DEPARTMENT OF TRANSPORTATION

Assessment of Bridge Decks with Glass Fiber-Reinforced Polymer (GFRP) Reinforcement

Behrouz Shafei, Principal Investigator
Institute for Tranpsortation
Iowa State University

MARCH 2023

Research Report
Final Report 2023-13

To request this document in an alternative format, such as braille or large print, call 651-366-4718 or 1-800-657-3774 (Greater Minnesota) or email your request to ADArequest.dot@state.mn.us. Please request at least one week in advance.

Technical Report Documentation Page

1. Report No. MN 2023-13	2.	3. Recipients Accession No.	
4. Title and Subtitle Assessment of Bridge Decks with Glass Fiber-Reinforced Polymer (GFRP) Reinforcement		5. Report Date March 2023 6.	
7. Author(s) Behrouz Shafei, Brent Phares, Dikshant Saini, and Shadi Azad		8. Performing Organization Report No.	
9. Performing Organization Name and Address Institute for Transportation Iowa State University 2711 S. Loop Drive, Suite 4700 Ames, IA 50010		10. Project/Task/Work Unit No. 11. Contract (C) or Grant (G) No. (c) 1003320 wo (4)	
12. Sponsoring Organization Name and Address Minnesota Department of Transportation Office of Research & Innovation 395 John Ireland Boulevard, MS 330 St. Paul, Minnesota 55155-1899		13. Type of Report and Period Covered Final Report 14. Sponsoring Agency Code	
15. Supplementary Notes http://mdl.mndot.gov/			

16. Abstract (Limit: 250 words)

In 2018, the Minnesota Department of Transportation (MnDOT) constructed a pair of side-by-side bridges on TH 169 over Elm Creek, with glass fiber-reinforced polymer (GFRP) reinforcement used in one deck and conventional epoxy-coated steel reinforcement used in the other. To understand the behavior of GFRP reinforcement and compare the performance and durability of the GFRP- and steel-reinforced decks, the following efforts were undertaken: (1) collect structural behavior information and response characteristics of the two bridge decks under service loads; (2) examine the short- and long-term performance characteristics of the two bridge decks; and (3) assess the advantages of using non-conventional, corrosion-resistant deck reinforcement. From the outcome of this four-year monitoring program, both bridge decks behaved similar to each other and as expected. The GFRP-reinforced deck showed no unusual behavior or sign of deterioration compared to the steel-reinforced deck. Although similar patterns of surface and full-depth cracks were observed in both decks, the structural integrity of both bridges was found to be consistent with design specifications. The short- and long-term comparison of the decks indicated that the use of GFRP bars can be a promising alternative in bridge deck reinforcement.

17. Document Analysis/Descriptors Bridge decks, Glass fiber reinforced plastics, Reinforcement (Engineering), Performance		18. Availability Statement No restrictions. Document available from: National Technical Information Services, Alexandria, Virginia 22312	
19. Security Class (this report) Unclassified	20. Security Class (this page) Unclassified	21. No. of Pages 102	22. Price

ASSESSMENT OF BRIDGE DECKS WITH GLASS FIBER-REINFORCED POLYMER (GFRP) REINFORCEMENT

FINAL REPORT

Prepared by:

Behrouz Shafei, Ph.D., P.E.
Associate Professor
Institute for Transportation, Iowa State University

Brent Phares, Ph.D., P.E.
Research Associate Professor
Institute for Transportation, Iowa State University

Dikshant Saini, Ph.D.
Postdoctoral Research Associate
Institute for Transportation, Iowa State University

Shadi Azad
Graduate Research Assistant
Institute for Transportation, Iowa State University

MARCH 2023

Published by:

Minnesota Department of Transportation
Office of Research & Innovation
395 John Ireland Boulevard, MS 330
St. Paul, Minnesota 55155-1899

ACKNOWLEDGMENTS

We would like to gratefully acknowledge the Minnesota Department of Transportation (MnDOT) for sponsoring this research project.

The research team would also like to thank the Technical Advisory Panel (TAP) members, including Paul Kettleson, Joseph Black, Paul Rowekamp, Paul Stenberg, Katherine Lodin, and Lucas Brockman, for their time, guidance, and feedback. In addition, the authors would like to acknowledge the administrative coordination made by David Glyer throughout the course of this research project. The authors wish to thank Doug Wood and Owen Steffens for their assistance with the field investigations performed by Iowa State University. Special thanks is also given to the MnDOT field engineers and traffic control crew for helping the research team access the two bridges investigated in this research project.

TABLE OF CONTENTS

LIST OF FIGURES

LIST OF TABLES

EXECUTIVE SUMMARY

In 2018, the Minnesota Department of Transportation (MnDOT) constructed two side-by-side bridges on TH 169 over Elm Creek, with the northbound bridge deck reinforced with conventional steel bars and the southbound slab reinforced with glass fiber-reinforced polymer (GFRP) bars. The goal of the research project described in this report was to evaluate the fundamental structural behavior of the GFRP-reinforced bridge deck compared to that of the steel-reinforced bridge deck. To achieve this goal, comprehensive field testing was carried out to investigate the performance of the two bridges, and laboratory testing was conducted on the GFRP rebars used in the southbound bridge deck.

Prior to placing the concrete in the bridge decks under consideration, vibrating wire (VW) gauges were installed to measure the strain values inside the decks. To best measure performance, gauge locations were selected to capture the extreme response, characterize the general response, and determine the relevant response measures (e.g., live load girder distribution factors [GDFs]). The temperature at each strain gauge was also captured from the thermistors built into the VW gauges. The VW gauges were connected to a data-acquisition system placed under the bridge deck. The data from the gauges were recorded continuously over a period of three years using the data-acquisition system.

In addition to these long-term performance monitoring efforts, three live load field tests were performed on each of the bridges. The first test was conducted prior to opening the bridges to regular traffic. The second and third load tests were conducted in June 2021 and August 2022, respectively. Strains recorded during the live load testing were analyzed to evaluate deck behavior. The primary focus of the live load tests was to understand the manner in which the decks participate globally along with the girders to transfer vehicle loads longitudinally to the abutments.

The research project also included a condition assessment of the bridge decks at regular intervals throughout the duration of the project. The condition assessment included documentation of the deck surface and any full-depth cracks on top of and underneath the bridge decks, including the types and locations of the cracks and other relevant information.

The research project also evaluated the mechanical properties of the GFRP rebar used in the southbound bridge deck. For that purpose, the researchers conducted a set of laboratory tests on the GFRP rebar used by the contractor. The specimens were loaded in tension until failure, while force, displacement, and strain were measured during loading. The comparisons between the short- and long-term performance of the bridge decks reinforced with steel and GFRP rebar revealed no significant difference over the years, indicating that GFRP bars could be used as a promising alternative in bridge deck reinforcement.

A detailed life-cycle cost analysis (LCCA) of the two bridges was also conducted to evaluate the potential of GFRP reinforcement as a viable economic option. The LCCA showed that using GFRP rebars as an alternative to steel reinforcement in bridge decks decreased the expected life-cycle cost, especially for extended service durations.

CHAPTER 1: INTRODUCTION

1.1 PROJECT BACKGROUND

In 2018, the Minnesota Department of Transportation (MnDOT) constructed a pair of side-by-side bridges on Trunk Highway (TH) 169 over Elm Creek, one with glass fiber-reinforced polymer (GFRP) deck reinforcement (bridge 27W37) and the other with conventional epoxy-coated steel reinforcement (bridge 27W36). Because these two bridges would be exposed to the same environmental conditions, experience very similar traffic, and be constructed within the same timeframe, a unique opportunity existed to identify and evaluate differences in performance between them.

The main goals of the research project described in this report were as follows:

- Collect the structural behavior information and response characteristics of the two bridge decks under service loads
- Examine the short- and long-term performance characteristics of the two bridge decks
- Assess the impact of using non-conventional, corrosion-resistant deck reinforcement on life-cycle cost

Although there is wide use of GFRP reinforcement in bridge decks in some parts of Canada, there have been few GFRP-reinforced bridge decks built in the United States. The Canadian decks were primarily designed using the empirical design method in the Canadian Highway Bridge Design Code (CSA S6). This method differs from the design guidelines produced by the American Association of State Highway Transportation Officials (AASHTO) and the American Concrete Institute (ACI).

To maximize the knowledge and experience gained through the use of nonmetallic reinforcement in one of the bridge decks and to understand how the performance and durability of GFRP-reinforced bridge decks compares with the performance and durability of conventional bridge decks reinforced with epoxy-coated steel rebar, a systematic effort is planned for this project. The outcome is expected to directly contribute to the development of guidance and details for constructing corrosion-resistant bridges with service lives beyond 100 years.

1.2 RESEARCH ACTIVITIES

The following activities were undertaken for this research project.

1.2.1 Activity 1 – Bridge Instrumentation during Construction

Considering the importance of the long-term monitoring of the concrete and the GFRP rebar embedded in the concrete, it was critical to install strain gauges and thermocouples during the construction of the bridge decks. Upon receiving the bridge drawings, the research team first determined the best distribution of embedded sensors to maximize the efficiency of data-collection efforts. During construction, both bridges were instrumented with a set of 16 vibrating wire (VW) strain gauges to continuously measure the strains and temperatures within the concrete deck. VW strain gauges have

been proven to deliver a higher accuracy for long-term monitoring while providing a longer service life than other types of sensors. Each VW strain gauge was also equipped with a thermistor that measures the temperature at the location of the gauge.

1.2.2 Activity 2 – Long-Term Monitoring

The instrumentation installed in each of the bridge decks during construction was connected to a long-term data-acquisition system. To eliminate the extra cost and potential issues associated with data communication, the data gathered through the instrumentation were stored locally and downloaded during inspection visits scheduled every six months.

1.2.3 Activity 3 – Live Load Field Testing

Live load field tests were performed on each of the bridges three times throughout the duration of the project. The initial live load test was conducted immediately after bridge construction. The second and third live load tests were performed in 2021 and 2022, respectively. For live load field testing, a standard dump truck provided by MnDOT was used. During live load field testing, a variety of transducers such as BDI Intelliducer gauges and deflectometers were installed on the bridges' superstructures. These gauges were placed on both the bridge deck and girders. Subsequently, a loaded truck of known weight and dimensions was driven across the bridges, with the resulting response data collected. The data from the three tests were compared to identify any changes in the behavior of bridge decks.

1.2.4 Activity 4 – Bridge Deck Inspection

Regular visits to the bridge site were made every six months throughout the entire duration of the project to inspect the condition state of the bridge decks and to retrieve the recorded long-term monitoring data for off-site processing. One of the main objectives of the inspection efforts was to document the number of cracks and measure crack spacing, crack penetration depth, and crack width.

1.2.5 Activity 5 – Laboratory Tests on GFRP Rebar

To better understand the mechanical properties and strength of the GFRP rebar used in the bridge deck evaluated in this study, the research team conducted a limited set of laboratory material characterization tests. MnDOT provided approximately 60 ft of GFRP rebar for this testing. The tensile strength properties obtained for the GFRP rebar were found to be consistent with the values identified in the literature.

CHAPTER 2: LITERATURE REVIEW

Steel-reinforced concrete (SRC) bridge decks have become standard for bridges. Although SRC decks have several advantages, the steel rebar in concrete is susceptible to corrosion during the service life of a bridge. This phenomenon becomes more prominent in colder regions where deicing salts are used. The corrosion of steel is mainly responsible for the degradation of bridge decks. Therefore, it is not surprising that existing bridge decks often need major repair or complete replacement after 50 to 60 years. This research project focused on the use of corrosion resistant GFRP rebar. The research team completed the following comprehensive literature review on the use of GFRP rebar for the reinforcement of bridge decks and on how bridge deck performance research is conducted against current bridge design specifications and standards.

2.1 STUDIES ON BRIDGE DECKS REINFORCED WITH FRP

Among the past studies, Kumar and GangaRao (1998) made the first effort to evaluate the fatigue response of concrete bridge decks reinforced with GFRP rebar. The primary aim was to evaluate the stiffness degradation of the bridge decks. From the experimental results, the deck degradation rate with GFRP bars was found comparable to that with a steel-reinforced bridge deck. The outcome of the experimental tests revealed that GFRP is a favorable material and that the deck with GFRP rebar behaves similar to the one reinforced with steel rebar. Because of the promising results obtained from a number of similar studies (e.g., Benmokrane et al. 2006, Deitz 1998, Eitel 2005, El-Ragaby et al. 2005, El-Ragaby et al. 2007, El-Salakawy et al. 2005), fiber-reinforced polymer (FRP) rebar has become an increasingly attractive alternative to steel for reinforcing concrete bridge decks.

Focusing on the use of GFRP rebar, a number of studies have been performed in the last three decades. Harik et al. (1999) investigated deck specimens cast from a GFRP rebar reinforced concrete (RC) slab and GFRP panel with an externally bonded tubular section (transverse to traffic directions). From the three-point bending tests of different lengths and depths, the deck specimens were found to satisfy the deflection and strength criteria of the Ohio Department of Transportation (ODOT) with a factor of safety of at least 3. The deck specimens were found to fail in combined bending and shear and debonding of GFRP tubular sections from the concrete.

In another study, Hassan et al. (2000) investigated the behavior of a highway bridge slab reinforced with FRP rebar. Two full-scale models were tested, one specimen reinforced with carbon FRP (CFRP), and the second slab with hybrid glass FRP and steel reinforcement. From the detailed finite element study, the ultimate load capacity of the continuous full-scale deck slabs were found more than seven times the service load specified by AASHTO specifications (1996). The researchers proposed using a reinforcement ratio of 0.3% CFRP per ft^2 (fiber volume ratio 60% or more) as bottom and top reinforcement in each direction to satisfy the serviceability and ultimate capacity requirement for the span-to-depth ratio; and, for GFRP-reinforced decks, 1.2% and 0.6% on top and bottom, respectively, in the transverse direction. In the longitudinal direction, it should be 0.6% each on top and bottom.

Deitz et al. (2000) reported experimental results of 12 full-scale RC deck panels. Three different reinforcing schemes were adopted: RC deck with top and bottom epoxy-coated steel (ECS) rebar, RC deck with top and bottom GFRP rebar, and RC deck with a top mat of GFRP rebar and a bottom mat of ECS rebar (referred to by the researchers as hybrid). It was found that the performance criteria (ultimate load, load vs. displacement, moment vs. curvature, and type of failure) were governed by the tensile reinforcement type. Prior to cracking, the load-deformation curves were the same for all 12 specimens. After cracking, the deck panels with GFRP reinforcement exhibited low stiffness and larger crack widths as compared to RC decks with steel reinforcement. The researchers also noted that all of the GFRP specimens failed in combined flexure and shear mode. From the experimental results, the researchers also found that the GFRP-reinforced deck did not satisfy the AASHTO requirements for maximum crack width criteria. The displacement for the GFRP- and hybrid-reinforced decks were significantly larger than that for the ECS-reinforced deck.

In a separate effort, Hall and Ghali (2000) investigated the long-term performance of GFRP-reinforced concrete beams. The objective was to identify whether the long-term deflection method for steel beams can be applied to GFRP beams. From the experimental results, the deflections of GFRP beams were found to be 1.7 times that of the steel-reinforced beams due to creep and shrinkage effects. El-Salakawy and Benmokrane (2004) tested 10 full-scale concrete slabs to study the performance of FRP bars against that of steel bars. Out of 10 specimens, five were reinforced with GFRP bars, three with CFRP bars, and two with steel bars. From the test results and observations, the number of cracks, crack spacing, crack penetration depth, and crack width of the GFRP slabs were similar to that of the steel-reinforced slabs. The GFRP slabs failed in the shear tests, whereas the steel-reinforced slabs failed by yielding of the steel.

In another study, El-Salakawy et al. (2005) carried out field investigations on the first bridge deck slab reinforced with GFRP bars. The bridge deck was instrumented at critical locations for strain and temperature gradient measurement. In this bridge, one span was reinforced with galvanized steel rebar and the other with GFRP bars. The maximum strain in the GFRP slab was 30 μstrain during the test (0.2% of the ultimate strain). The deflection of the bridge deck and slab never exceeded the Canadian Standard Association (CSA S6 2000) allowable limits. Focusing on the stiffness of GFRP-reinforced decks, Holden et al. (2014) investigated two precast deck panels constructed with GFRP bars and six girders of a single-span bridge. The researchers found the deck deflections and stresses were within the limits of the AASHTO specifications. From their parametric study, the researchers found that the deck depth could be reduced with the use of GFRP rebar.

In addition to the use of GFRP in the form of rebar, several studies have been conducted on composite bridge decks utilizing GFRP mechanical properties. Yost and Schmeckpeper (2001) studied the flexural performance of bridge deck panels reinforced with two-dimensional (2D) FRP grids. Two different FRP grids were investigated, one reinforced with a hybrid of glass and carbon fibers and a second reinforced with carbon fibers only. The researchers identified several problems with the use of these FRP grids as structural reinforcement for concrete bridge decks. Most importantly, the modulus of elasticity of the FRP grids was considerably lower than that of steel. As a result, larger deflections and greater crack widths were observed as compared with steel-reinforced concrete members of equal strength.

To study the fatigue performance of FRP bridge decks under extreme temperature loadings, Kwon et al. (2003) carried out a fatigue test of four composite bridge decks. The deck specimens were tested for one million wheel load cycles at low temperatures, followed by one million wheel load cycles at high temperatures. The bridge deck was subjected to a total of 10 million wheel load cycles. FRP bridge decks exhibited satisfactory performance under extreme temperature conditions. However, the stiffness of FRP bridge decks was found to be substantially affected by the extreme temperature conditions.

Kitane et al. (2004) investigated the performance of a hybrid deck system. The system was composed of a layer of concrete on the compression side of the all-GFRP deck section. The primary aim was to reduce the initial cost and increase the stiffness of the all-GFRP deck. The model was found to meet the stiffness requirement with significant reserve strength. And the stiffness degradation from the fatigue test results was also found to be insignificant. A new hybrid system was proposed by Cheng (2005) in which a hybrid polypropylene (PP) fiber-mixed concrete and thin continuous FRP mesh and laminated plates were used. Static and fatigue tests were carried out to determine the feasibility of this system in the construction of slab-on-girder type bridges. Test results showed satisfactory performance of the all-concrete slabs (slab-plate interface, component and system-level flexure, and shear and fatigue response tests).

Alagusundaramoorthy et al. (2006) studied the force deformation characteristics of FRP composite bridge deck panels. The test results of the panels were compared with those for RC deck panels and also with the performance criteria as per ODOT. The factors of safety against failure of bridge deck panels varied from 3 to 8 and satisfied the performance criteria. Cheng (2011) studied the fatigue performance of a steel-free concrete bridge deck reinforced with a CFRP stay-in-place form under repeated traffic loads. This paper presented a fatigue analysis tool specifically developed for this study and found that flexural stiffness deteriorated gradually with the number of cycles, but no failure in the FRP or concrete during the 2 million cycles. The deflection damage was found to decrease as the amount of CFRP reinforcement and concrete strength increase.

The Bridge Engineering Center (BEC) at Iowa State University has been active in this area of research and conducted numerous evaluations of FRP for use in bridges. Examples of the BEC's related research include the following: use of post-tensioned CFRP rods for bridge strengthening, use of CFRP plates for bridge strengthening, use of GFRP bars in a precast/prestressed concrete girder bridge deck, use of GFRP for the fabrication of a temporary bypass bridge, and use of GFRP fabric for emergency repair of damaged precast/prestressed concrete girders.

2.2 BRIDGE DECK PERFORMANCE STUDIES

From the existing literature, it can be concluded that resistance to corrosion and a high strength-to-weight ratio make GFRP rebar suitable for use as bridge deck reinforcement, especially where harsh environmental conditions exist (Cheng and Karbhari 2006, Hall and Ghali 2000, Trejo et al. 2005). However, GFRP is still a relatively new material for bridge deck reinforcement, leaving a range of questions about its long-term strength and durability.

Although accelerated tests have been performed on GFRP rebar (e.g., Park et al. 2014), attempting to rapidly replicate the degradation, which typically takes years to develop with accelerated tests, cannot guarantee reliable long-term results. With the limited number of field investigations on GFRP-reinforced bridge decks in service (e.g., El-Salakawy et al. 2005), actual data still needs to be collected to understand the bridge behavior over time and verify the sufficiency of design guidelines provided by ACI 440.1 (2015) and AASHTO (2017).

Bridge deck performance can be evaluated by conducting live load tests and through long-term monitoring. Live load tests are performed on the bridge deck to evaluate the response of the bridge deck to vehicle loads. These tests can reveal important information on the behavior and integrity of the bridge deck. In long-term monitoring, the primary objective is to determine the effect of temperature changes on the bridge deck. For this purpose, strain gauges embedded in the concrete deck are utilized. In the past, live load tests were performed on conventional girder bridge decks, focusing on the girder system to investigate the load distribution among the locations of the girders. For that purpose, girder distribution factors (GDFs) were calculated to evaluate bridge deck performance (Nassif et al. 2003, Tabsh and Tabatabai 2001, Yang and Myers 2003).

Stallings and Porter (2002) performed live load testing on the Uphapee Creek Bridge in Alabama. The strain response of the bridge deck was the researchers' specific focus. The bridge deck was constructed with high-performance concrete (HPC). Live load distribution factors, deflections, strains, and stresses from the live load tests were compared with design equations in AASHTO LRFD (1998) and AASHTO Standard Specifications (1996). The predictions from both AASHTO specifications were found to be conservative as compared to values obtained from field tests. Live load tests were performed on the South Platte River Bridge near Commerce City, Colorado, as reported by Cao (1996). The measured strain data from live load tests were utilized to evaluate the bending moments incurred in the bridge deck. From the data analysis, it was found that negative moments in the bridge deck are reduced by differential girder deflections.

In a separate effort, Semendary et al. (2017) evaluated the live load moment distribution factors for an adjacent precast/prestressed concrete box beam bridge with a new reinforced/grouted ultra-high performance concrete (UHPC) shear key connection configuration. The bridge was tested using two load trucks with weights of 56.1 kips (249.5 kN) and 53.4 kips (237.5 kN). On comparing GDFs to those from AASHTO load and resistance factor design (LRFD) equations, the GDFs from the field tests were underestimated by 4.3% for the exterior beams and 12.7% conservative for the interior beams. More recently, Torres et al. (2019) evaluated the live load distribution factors of a deteriorated double-T bridge in Coalville, Utah. Displacements, rotations, and strains were measured to quantify the load carrying behavior of the bridge. A loaded truck with a gross weight of 61.6 kips (274 kN) was utilized. Based on validated finite element (FE) models, a parametric study was performed to compare GDFs from AASHTO LRFD with the GDFs from the FE simulation results.

During their service lives, concrete bridges are subjected to environmental stresses such as temperature, humidity, and moisture. Among them, the temperature effects can significantly affect the performance of concrete bridges. The thermal or temperature effects can be viewed as two

superimposed effects. The first effect is due to the uniform change in temperature that happens over the entire superstructure. This effect causes free elongation for an unrestrained structure. When the structure is restrained, it will be subjected to uniform internal stresses. The second thermal effect is due to temperature gradients when the bridge superstructure is heated differentially. The temperature gradient causes flexural strains in the superstructure. The current AASHTO LRFD Bridge Design Specifications (2017) provide guidelines based on recommendations of National Cooperative Highway Research Program (NCHRP) Report 276 (Imbsen et al. 1995) for the design of bridge components against thermal loads.

In a comprehensive study, Cuelho et al. (2006) investigated the performance of three bridge decks by performing live load tests and long-term monitoring on the decks. VW gauges were used to monitor the long-term performance of the bridge decks. In addition, the performance of the bridge decks was investigated by conducting visual distress surveys and corrosion tests. From the strain data, the researchers found that long-term shrinkage strain in the decks ranged from 300 to 350 μstrain. The strain variation with respect to temperature was found comparable to strain calculated from the coefficients of thermal expansion of the deck concrete. More recently, Pantelides et al. (2012) investigated the long-term performance of precast concrete panels for bridge decks. The panels were instrumented with strain gauges, displacement sensors, and accelerometers. VW strain gauges were used in the longitudinal and transverse directions. The results showed no cracking and negligible deflections. Also, the vehicle-crossing tests indicated that the AASHTO LRFD guidelines apply to the load distribution factors of the interior beams.

The long-term monitoring findings of two hybrid single span bridges were reported by Ahmed et al. (2014). The bridge decks contained GFRP reinforcement in the top and steel rebar in the bottom. The cracks due to live load bending moment were studied using fiber optic gauges, showing no particular difference between the hybrid decks and steel or FRP-reinforced slabs. The MnDOT constructed its first GFRP-reinforced bridge deck on MN 42 over Dry Creek just north of Elgin, Minnesota. To maximize the knowledge and experience gained in constructing this bridge deck, a research project was completed by Shafei et al. (2019), investigating the performance of this bridge deck system. The main focus of the referenced project was on cracking, deck stiffness, load distribution factors, and GFRP rebar strains. The results suggested that GFRP rebar can be a viable option for replacing steel rebar in bridge decks.

CHAPTER 3: LONG-TERM MONITORING

3.1 INTRODUCTION

The structural performance of the two bridges under consideration was investigated using an array of embedded strain gauges and thermocouples installed during the construction of the bridges in the summer and fall of 2018. From a long-term performance perspective, GFRP does not oxidize/rust, thus resulting in less deterioration on the deck compared to its steel counterpart. This functionally extends the service life of the deck and lowers the life-cycle cost for the bridge. It should be noted that, despite the wealth of data collected from the two bridges during their first four years of service (as reported in this chapter), a four-year duration is essentially a snapshot when compared to 75+ years of service anticipated for these bridges. Hence, additional monitoring is recommended after 10, 25, and 35 years to obtain holistic insights, as the decks continue to degrade and live their lives.

3.2 SENSOR LAYOUTS

A total of 16 VW strain gauges were installed on each of the bridge decks during the construction phase. Figures 3.1 and 3.2 show the locations of the VW strain gauges embedded inside the two bridge decks during construction.

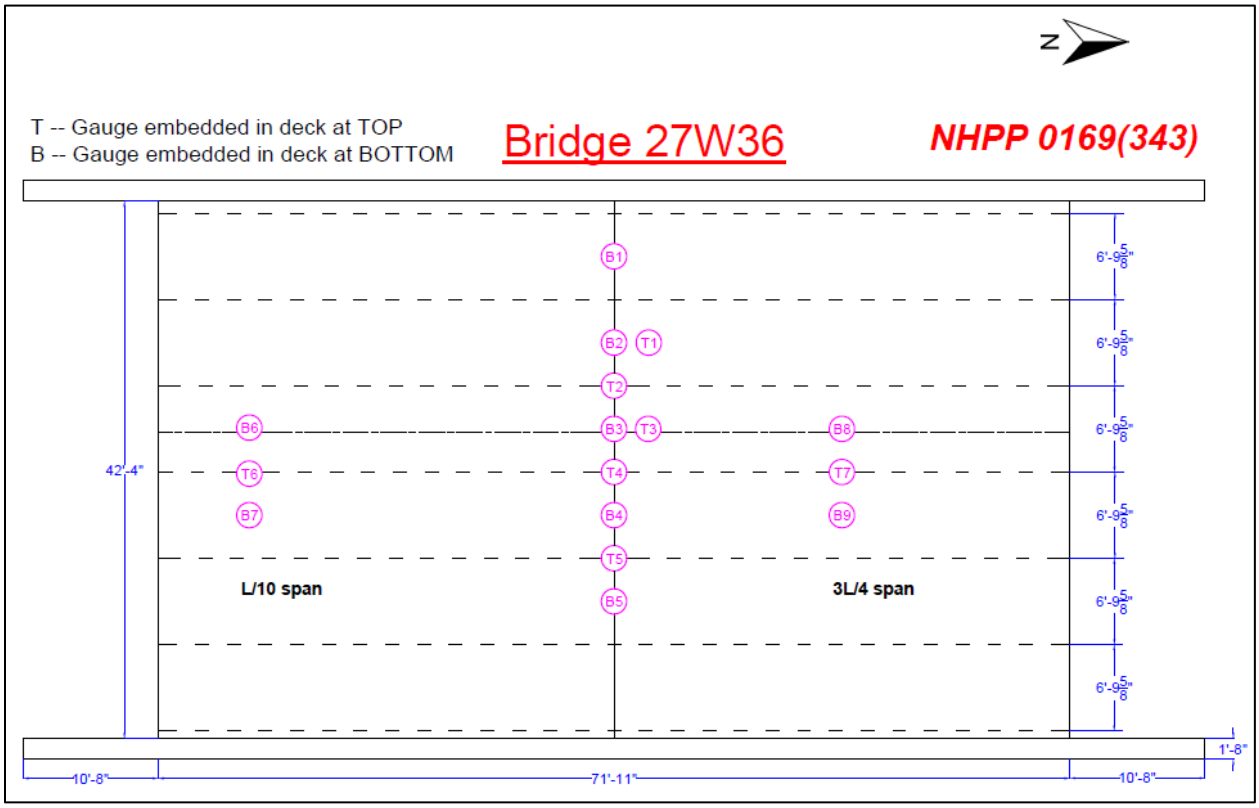

Figure 3.1. Instrumentation layout for long-term monitoring in steel-reinforced bridge deck (27W36)

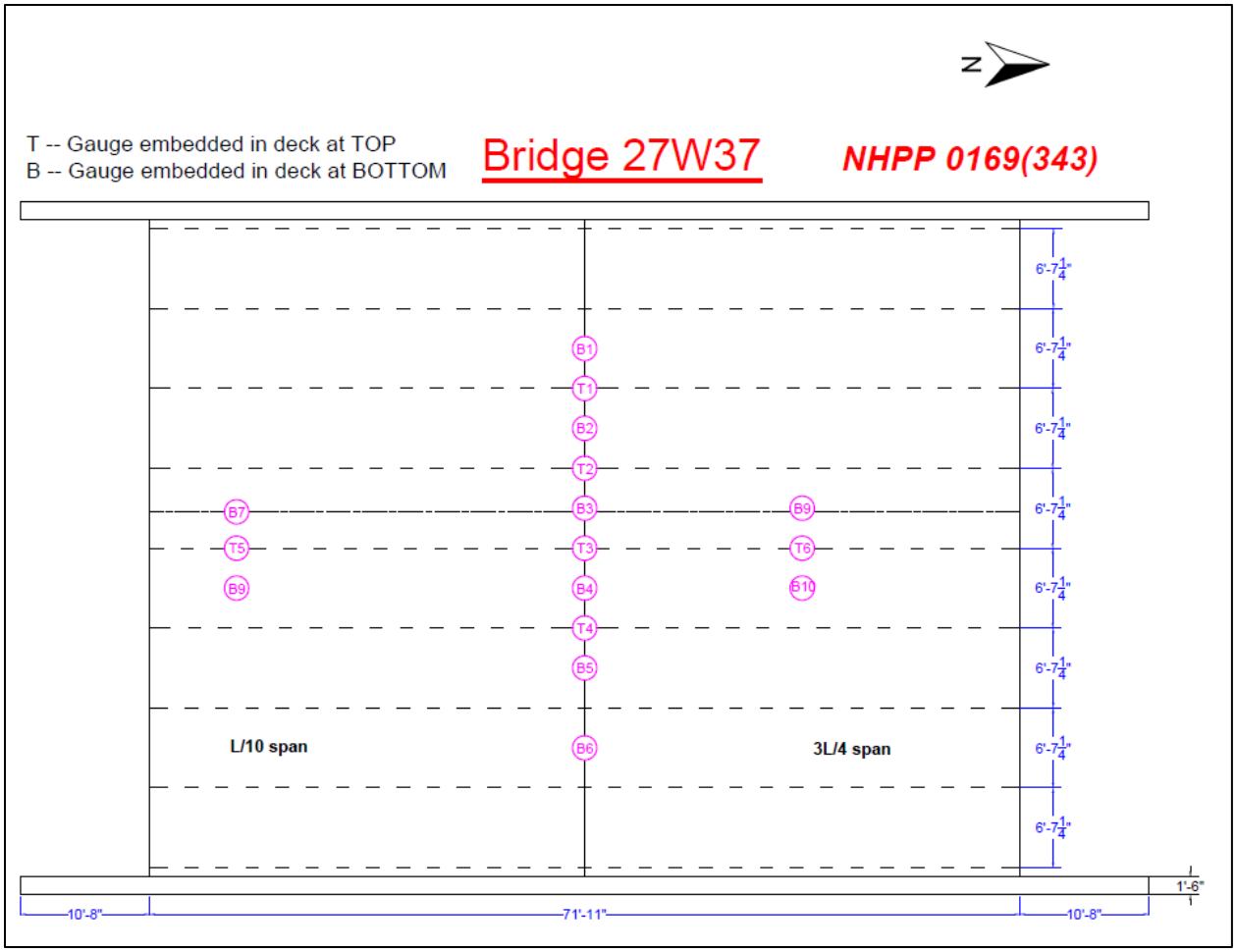

Figure 3.2. Instrumentation layout for long-term monitoring in GFRP-reinforced bridge deck (27W37)

The VW strain gauges were placed at L/10, L/2, and 3L/4 of the bridge deck, where L represents the total length of the bridge span.

Since the bridge deck is expected to behave as a one-way slab, the strain in the transverse direction, i.e., perpendicular to the traffic flow, is critical to record. Therefore, the VW strain gauges were placed along the transverse direction. From structural analysis, the tension occurs on the top of the bridge deck at the girders and on the bottom of the bridge deck midway between the girders. Noting the most damage-prone locations, the sensor layout was decided. The sensors on the top and bottom of the girders were designated as T and B, respectively.

While installing the sensors on site, the locations of the sensors slightly varied due to practical constraints because of the lack of space between rebar components or the unavailability of rebar at the location. Therefore, the actual locations of the rebar and the installed gauges were recorded for future analysis.

Once the deck was cast, the VW gauges were connected to the data-acquisition system.

3.3 VIBRATING WIRE STRAIN GAUGES

The GEOKON 4200 VW strain gauges used for this project have been primarily designed for long-term strain measurements in various structural components, such as decks, foundations, and piles. These strain gauges are equipped with a thermistor for reading temperature. The thermistor gives varying resistance as the temperature changes. Figures 3.3 and 3.4 show the GEOKON 4200 VW strain gauges, which were installed on the rebar using 1 in. × 0.5 in. × 0.5 in. blocks and tied using zip ties.

Figure 3.3. VW strain gauge

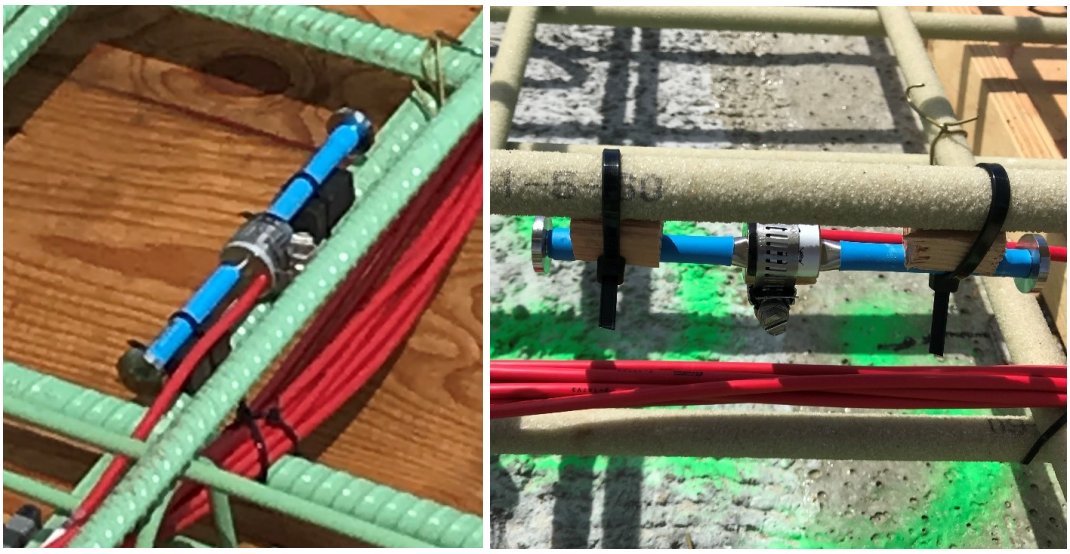

Steel-reinforced (27W36) *GFRP-reinforced (27W37)*

Figure 3.4. VW strain gauges installed inside the bridge decks

The parameters for the VW strain gauges are listed in Table 3.1.

Table 3.1. GEOKON 4200 strain gauge parameters

Parameter	Value
Gauge type	4200
Gauge factor	3.304
Start frequency	450 Hz
End frequency	1,200 Hz
Nominal batch factor	0.98

3.4 DATA-ACQUISITION SYSTEM

A CR1000 data logger was installed to continuously record the gauge data for this project (Figure 3.5).

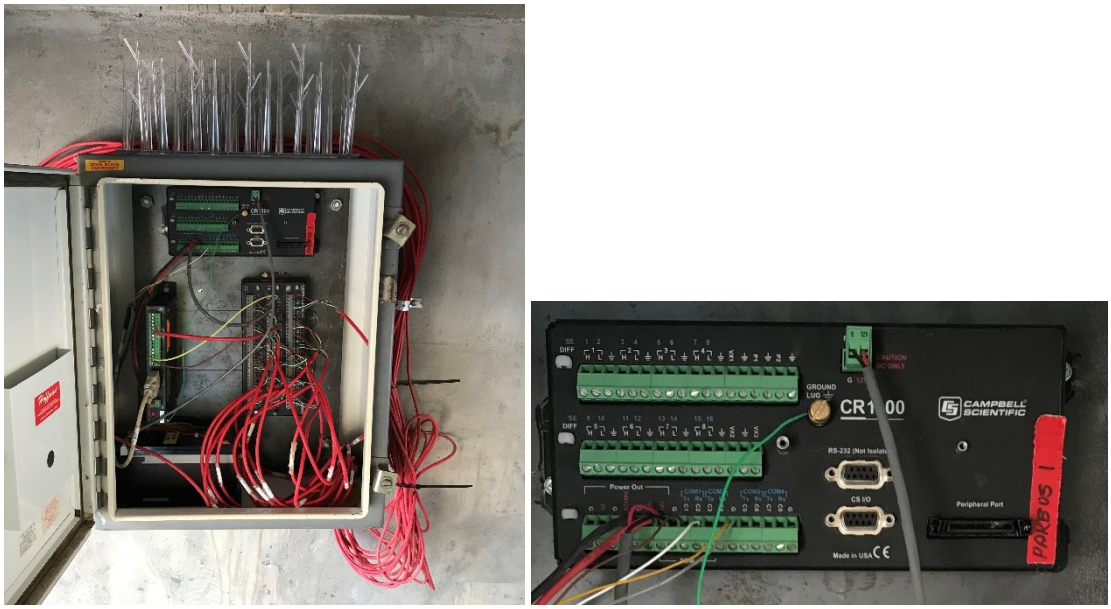

Figure 3.5. Data logger mounted in box

This system can be used for extreme temperature conditions and is reliable enough for remote environments. The data logger is powered with an uninterrupted power supply. To maintain the supply of power to the data-acquisition system, a solar panel was installed on site (Figure 3.6).

Figure 3.6. Solar panel installed at the bridge site

Each unit of the data-acquisition system can support up to 16 channels. The data logger and power supply were placed in a box. The data logger was located underneath each bridge deck, keeping it away from the proximity of pedestrians and traffic flow. The strain data from the bridge deck were recorded

every hour. With the current memory space, the data logger could store data for 10 months. For this project, the monitored data were collected every six months.

3.5 LONG-TERM MONITORING DATA

The strain data collected from the bridge site were studied from all sensor locations. In the early stage, the fluctuations in the recorded strains were mainly due to temperature and (initially) shrinkage effects. The strain data were thoroughly analyzed for anomalous behaviors, maximum compressive and tensile strains, and seasonal variations. An anomalous behavior in the strain data was defined as any unusual pattern that was deemed strikingly different from the trends and magnitudes obtained for the strain data over years. The maximum compressive and tensile strains in the concrete deck were used in identifying possible crack developments in the deck. The concrete normally cracks at a tensile strain of 100–120 μstrain.

Figure 3.7 shows the strain time histories of the three gauges at L/10 in the steel-reinforced bridge deck (27W36).

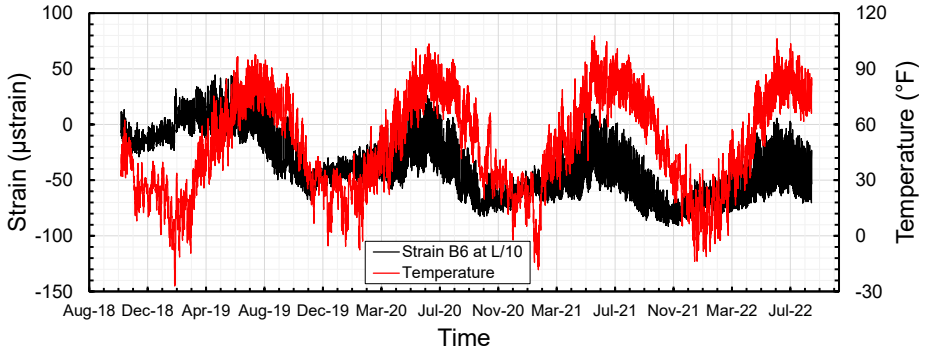

(a)

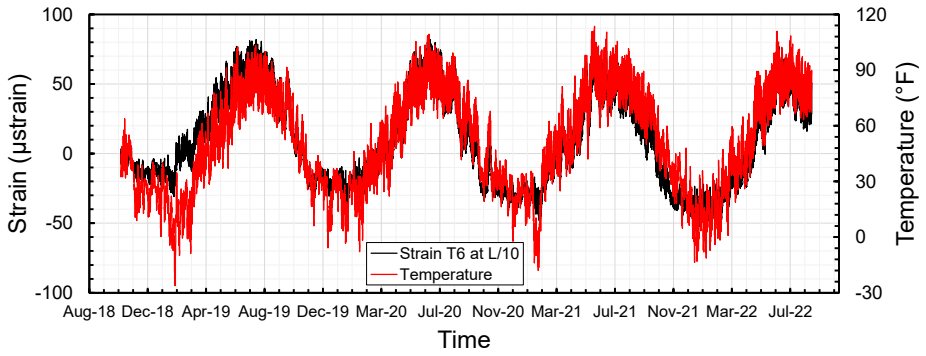

(b)

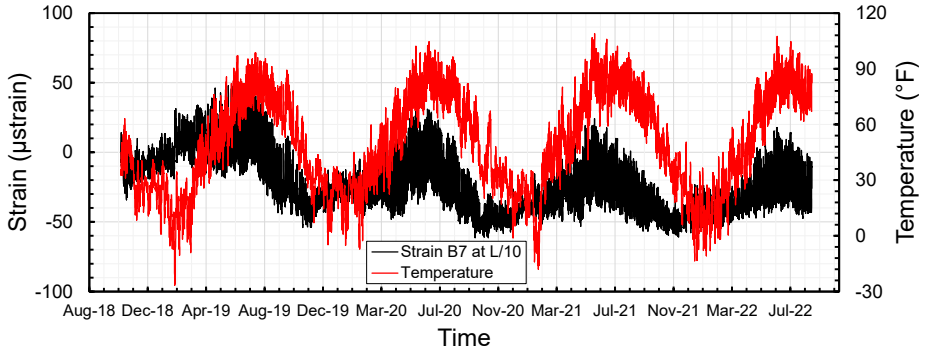

(c)

Figure 3.7. Strain time histories of gauges at L/10 length in steel reinforced bridge deck (27W36)

In the developed plots, negative and positive signs represent compression and tension, respectively. The temperature during the long-term monitoring period was found to range between -30°F and 120°F. The three strain gauges followed trends similar to the temperature, with high tensile and compressive strains occurring at the time of high and low temperatures, respectively. Considering that the bridge is not restrained along the transverse direction, expansion of the concrete due to high temperatures caused the tensile strain in the reinforcement, while low temperatures resulted in compression in the bars. The strain trends subsequently decreased over the years. The peak tensile strain was observed in June 2019 for gauges B6 and B7 and July 2020 for gauge T6. Although the tensile strain was well below the cracking strain of concrete, the photos taken during the last inspection showed transverse cracks at

L/10. Considering that the cracks might not intersect with the locations of the gauges, the incompatibility between the tensile strain and the cracks could be explained. As time passed, the deck was observed to be majorly in compression at gauges B6 and B7. Overall, the tensile strain values in the top gauge, T6, were higher than the strains measured in the bottom gauges, B6 and B7. At the same location, i.e., L/10, where L is the length of the bridge deck, higher tensile strains were recorded in the GFRP-reinforced bridge deck (27W37) bottom bars.

Figure 3.8 presents the strain at L/10 in the bridge deck reinforced with GFRP rebar.

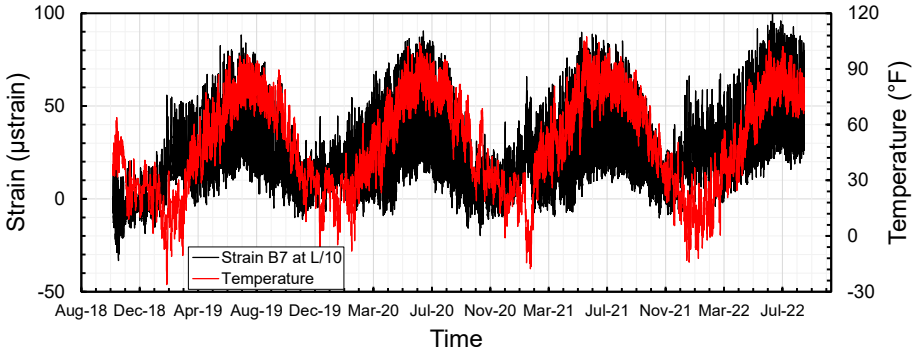

(a)

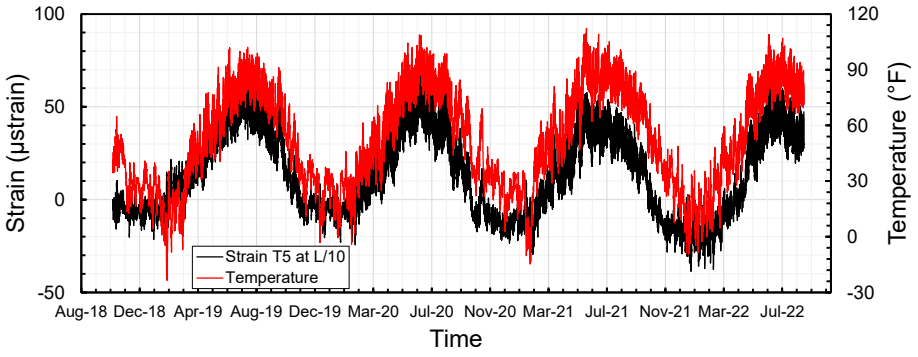

(b)

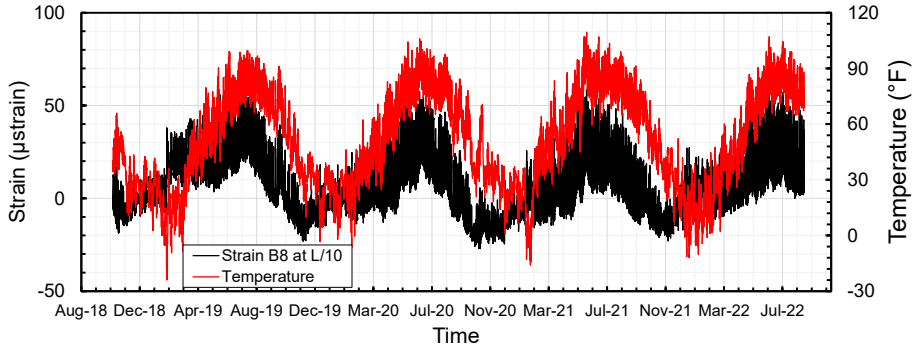

(c)

Figure 3.8. Strain time histories of gauges at L/10 length in GFRP-reinforced bridge deck (27W37)

The strain trends followed a pattern similar to the strains in the bridge with steel bars; however, the tensile strains increased over the years due to the slight increase in the peak temperatures. This trend was more significant at gauge B7, showing the peak tensile strain in June 2022. In addition, the overall tensile strains were much higher than the strains at the same location in the steel-reinforced bridge deck. The maximum tensile strain at gauge B7 was 101 μstrain, which reflects the possibility of hairline cracks at this location. Gauges B8 and T5 showed peaks with small changes over the years. Compared to the same locations in the steel-reinforced bridge deck (27W36), gauges B7 and T5 showed higher and lower tensile strains, respectively. The maximum tensile strains of gauges B8 and T5 did not exceed the concrete's cracking strain, while those recorded by gauge B7 are almost on the border between cracking and non-cracking. However, the inspections showed cracks at L/10, especially near the north abutment. It is important to note that the T5 gauge was implemented at L/10 from the south abutment, and the cracks of the south abutment were far from the location of the gauge.

Figure 3.9 presents the strain time histories of the gauges at the mid-span in the steel-reinforced bridge deck (27W36).

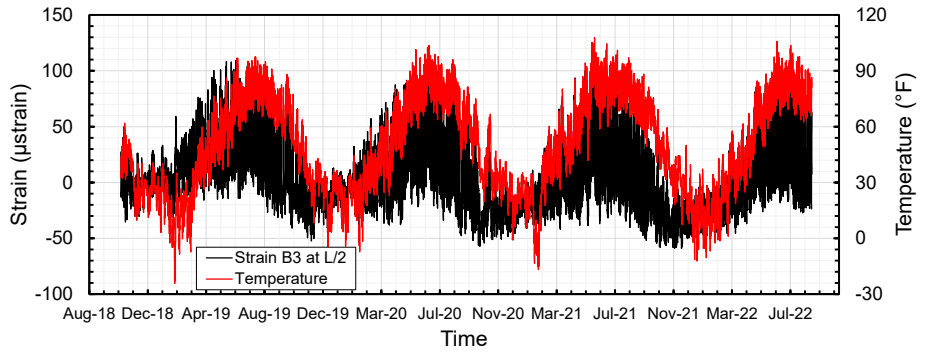

(a)

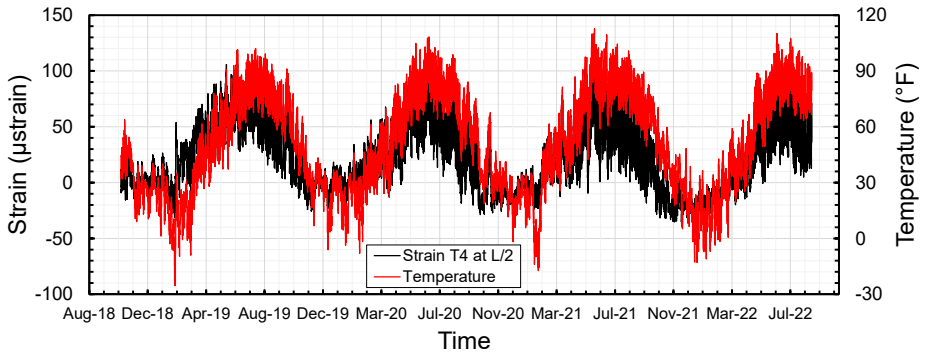

(b)

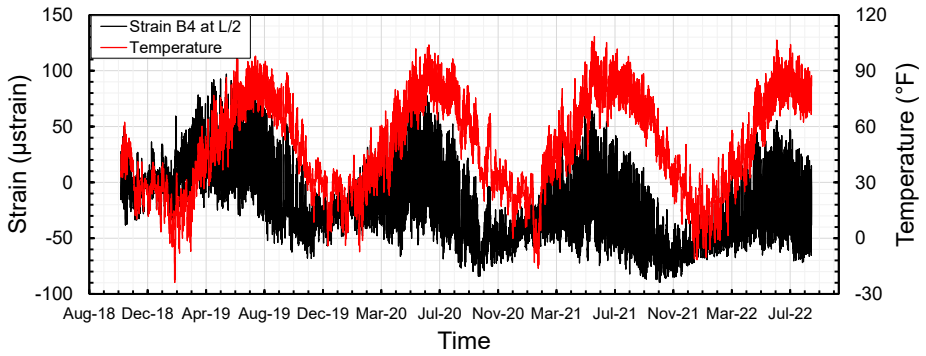

(c)

Figure 3.9. Strain time histories of gauges at the mid-span in steel-reinforced bridge deck (27W36)

At the mid-span, gauges B3, B4, and T4 showed maximum tensile strains of 114, 97, and 112 µstrain, respectively. This indicated the possible formation of cracks at the referenced locations. On comparing the strains from the top gauge, T4, with the bottom gauges, B3 and B4, the strains in the T4 gauge had less variation.

The strain time histories of the gauges at the mid-span in the GFRP-reinforced bridge deck (27W37) are shown in Figure 3.10.

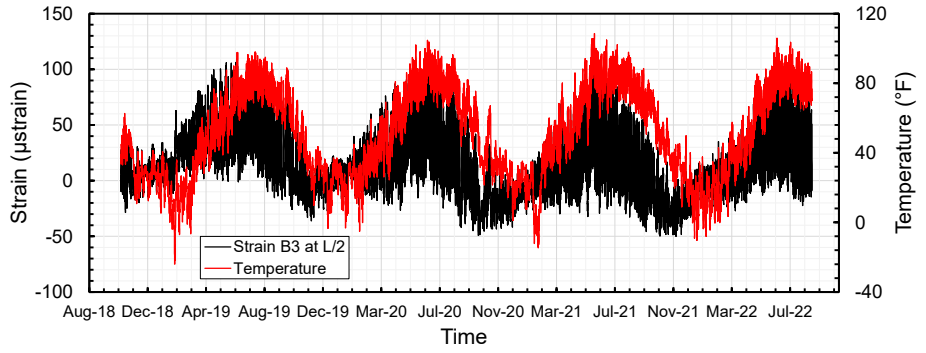

(a)

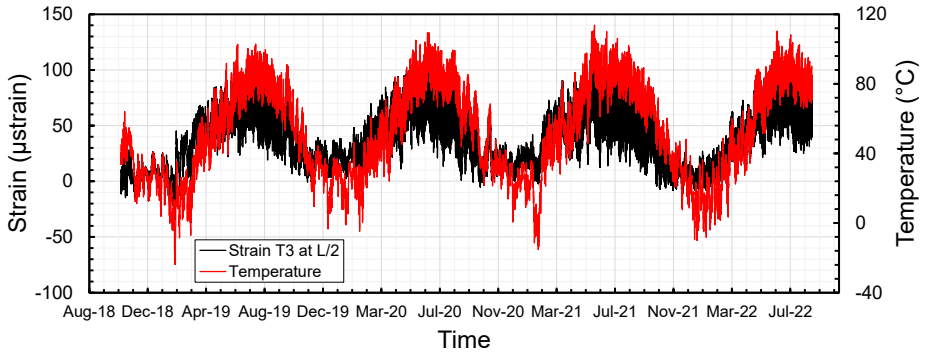

(b)

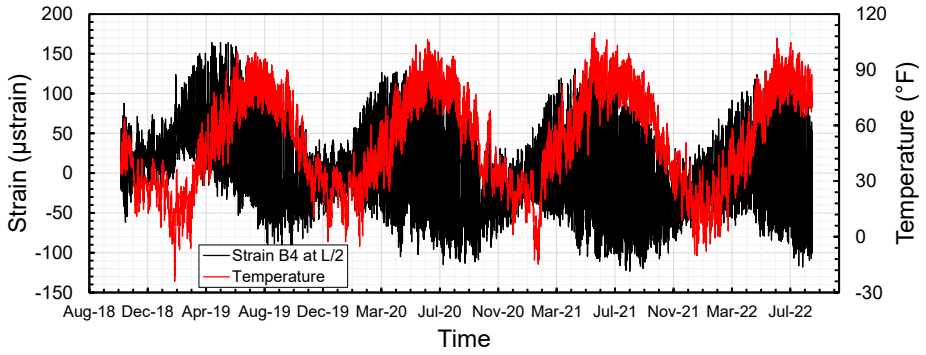

(c)

Figure 3.10. Strain time histories of gauges at the mid-span in GFRP-reinforced bridge deck (27W37)

The recordings from the B3, B4, and T4 gauges indicated the possibility of the formation of tensile cracks at the mid-span. A maximum tensile strain of 164 µstrain was obtained for the B4 gauge. The strains at the top and bottom of the deck showed an almost similar peak range in both bridge decks; however, the bars in the east side of the GFRP-reinforced bridge deck (27W37) demonstrated much higher tensile strains. This indicated the possible development of hairline cracks at the bottom and top of the deck in both bridges, while one side of the bridge with GFRP bars may face tensile cracks. This observation was well supported with photos taken during the inspections. As such, the GFRP bridge crack maps show the formation of cracks at L/2, and the inspections revealed cracks on the bottom surface of the slab in both bridges.

Figure 3.11 shows the strain time histories of the gauges at the quarter span of the steel-reinforced (27W36) and GFRP-reinforced (27W37) bridge deck.

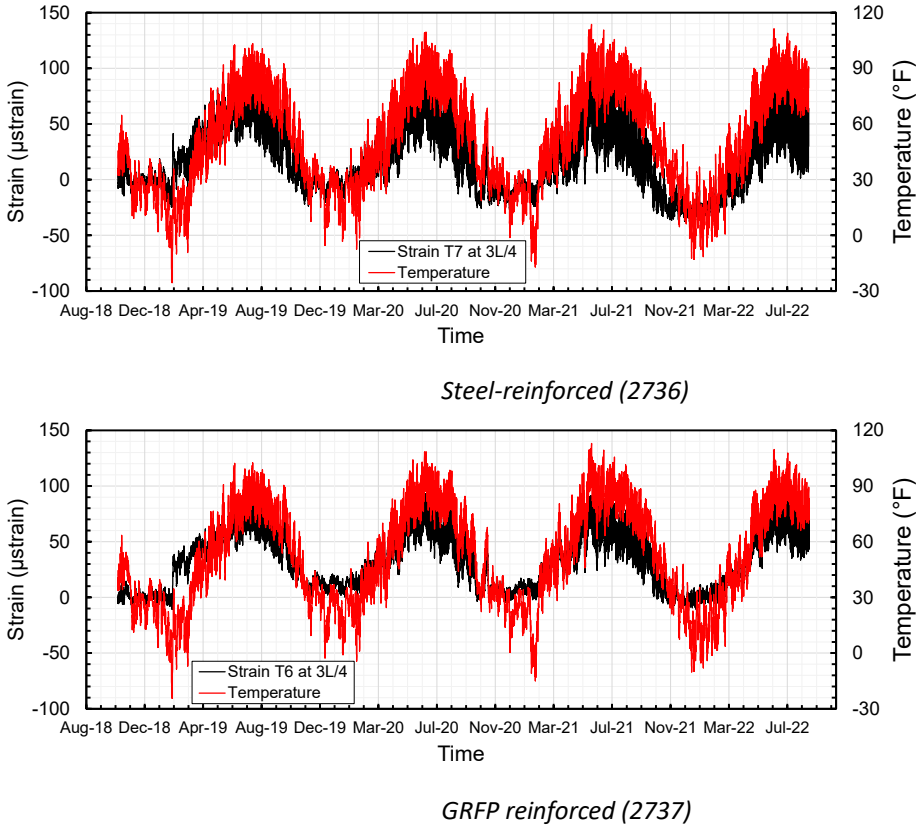

Figure 3.11. Strain time histories of gauges at the quarter span of both bridge decks

With further processing of the recorded strain data, Figure 3.12 shows the daily average strain time histories of the gauges placed over the middle axis of the steel-reinforced bridge deck (27W36) in the transverse direction.

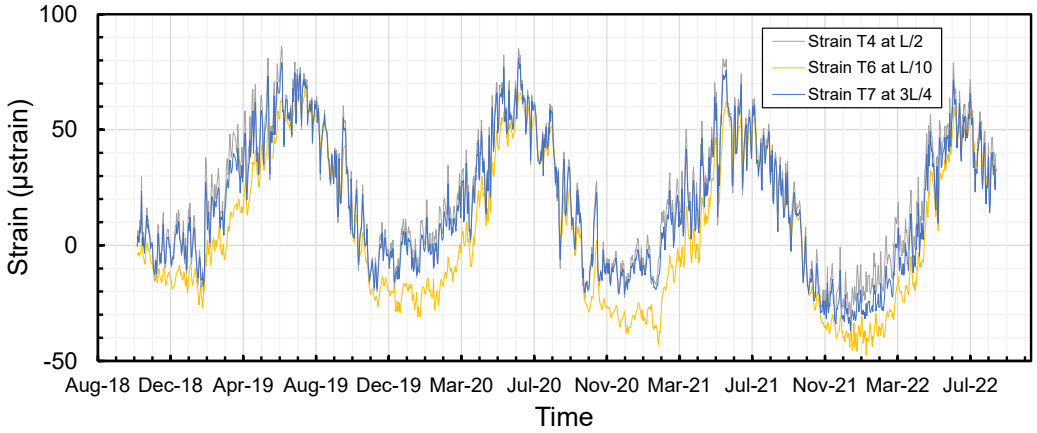

Figure 3.12. Daily average strain time histories of gauges at the middle axis/beamline in steel-reinforced bridge deck (27W36)

Gauges T4 (mid-span) and T7 (quarter-span) showed an almost similar trend over the years, indicating a daily average of 86 and 81 µstrain for maximum tensile strain and a daily average of -33 and -37 µstrain for maximum compressive strain, respectively. However, the tensile strain values recorded by gauge T6 at L/10 were usually lower than those at T4 and T7, especially over the colder months of a year. Gauge T6 also showed a maximum strain of 69 and a minimum strain of -48 µstrain.

Considering that the strain gauges placed over the middle beamline of the slab could not capture the cracks near them, the tensile strains seemed to change based on the temperature and time-dependent effects. As such, the contraction effect of the shrinkage over the years might have impeded the expansion effects of high temperatures and their subsequent temperature gradients.

Figure 3.13 shows the daily average of strains versus time between the beams of the steel-reinforced bridge deck (27W36) in the transverse direction.

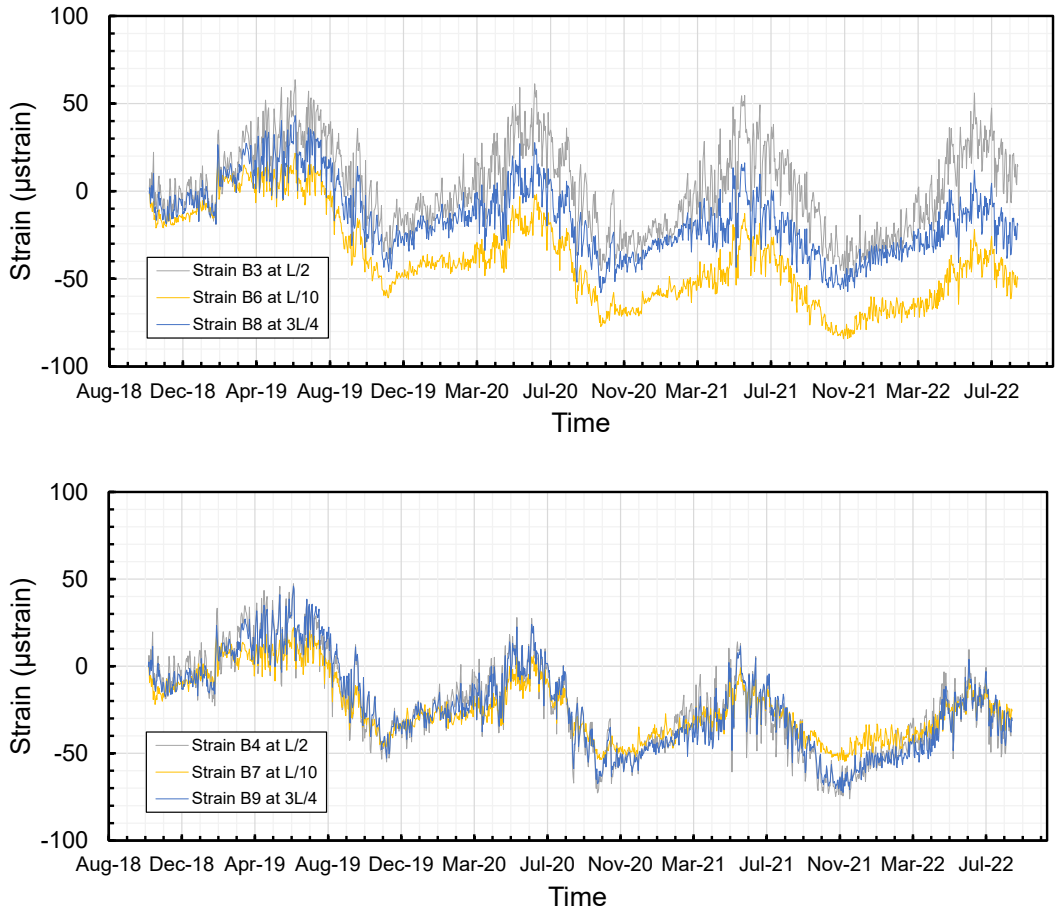

Figure 3.13. Strain time histories of gauges between the beams in steel-reinforced bridge deck (27W36)

The strain changes started with a similar behavior over the first six months of the data recording period. Although the gauges placed on the east side showed an almost similar behavior over time (maximum and minimum values of 47 and -76 µstrain, respectively), separation was noted in the daily average strain trends of the gauges placed on the west side, with lower compressive strains at mid-span

(maximum and minimum values of 64 and -51 µstrain) and higher compressive strains at L/10 (maximum and minimum values of 22 and -84 µstrain). The gauges at L/2 showed (relatively) high tensile strains that could be indicators of cracks. The graph also demonstrated negligible reduction in peak tensile strains and more variation for gauge B3 compared to the other gauges. The gauges also progressively showed higher compressive and lower tensile strains compared to the gauges located over the beams after the first six months.

Figure 3.14 shows the daily average strain time histories of the gauges placed over the middle axis of the GFRP-reinforced bridge deck (27W37) in the transverse direction.

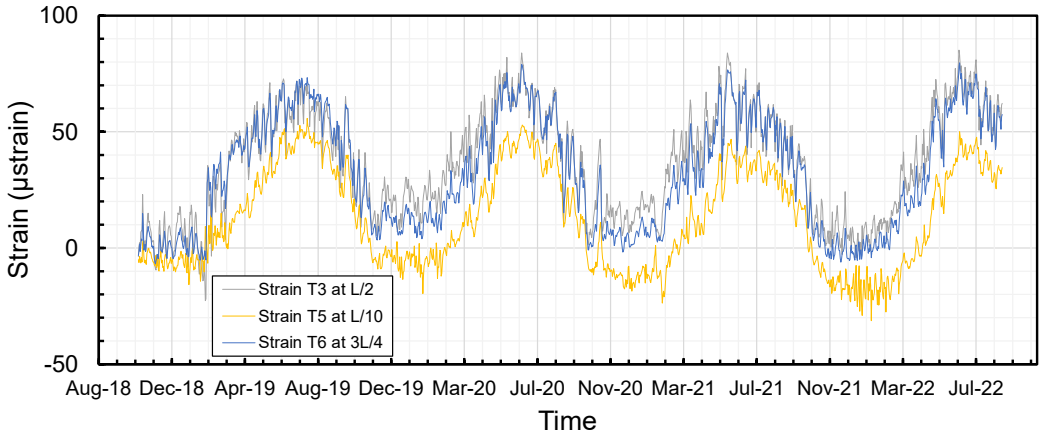

Figure 3.14. Strain time histories of gauges at the middle axis/beamline in GFRP-reinforced bridge deck (27W37)

The tensile and compressive strains at L/10 (maximum and minimum values of 56 and -31 µstrain) were lower and higher than those recorded in gauges T3 and T6, i.e., with maximum tensile strains of 85 and 80 µstrain and maximum compressive strains of 23 and 7 µstrain, respectively. On comparison between Figures 3.12 and 3.14, higher tensile and lower compressive strains were observed overall for the GFRP-reinforced bridge deck. In addition, the graphs in Figure 3.14 followed trends similar to those in Figure 3.12.

The daily average strain time histories between the beams of the GFRP-reinforced bridge deck (27W37) along the transverse direction are shown in Figure 3.15.

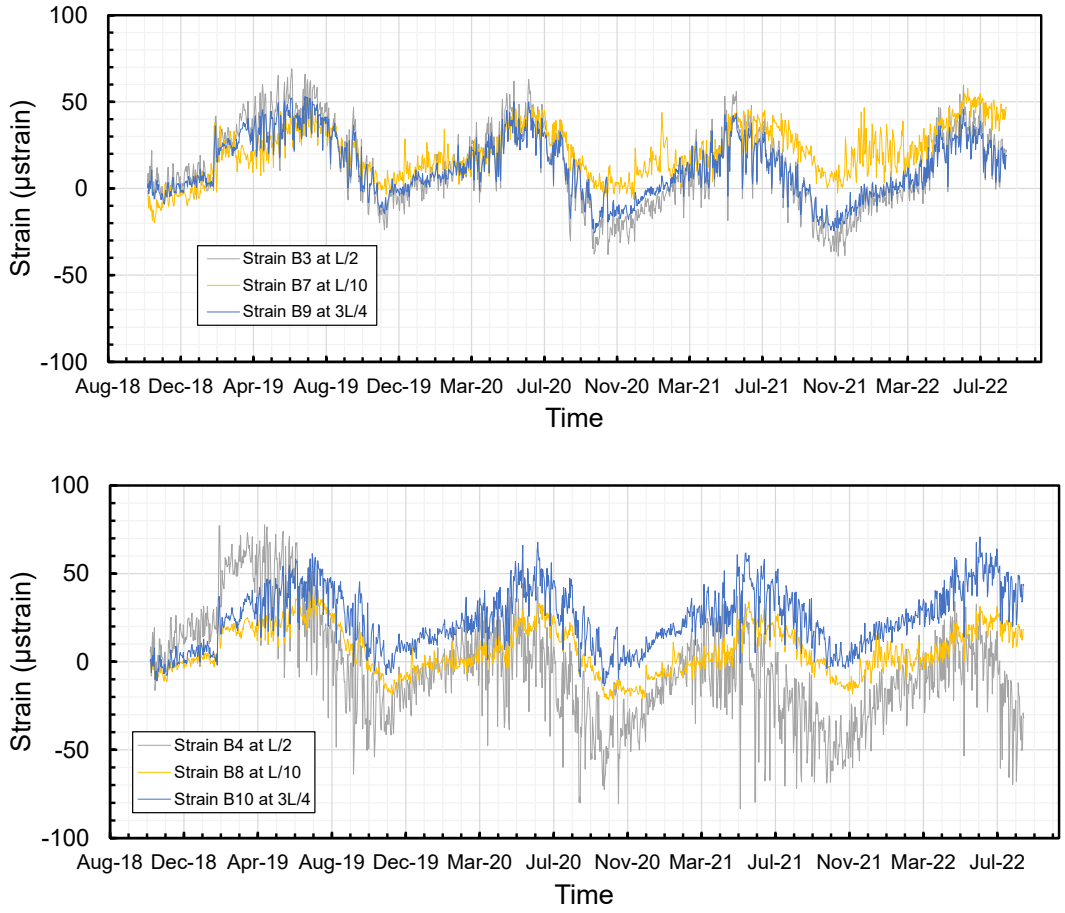

Figure 3.15. Strain time histories of gauges between the beams in GFRP-reinforced bridge deck (27W37)

The gauges showed an almost similar behavior along the west side of the middle beam before July 2020. Gauge B7 indicated higher tensile strains after that. Gauges B3, B7, and B9 reported maximum and minimum strains of 69, 58, 53 and -39, -20, -25 µstrain, respectively. On the east side, the B8 and B10 gauges followed a similar pattern (maximum and minimum values of 38, 71 and -22, -13 µstrain, respectively), with the B10 gauge showing higher tensile and lower compressive strains. However, the mid-span showed a different behavior, indicating more fluctuations, as well as higher maximum tensile/compressive strains (maximum and minimum values of 78 and -63 µstrain, respectively) and an overall decreasing trend over the years.

While the strains at L/10 on the east side decreased slightly over the years, their counterpart on the west side increased in recent years. The comparison between the gauges at 3L/4 suggested that the strains decreased on the west side and increased on the east side. The high tensile strains were also captured on the east side. Although the strains of the gauge on the west side of the slab at L/2 showed the possibility of hairline cracks, the strains decreased slightly over time. On the other hand, gauge B4 met the highest captured strain in April 2019. After that, large fluctuations were seen, reducing over the years and moving mostly toward compressive strains.

Figure 3.16 presents the daily average strain time histories of the steel-reinforced bridge deck (27W36) at the L/10 length.

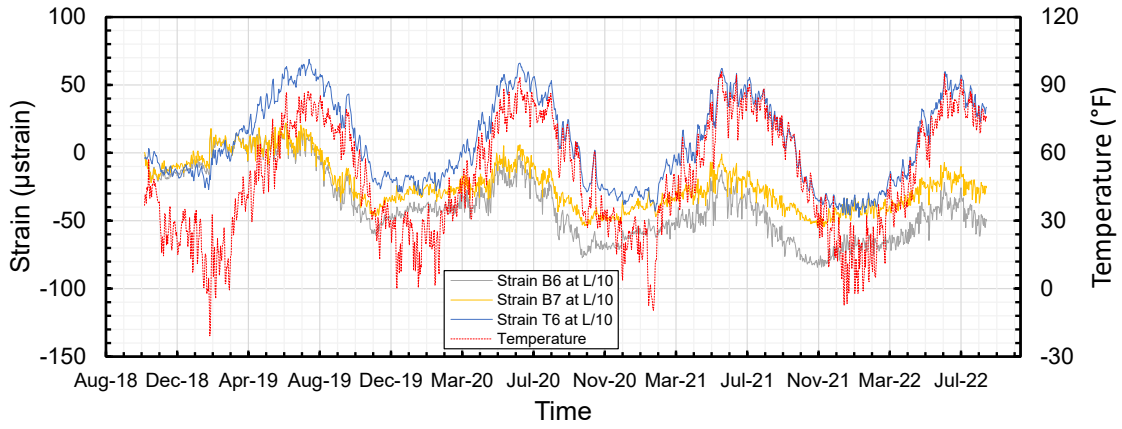

Figure 3.16. Strain time histories of gauges at L/10 length in steel-reinforced bridge deck (27W36)

The tensile strain peaks of the three gauges occurred in the summer of each year, corresponding to the peaks of daily average temperatures. The recorded data reflected considerable variations in both tensile and compressive peak strains at all gauges excluding the peak tensile strain with small changes at gauge T6. Also, gauges B6 and B7 were majorly in compression while gauge T6 was in tension over the warm seasons and in compression on the cold days.

Figure 3.17 shows the daily average strains versus time at the mid-span of the steel-reinforced bridge deck (27W36).

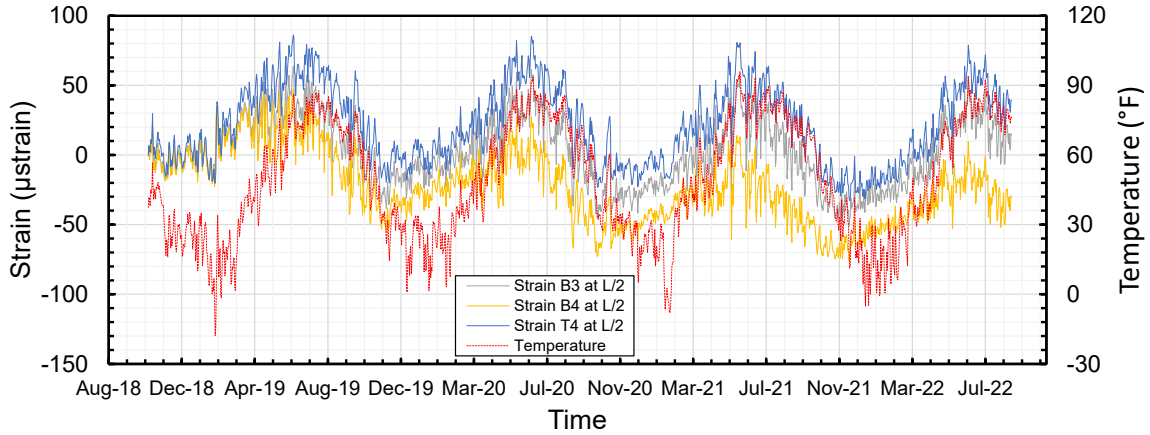

Figure 3.17. Strain time histories of gauges at mid-span in steel-reinforced bridge deck (27W36)

The strain changes showed an oscillation between compressive and tensile strains at gauges T4 and B3 over the years. A similar oscillation, although with a higher range, is noted for gauge B4, moving mostly toward compressive strains over the years.

Figure 3.18 shows strain time histories of the steel-reinforced bridge deck (27W36) at 3L/4.

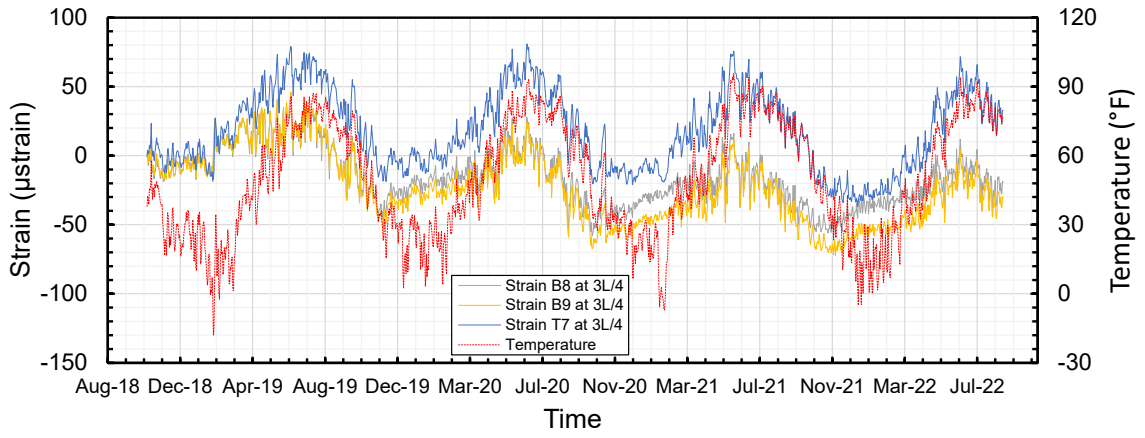

Figure 3.18. Strain time histories of gauges at 3L/4 in steel-reinforced bridge deck (27W36)

While gauges B8 and B9 followed an almost similar trend over time, especially in compression after the first year of data recording, gauge T7 showed a variation between compressive and tensile strains in different years. The three sets of data also showed more variation in the strain at the top of the deck over the middle beam at L/2 and 3L/4 (compared to L/10). The gauges on the east side of the middle beam showed an almost similar behavior, but the gauges on the west side showed different trends with lower compressive strains at mid-span and overall higher compressive strains at L/10. This observation was consistent with the plots of strain in the transverse direction.

Overall, the peak tensile strains of the top steel bars did not show considerable change in different years. The peak tensile strains of the bottom bars generally decreased over time. Nevertheless, gauge B3, which output the maximum tensile strain among all nine of the gauges, tended to report tensile strain peaks with low changes during the data recording period. Furthermore, the variation range of the graph at L/2 was larger than that of the other two.

Figure 3.19 shows the daily average strains versus time at L/10 of the GFRP-reinforced bridge deck (27W37).

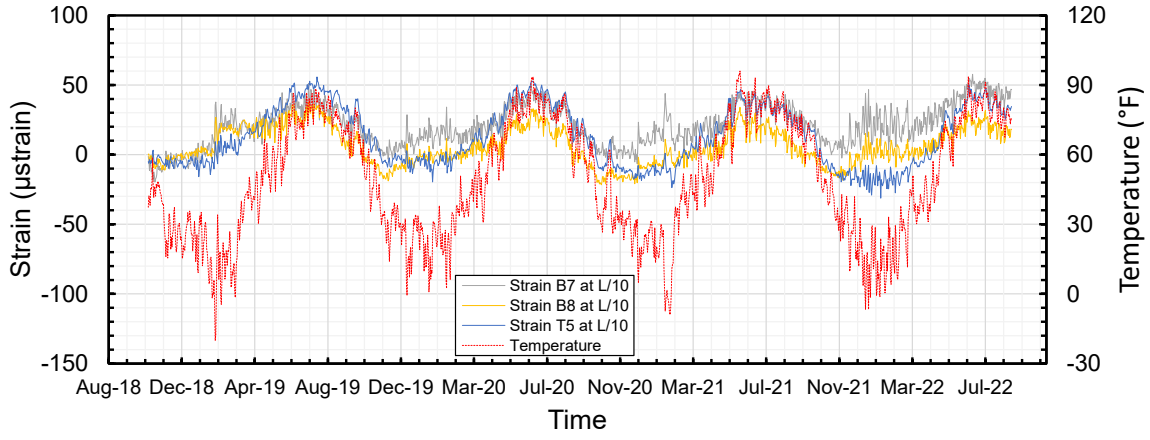

Figure 3.19. Strain time histories of gauges at L/10 in GFRP-reinforced bridge deck (27W37)

The three gauges followed an almost similar trend over warm days and slightly separated patterns in the winters. The plots showed less variation with lower tensile and compressive strains compared to the same locations in the steel-reinforced bridge deck (27W36).

On comparison between the steel and GFRP bars at L/10, the top bar graphs showed higher tensile and compressive strain peaks for the steel-reinforced bridge deck (27W36). As for the bottom bars, the GFRP rebar tended to mostly stay in the tension zone, while the steel reinforcement generally descended over time.

The strain values versus time at the mid-span of the GFRP-reinforced bridge deck (27W37) is shown in Figure 3.20.

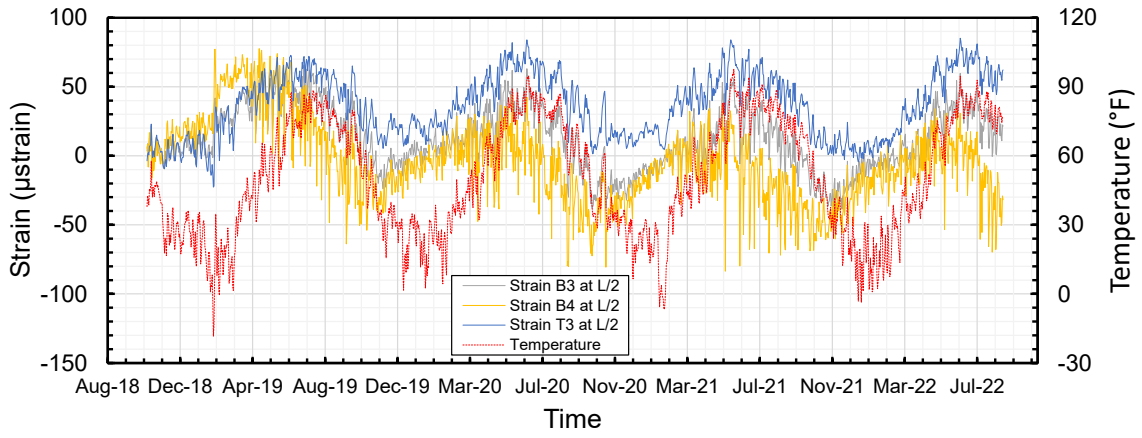

Figure 3.20. Strain time histories of gauges at mid-span in GFRP-reinforced bridge deck (27W37)

While gauge T3 showed a generally tensile strain over the years, gauges B3 and B4 oscillated between tensile and compressive strains. Gauge B4 also indicated slightly higher tensile strains over the first six months and higher compressive strains over the rest of the data recording time with more fluctuations.

According to Figures 3.17 and 3.20, the top and bottom bars in both bridges showed similar behaviors. While the top bar tensile strain peaks decreased slightly for the steel bars, they showed a slight increase for the GFRP bars. Also, the fluctuations in the strains of gauge B4 were considerable compared to the same location in the steel-reinforced bridge deck (27W36).

Figure 3.21 presents the strain time histories recorded by the gauges at 3L/4 of the GFRP-reinforced bridge deck (27W37).

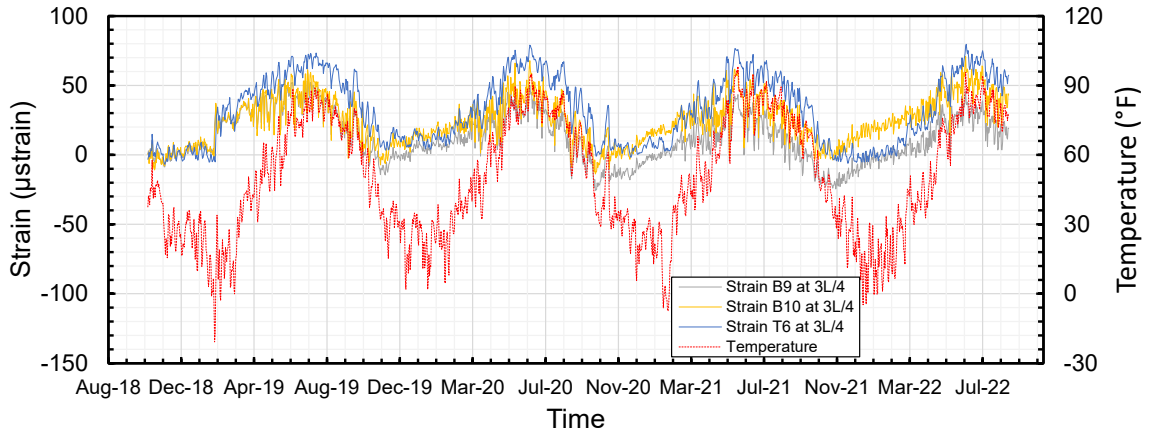

Figure 3.21. Strain time histories of gauges at 3L/4 in GFRP-reinforced bridge deck (27W37)

The strain at gauges T6 and B10 were generally in tension, while gauge B9 showed a variation between compressive and tensile strains over the years, noting that the compressive strain peaks increases. According to the three sets of data, the gauge at the top of the deck over the beam (i.e., T6) output more compressive strains at L/10 than L/2 or 3L/4. The gauges for the west side of the beam showed similar trends, with the gauges at L/10 capturing generally lower compressive strains. The strain values for the east side of the beam also showed that the mid-span was under higher compressive strains compared to L/10 and 3L/4.

Comparing the tensile strains of the two bridge decks at 3L/4 indicated that the top bars behaved similarly, while the bottom bars followed different trends. As such, the GFRP bottom bars were mostly in tension with small changes in the peak values, but the steel bar tensile strain peaks went down over time.

Figure 3.22 shows the monthly average, maximum, and minimum strain values in gauge T6 of the steel-reinforced bridge deck (27W36) and gauge T5 of the GFRP-reinforced bridge deck (27W37).

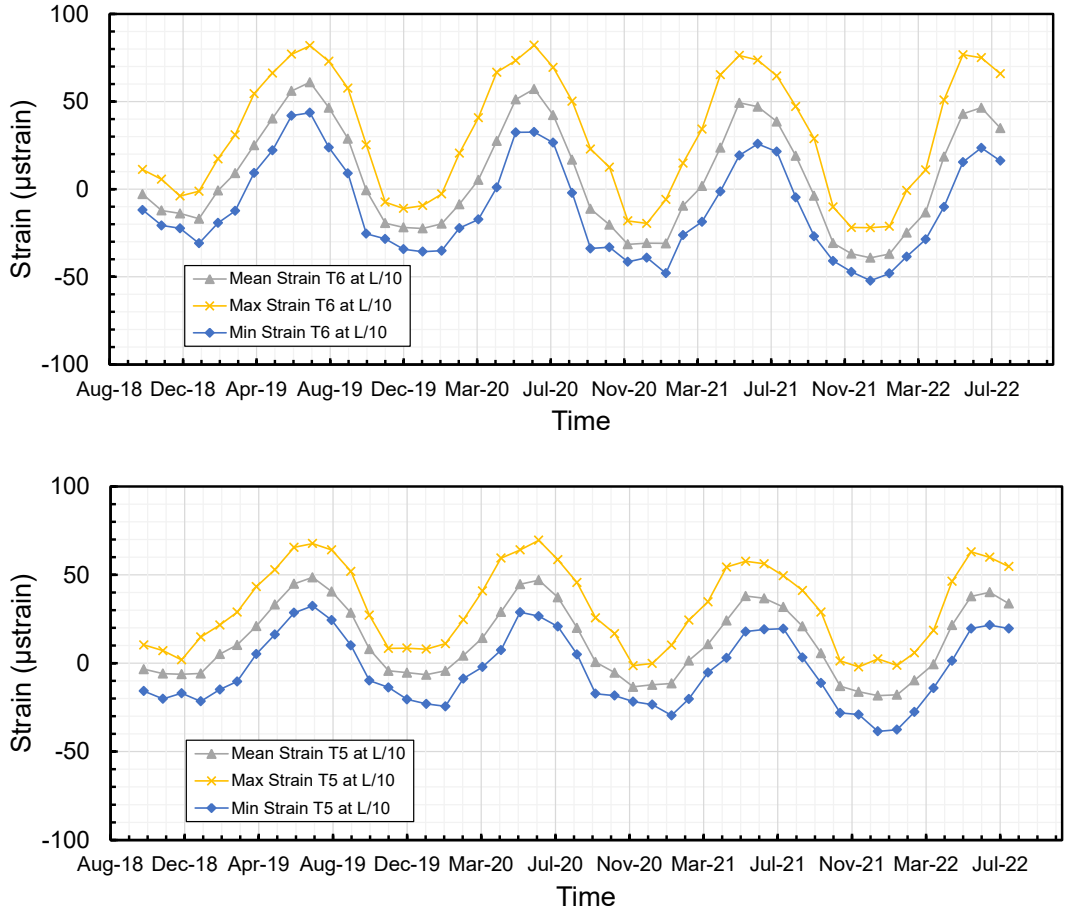

Figure 3.22. Strain time histories of gauge T6 of steel-reinforced bridge deck (27W36) and gauge T5 of GFRP-reinforced bridge deck (27W37)

The recorded maximum ranges were (-22 to 82 µstrain) and (-2 to 70 µstrain) for the steel- and GFRP-reinforced bridge decks, respectively. On the other hand, the recorded minimum ranges were (-52 to 44 µstrain) and (-39 to 32 µstrain) for the steel-reinforced (27W36) and GFRP-reinforced (27W37) bridge deck, respectively. Moreover, the average strain values of the steel-reinforced bridge deck (27W36) were between -39 and 61 µstrain, while the same values for the GFRP-reinforced bridge deck (27W37) ranged between -18 and 49 µstrain. The results showed that the maximum, minimum, and average monthly strains of the steel bars covered larger ranges than the GFRP bars at L/10. Although the maximum tensile strains were not high, the inspections revealed cracks at L/10 in both bridge decks. Considering that the cracks might not cross the locations of the sensors, the gauges failed to capture the cracks.

Figure 3.23 indicates the monthly strain data at gauge B3 of both the steel-reinforced and GFRP-reinforced bridge decks.

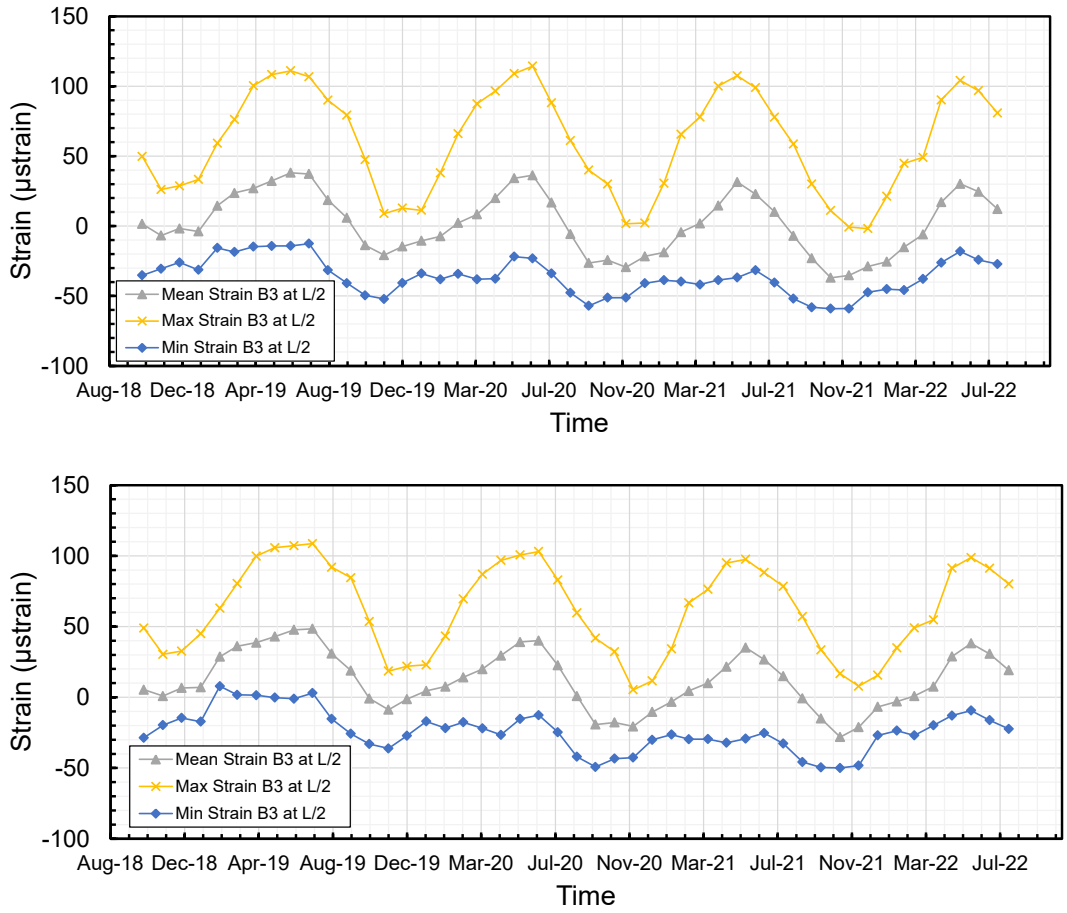

Figure 3.23. Strain time histories of gauge B3 of steel-reinforced bridge deck (27W36) and gauge B3 of GFRP-reinforced bridge deck (27W37)

The maximum strain values of the steel-reinforced bridge deck (27W36) and the GFRP-reinforced bridge deck (27W37) ranged between -2 and 114 µstrain and 5 and 109 µstrain, respectively. The tensile strains were consistent with the cracks that were detected on the bottom face of both bridges along the mid-span. On the other hand, the minimum strain values of the steel-reinforced bridge deck (27W36) were between -59 and -13 µstrain, while the same values for the GFRP-reinforced bridge deck (27W37) ranged between -50 and 8 µstrain. The recorded average value ranges were (-37 to 38 µstrain) and (-28 to 48 µstrain) for the steel-reinforced bridge deck (27W36) and the GFRP-reinforced bridge deck (27W37), respectively. The graphs indicated good agreement between the trends of the two bridge decks at L/2. All the trends showed almost similar behaviors with slight changes over time.

The monthly average, maximum, and minimum of the strain values at gauges T7 of the steel-reinforced bridge deck (27W36) and gauge T6 of the GFRP-reinforced bridge deck (27W37) are shown in Figure 3.24.

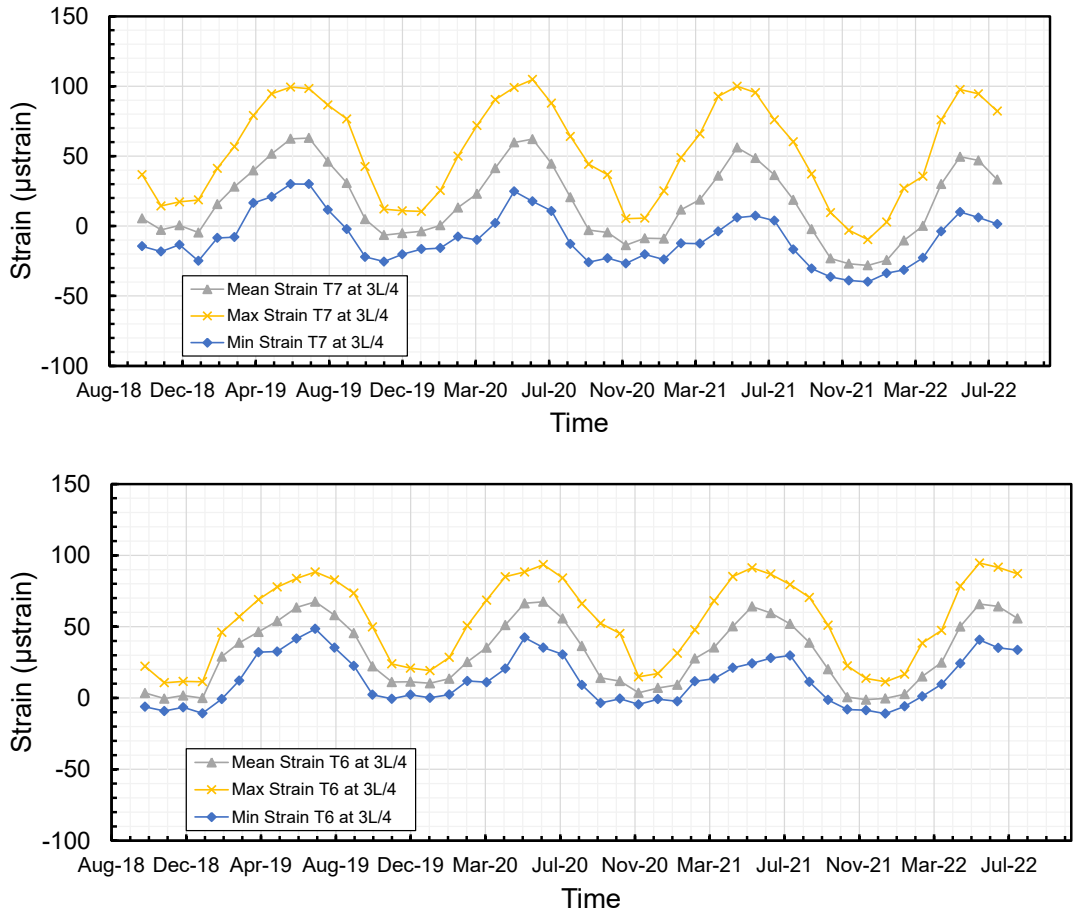

Figure 3.24. Strain time histories of gauge T7 of steel-reinforced bridge deck (27W36) and gauge T6 of GFRP-reinforced bridge deck (27W37)

The strain value ranges of the steel-reinforced bridge deck (27W36) were -28 to 63 µstrain, -10 to 105 µstrain, and -40 to 30 µstrain for the average, maximum, and minimum values, respectively. On the other hand, the strain gauges showed ranges of -1 to 67 µstrain, 11 to 95 µstrain, and -11 to 48 µstrain for the average, maximum, and minimum values of the GFRP-reinforced bridge deck (27W37), respectively. Accordingly, the strain variations recorded in the GFRP bars at 3L/4 were lower than the steel bars, and lower compressive strains were also reported for the steel bars. In addition, some transverse cracks were seen over 3L/4 of the two bridge decks, which aligned with the strain recordings.

Figure 3.25 shows the recorded strains for three selected temperatures of 10°F, 50°F, and 70°F at gauges T6, B3, and T7 in the steel-reinforced bridge deck (27W36).

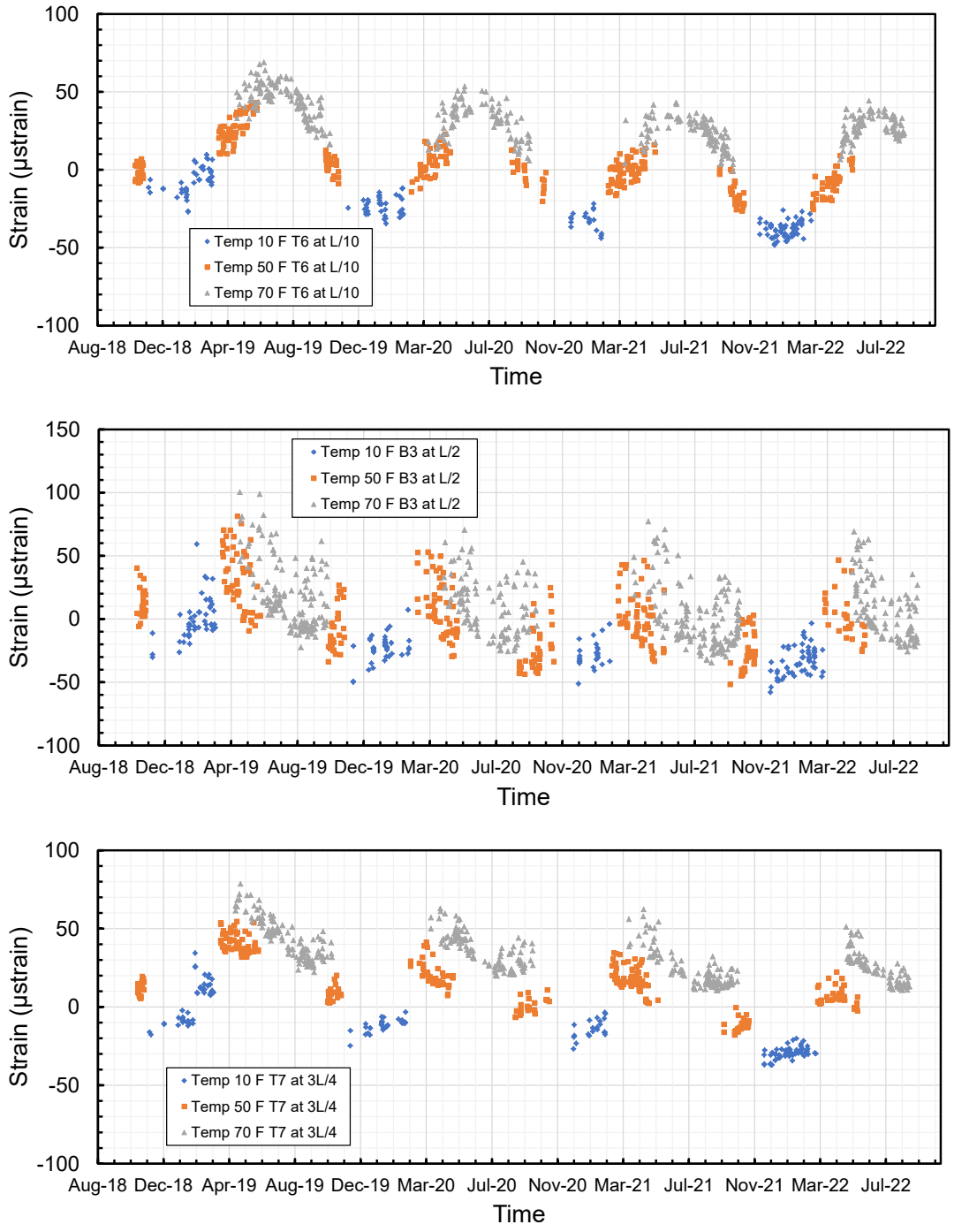

Figure 3.25. Strain time histories of gauges T6, B3, and T7 of steel-reinforced bridge deck (27W36) at 10°F, 50°F, and 70°F

The average compressive strain at 10°F increased in all three gauges with generally lower values at 3L/4. Under a temperature of 50°F, the strains at L/10 decreased in every subsequent fall and spring season, trending mostly to compressive strains after spring 2021. The same pattern applied to strains at L/2 and 3L/4; however, the strains generally increased every subsequent fall. At L/10, the strains increased to the peak and decreased afterwards during the summer at 70°F, while the peaks decreased over the

years. On the other hand, the strains decreased over the summer and generally over the years with the same temperature at L/2 and 3L/4. In addition, the recorded values at the three temperatures showed more variation at L/2 in comparison with the other two locations.

Figure 3.26 shows the strain values from the GFRP-reinforced bridge deck (27W37) for temperatures of 10°F, 50°F, and 70°F at gauges T5, B3, and T6.

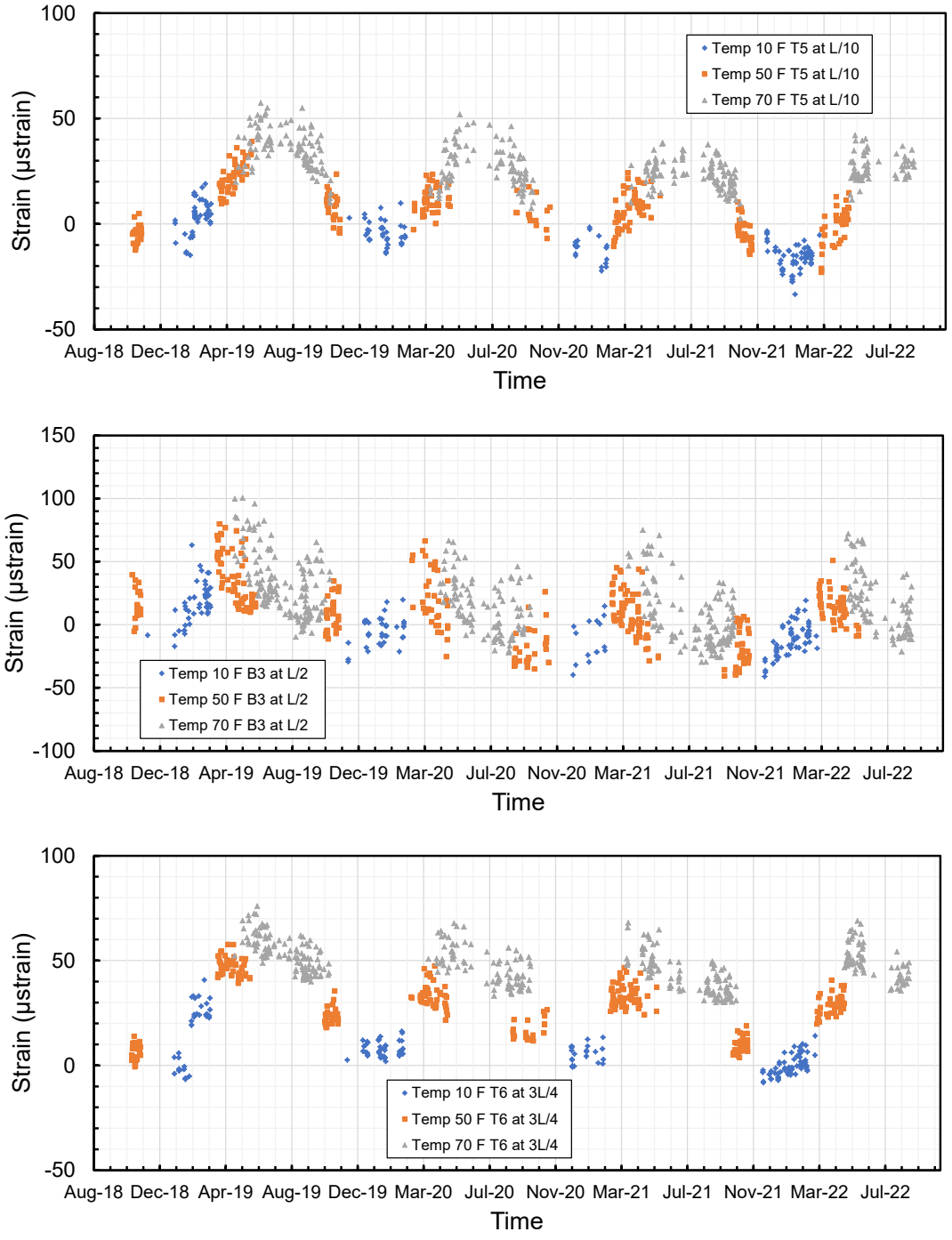

Figure 3.26. Strain time histories of gauges T5, B3, and T6 of GFRP-reinforced bridge deck (27W37) at 10°F, 50°F, and 70°F

The processed data showed decreasing strains at 10°F, which changed from tensile strains to compressive strains in winter 2020 at L/10 and L/2. At 50°F, the strains followed an overall decreasing trend with an increase every spring at all three gauges. Bars at L/10 were generally in tension before fall 2021, compressive strains were dominant in fall 2020 and 2021 at mid-span, and the strains were mainly

tensile at 3L/4. At 70°F, the strains followed the same pattern as for the steel-reinforced bridge deck (27W36).

The comparison between Figures 3.25 and 3.26 showed a similar behavior between gauges with higher compressive strains for the steel bars at L/10 and higher tensile strains in GFRP bars at L/2 and 3L/4.

Figure 3.27 shows the maximum and minimum annual temperatures and their corresponding strains in gauge T6 of the steel-reinforced bridge deck (27W36) and gauge T5 of the GFRP-reinforced bridge deck (27W37).

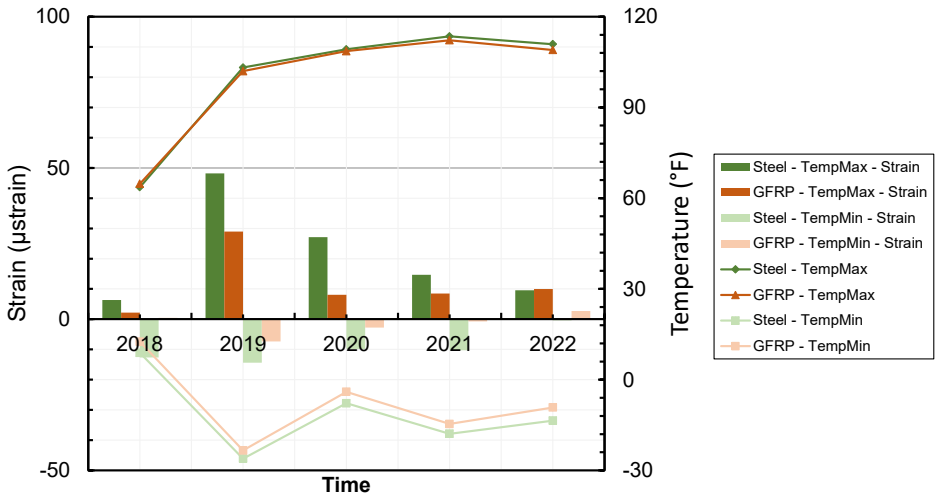

Figure 3.27 Annual maximum and minimum temperatures and their corresponding strains in gauge T6 of steel-reinforced bridge deck (27W36) and gauge T5 of GFRP-reinforced bridge deck (27W37)

Considering that the data recording started in October 2018, the maximum temperature in 2018 did not exceed 65˚ F. However, as the data collection continued through subsequent years, a maximum temperature of 104˚ F was recorded in 2019. The temperature increase led to bridge deck expansion, causing (relatively) large tensile strains in both steel and GFRP bridge decks.

At the early age, the cold season and shrinkage effects tended to contract the bridge deck, especially in the transverse direction, as the bridge deck has no constraint in that direction. This was captured in the compressive strains recorded in the transverse bars. Figure 3.28 shows the strains related to the maximum and minimum temperatures of each year at gauge B3 in both the steel-reinforced and GFRP-reinforced bridge decks.

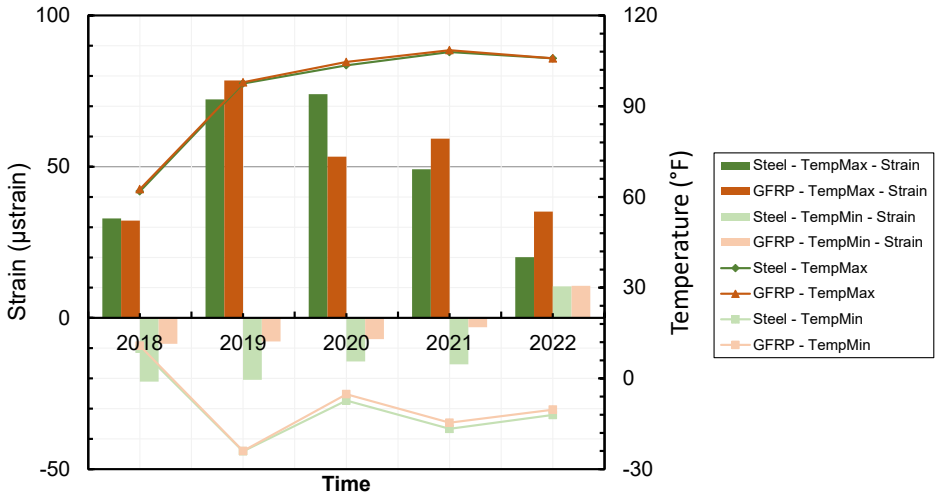

Figure 3.28. Annual maximum and minimum temperatures and their corresponding strains in gauge B3 of steel-reinforced bridge deck (27W36) and GFRP-reinforced bridge deck (27W37)

The strains corresponding to the maximum and minimum temperatures followed the same patterns as that recorded by the gauges at L/10. However, the tensile and compressive strains were much higher at L/2 than L/10. In addition, the tensile strains in the GFRP bars were higher than in the steel bars in most of the years. Although the temperature gradient and the concrete shrinkage should induce compressive strains in the bottom of the deck between the beams, the high temperature and external load may reverse the recordings to the tensile strain. Thus, the strains corresponding to the maximum temperatures were mainly in tension, generally decreasing over the years due to shrinkage and the temperature gradient. On the other hand, the low temperatures resulted in concrete contraction, which induced compressive strains in the bars. This effect decreased and even reversed over time as a result of the temperature gradient and external loads. Overall, the tensile strains of the GFRP-reinforced bridge deck (27W37) were larger than the strains of the steel-reinforced bridge deck (27W36) at the referenced location.

Figure 3.29 shows the maximum and minimum annual temperatures and their corresponding strains in gauge T7 of the steel-reinforced bridge deck (27W36) and gauge T6 of the GFRP-reinforced bridge deck (27W37).

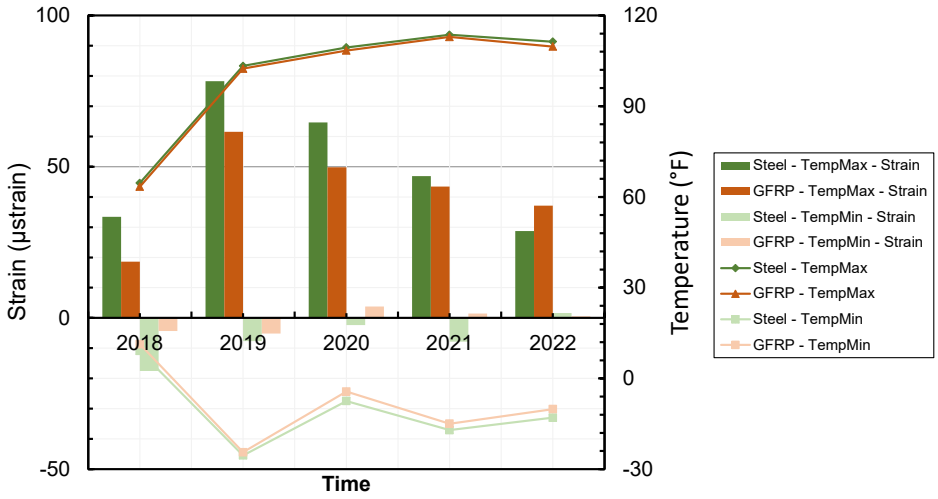

Figure 3.29. Annual maximum and minimum temperatures and their corresponding strains in gauge T7 of steel-reinforced bridge deck (27W36) and gauge T6 of GFRP-reinforced bridge deck (27W37)

The strain change pattern in response to the maximum temperatures was similar to the changes in the other two gauge locations. As for the minimum temperature, gauge T7 mainly showed compressive strains decreasing and increasing slightly over the years. On the other hand, gauge T6 showed a decrease in the compressive strains until 2020 and in tensile strains afterwards. However, the tensile strains related to the maximum temperature in the steel-reinforced bridge deck (27W36) were higher than the same strains in the GFRP-reinforced bridge deck (27W37) at 3L/4. Again, tensile strains in the GFRP bars exceeded the strains of the steel bars in 2022.

3.6 SUMMARY

The long-term monitoring of the bridge decks reinforced with steel and GFRP bars through transverse strain recordings and bridge inspections were discussed in this chapter. The tensile strains, recoded along the length and width of the bridges, were consistent with the cracks detected during the inspections at most of the sensor locations. However, some gauges failed to show the cracking strains due to the lack of overlap between the gauge locations and the crack paths. It should be noted that the concrete cracking strain can be considered to be in the range of 100 µstrain. One-way action for the transverse direction forms tensile strains in the top bars of the concrete deck (at the girder lines) and in the bottom bars of the concrete deck (between the girders).

The final inspection also revealed transverse cracks concentrated mostly near the abutments in both bridge decks. Several factors might have caused the formation of the cracks away from the middle part of the integral bridges. The shrinkage effects of the cast-in-place decks over the precast beams might result in crack formation in the concrete decks. The temperature gradient in the cold and warm days of a year might amplify the shrinkage effect in some cases. Also, the stiffness property of the integral bridges might lead to some fixity effects near the abutments, resisting against the deck movement under the temperature and traffic loads. Consequently, cracks formed on the deck slabs close to the abutments, which could lead to a release in the slab-abutment joints, moving from the full fixity to the

partial fixity. Overall, both bridge decks showed almost similar behaviors and crack patterns during the years.

CHAPTER 4: LIVE LOAD TESTING

The objective of the live load tests performed on the two bridges immediately after construction was to understand how the decks structurally transfer wheel loads from their points of application to the bridges' supports. The magnitude of stresses and strains that develop in the deck while transferring the load is also important. Such information can be used to compare the performance of the GFRP-reinforced deck with that of the steel-reinforced deck, in terms of expected structural behavior and load-carrying mechanisms. The data obtained from the live load tests can also be used to assess the likelihood of immediate/long-term crack development in the bridge deck from vehicle loads.

To obtain a holistic assessment, gauge locations were selected to (1) capture extreme responses, (2) characterize the response in general, and (3) evaluate specific parameters, such as girder distribution factors. The test runs were conducted with a single truck passing over the bridge at a low speed. For this purpose, a Sterling Class 35 Model 14-6LLL dump truck was used after necessary coordination. The weights and dimensions of the loaded truck used in the live load tests are summarized in Figure 4.1.

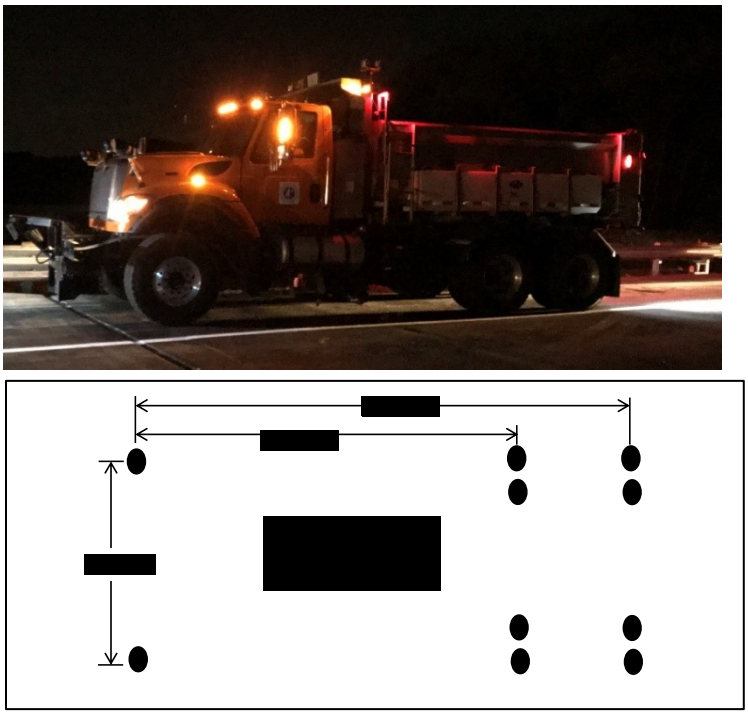

Figure 4.1 Dimensions and weights of the three-axle dump truck used for live load tests

4.1 LOAD PATHS

Several vehicle configurations were investigated to generate different shear and moment demands in the bridges. The live load tests were performed with the truck moving at approximately 5 mph. The information collected in these tests was in the form of continuous data as a function of truck position on the bridge decks. This was found to be more efficient than placing the truck at specific locations because it provided a holistic perspective of the bridges' response to live loads. For the steel-reinforced bridge

deck (27W36), a total of seven longitudinal paths were considered. The load paths were labeled 1 through 7, as shown in Figure 4.2.

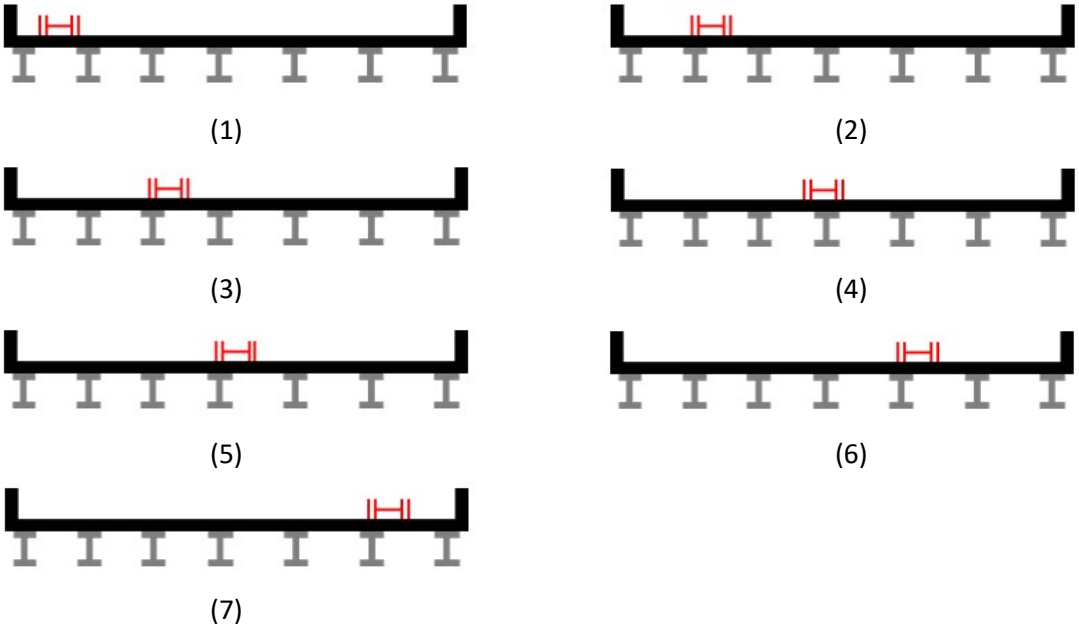

Figure 4.2 Truck positions for live load tests of steel-reinforced bridge deck (27W36)

Except for load case 1, all of the load paths were positioned directly over the girders. In the case of load case 1, the passenger-side wheels were placed 2 ft from the barrier. For the steel-reinforced bridge deck (27W36), a total of 14 test runs were conducted, i.e., two for each configuration shown in Figure 4.2.

For the GFRP-reinforced bridge deck (27W37), nine longitudinal truck paths were marked on the bridge deck before conducting the load tests. These nine longitudinal paths were used to guide the truck as it passed over the bridge. The positions were labeled 1 through 9, as shown in Figure 4.3.

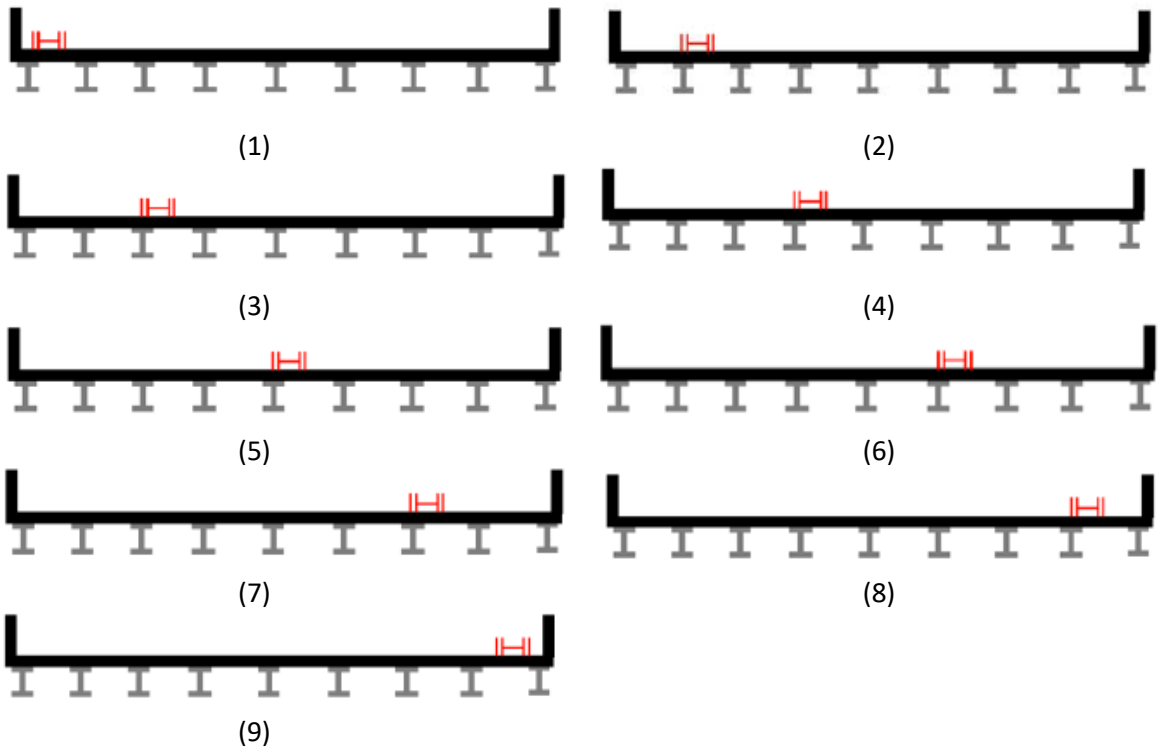

Figure 4.3 Truck positions for live load tests on GFRP-reinforced bridge deck (27W37)

To record the longitudinal position of the truck as it crossed the bridge, transverse lines were painted on the deck at 10 ft intervals. The nine truck positions were selected to characterize the deck response under the most critical loading combinations. For seven of the load cases, tire loads were positioned directly on the girders. Load cases 1 and 9 were exceptions, in which one of the wheels was placed 2 ft from the barrier. In total, the bridge was subjected to 18 test runs, i.e., two for each configuration shown in Figure 4.3.

4.2 INSTRUMENTATION FOR LIVE LOAD TESTS

For the live load tests, a dense array of strain transducers was temporarily attached to the deck and girders. The gauges used in the longitudinal direction primarily provided information about the global behavior of the bridge. The gauges were attached to the top surface of the bridge deck and the top and bottom of the girders. The transverse gauges were attached to the top of the bridge deck, providing information about the local deck behavior. The labeling of the gauges was done in such a way as to distinguish the gauges on the bridge deck from those on the girders. The gauges with a "D" prefix were used on the bridge deck, and the gauges with a "G" prefix were used on the girders.

For the steel-reinforced bridge deck (27W36), the positioning and details of the transverse and longitudinal gauges are shown in Figures 4.4 through 4.8.

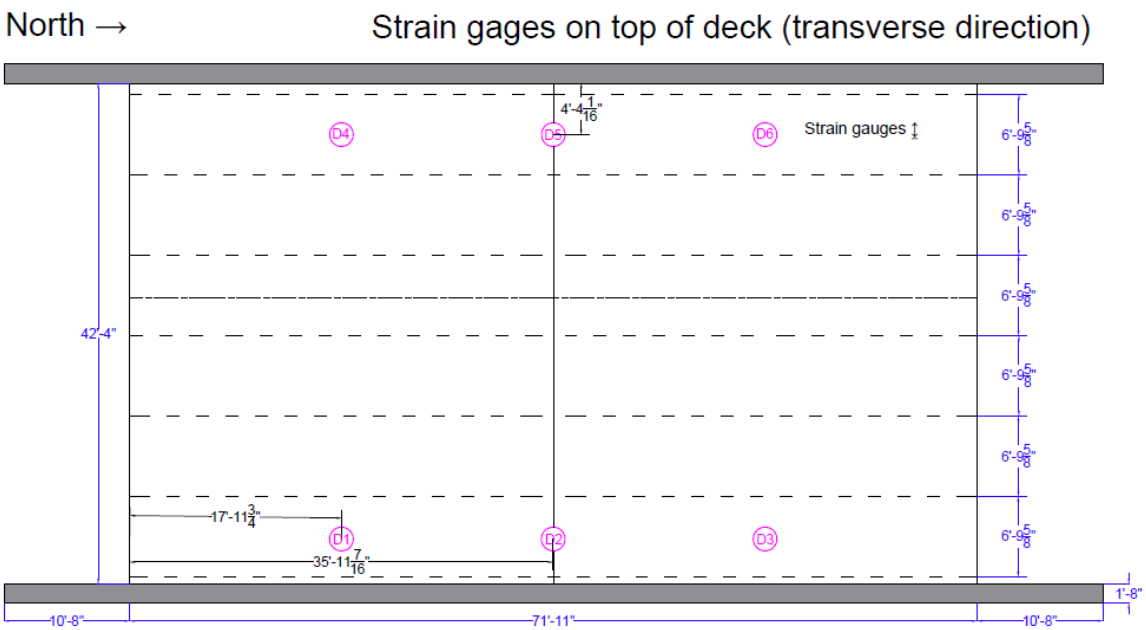

Figure 4.4 Strain gauge distribution on the top of the deck for live load testing of steel-reinforced bridge deck (27W36)

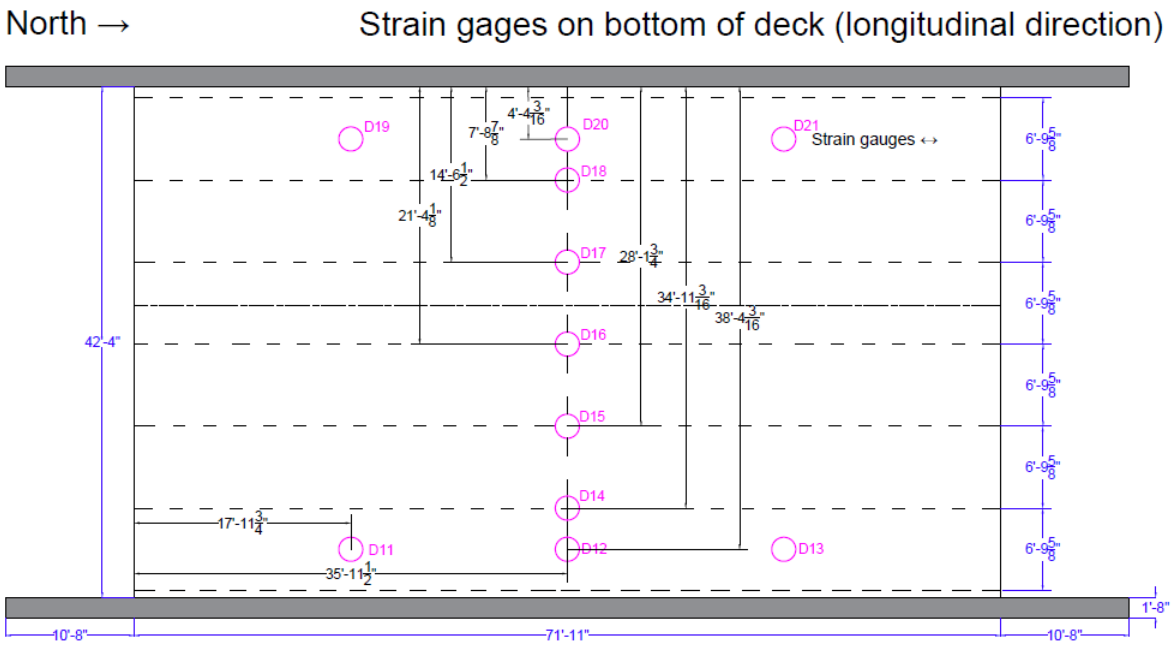

Figure 4.5 Strain gauge distribution on the bottom of the deck for live load testing of steel-reinforced bridge deck (27W36)

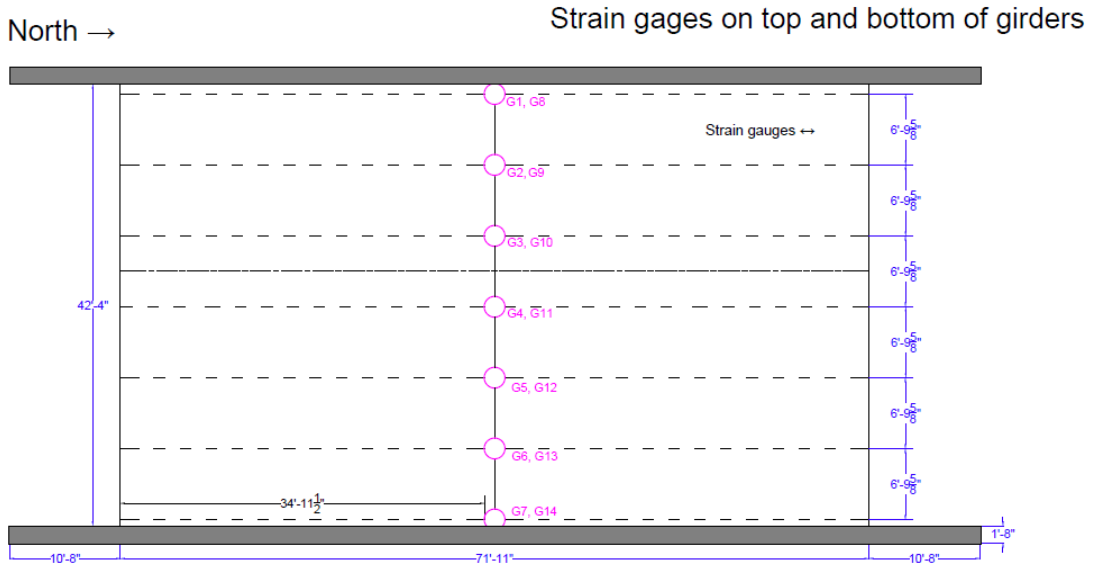

Figure 4.6 Strain gauge distribution on the top and bottom of girders for live load testing of steel-reinforced bridge deck (27W36)

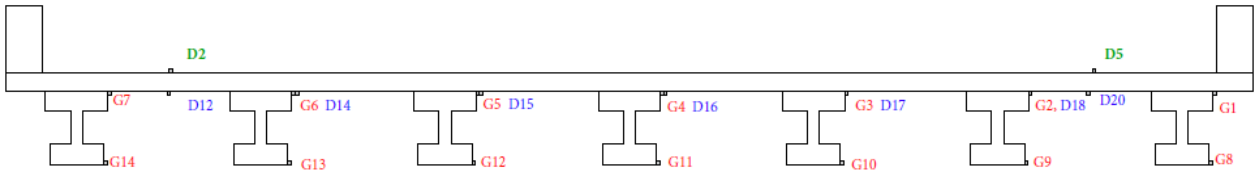

Figure 4.7 Strain gauge distribution at the mid-span for live load testing of steel-reinforced bridge deck (27W36)

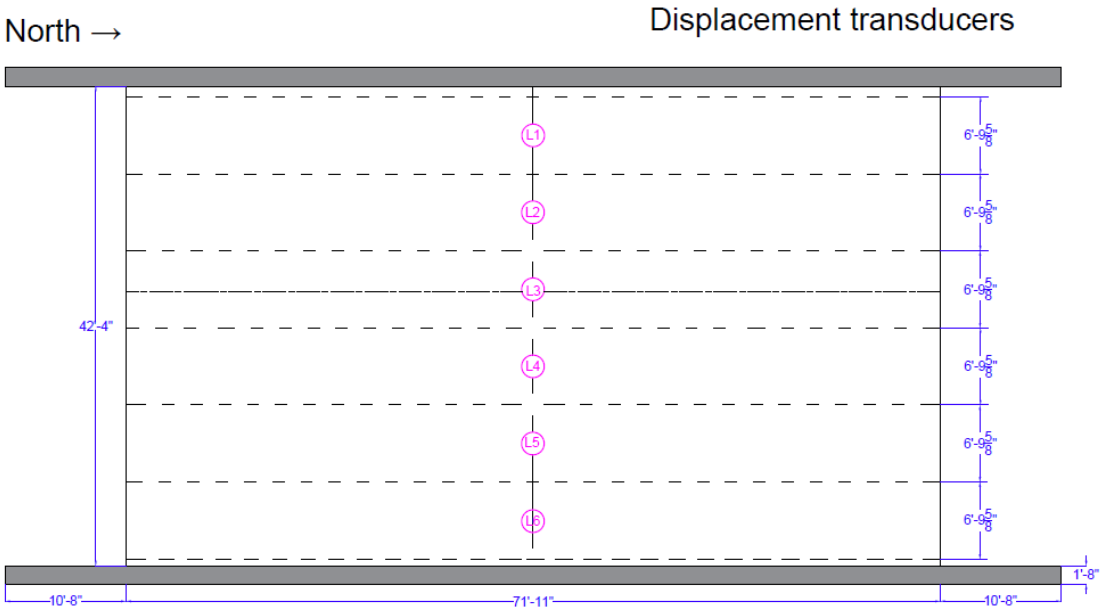

Figure 4.8 Distribution of displacement transducers for steel-reinforced bridge deck (27W36)

A set of six gauges was placed on the top of the deck to capture the deck's response in the transverse direction. To capture the deck's behavior in the longitudinal direction, a total of 25 gauges were placed underneath the bridge deck as well as on the top and bottom of the bridge girders. In addition to the BDI gauges, displacement transducers were used to measure the relative deflection of the bridge deck with respect to adjacent girders. This was done by using a wood plank placed between two adjacent girders. One end of the displacement transducer was then placed on the plank, with the other end attached to the bridge deck. In total, displacement was measured at 6 places in the bridge decks.

In the case of the GFRP-reinforced bridge deck (27W37), a total of 34 strain gauges were used (Figures 4.9 through 4.13). This was due to the fact that the GFRP-reinforced bridge deck (27W37) is wider than the steel-reinforced bridge deck (27W36).

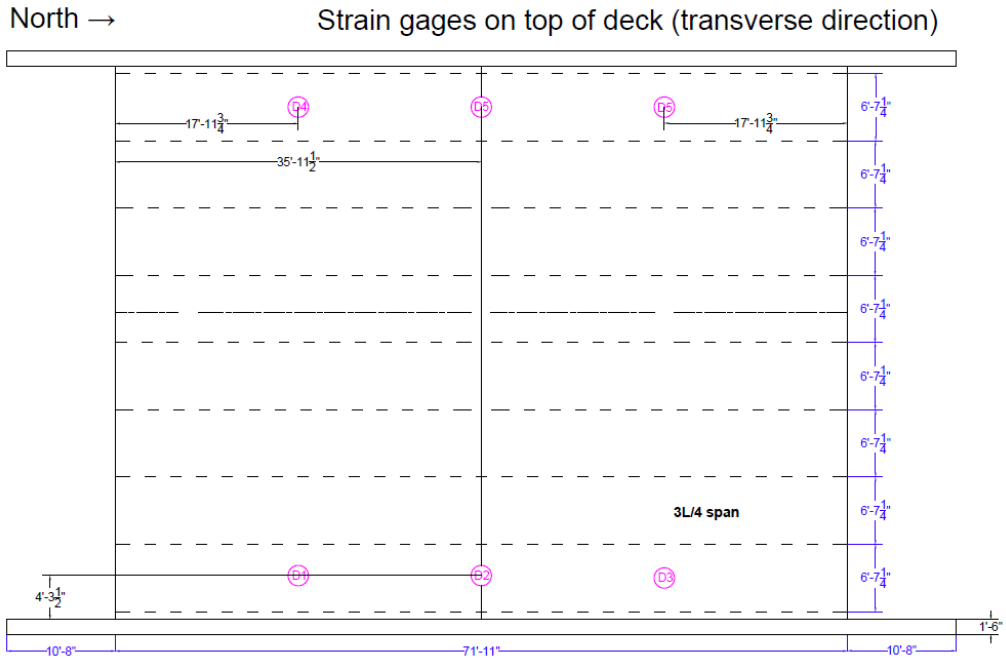

Figure 4.9 Strain gauge distribution on the top of the deck for live load testing of GFRP-reinforced bridge deck (27W37)

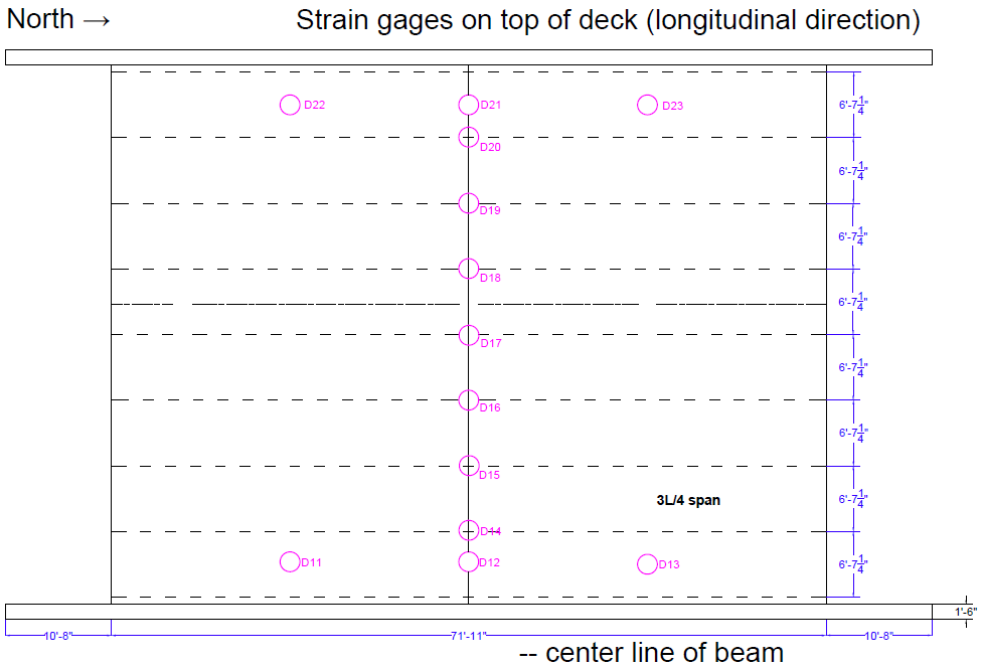

Figure 4.10 Strain gauge distribution on the bottom of the deck for live load testing of GFRP-reinforced bridge deck (27W37)

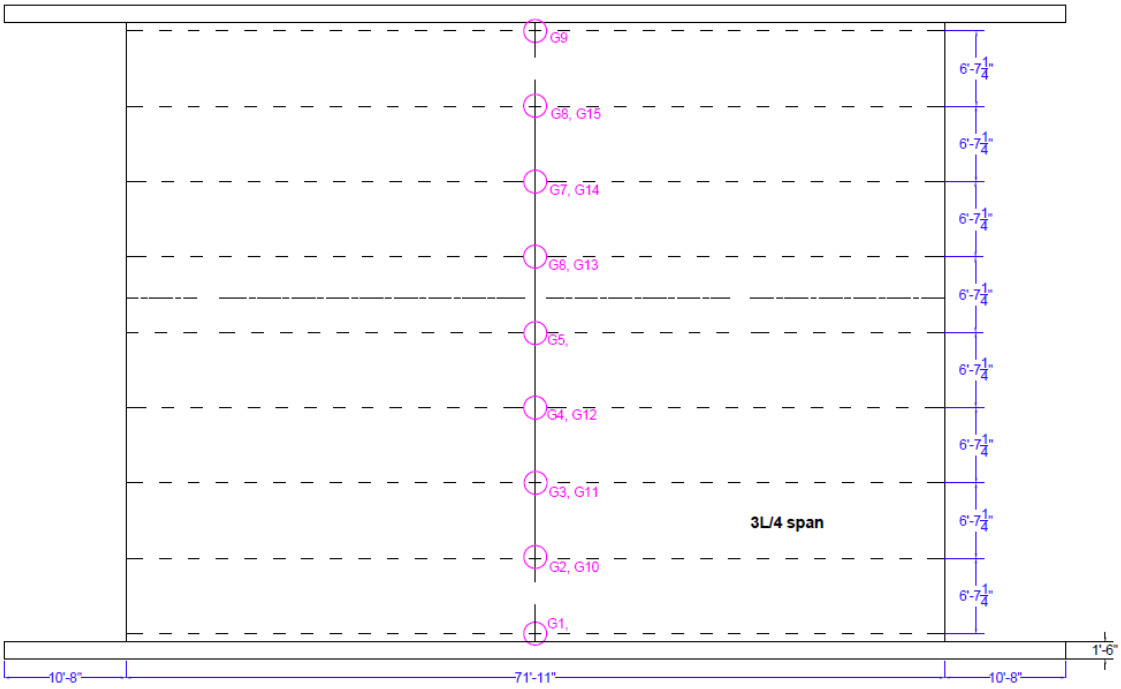

Figure 4.11 Strain gauge distribution on the top and bottom of the girder for live load testing of GFRP-reinforced bridge deck (27W37)

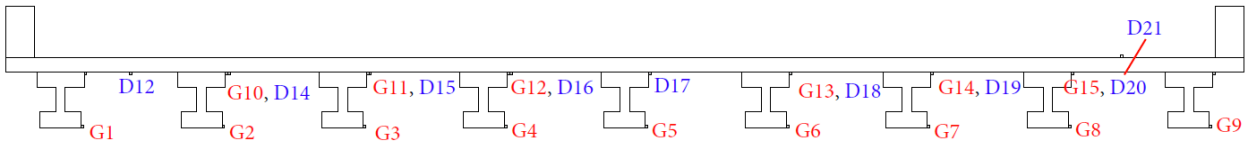

Figure 4.12 Strain gauge distribution at the mid-span for live load testing of GFRP-reinforced bridge deck (27W37)

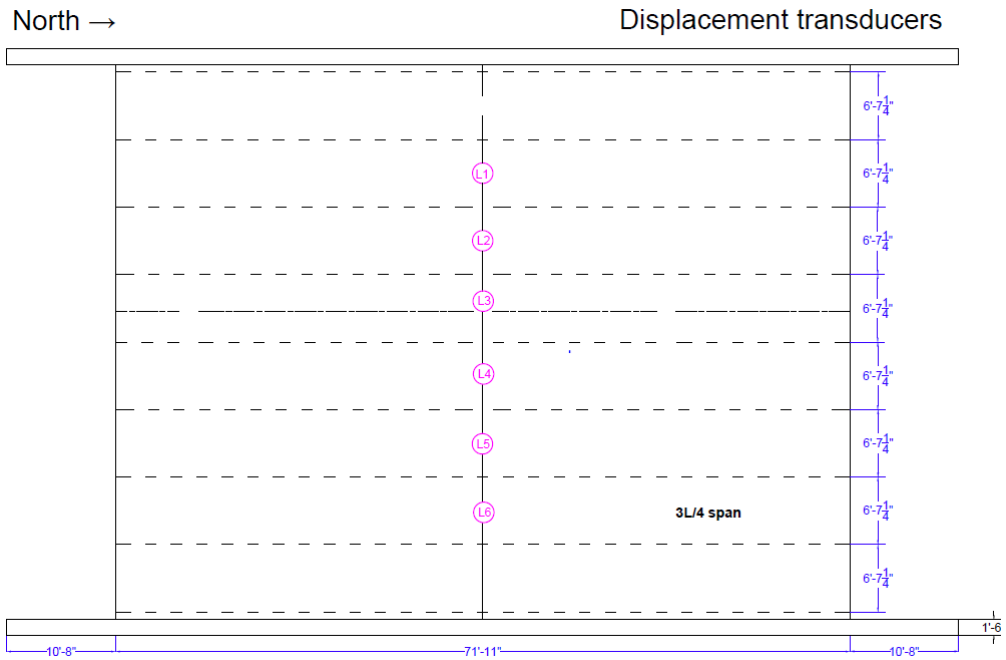

Figure 4.13 Distribution of displacement transducers for GFRP-reinforced bridge deck (27W37)

The gauges were made of aluminum and had a 3 in. effective gauge length (Figure 4.14).

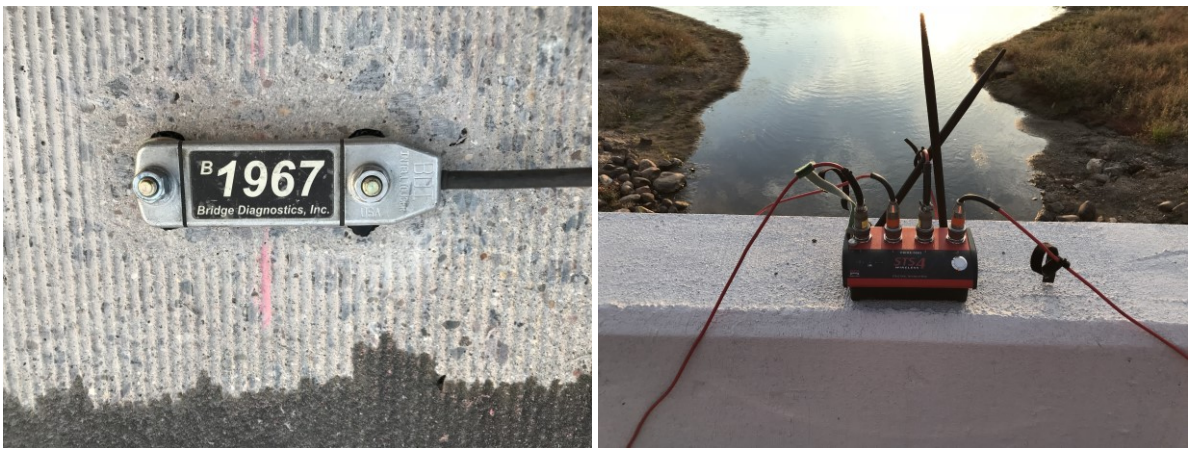

Figure 4.14 BDI Intelliducer gauge (left) and transmitter (right)

Extensions were used to obtain an average strain in the event of cracking in or near the gauged zone. During the testing, the data logger provided a 5 V input voltage and read the output on its differential

terminals. The gauges had an accuracy of ±2%, a range of ±4000 με, and a minimum limit of 30 με. The strain gauges experienced no mortality during the live load tests. Although the gauges were tough, additional cover plates were used to protect them from direct wheel loads. The gauges did not need direct wiring to a data-acquisition system, as they were equipped with a transmitter to connect them to a laptop via Wi-Fi.

4.3 RESULTS OF FIRST AND THIRD LOAD TESTINGS

4.3.1 General Behavior

The first round of live load tests on the two bridges was conducted in August and September 2018 for steel- and GFRP-reinforced bridges, respectively. Prior to a detailed analysis of the recorded data, it was critical to verify that the behavior of each bridge deck recorded during the tests was consistent with the direction and relative magnitude of the expected response. With the availability of the strain time history from the live load tests, the bridge deck response was examined. The response patterns and magnitudes were compared with the available results in the literature. All the gauges were evaluated under the governing load cases, and some of them are presented as examples.

As the third load test details were comparable to those completed in the first year, this section also contains the data related to the third load test conducted in August 2022. Due to a change in the instrumentation plan of the GFRP-reinforced bridge deck (27W37) deck, the second load test data will be presented in Section 4.4. As such, the third set of live load tests on the two bridges was. The longitudinal strain time histories are shown in Figures 4.15 and 4.16 at strain gauge locations D14 and D15 for the first and third load tests, respectively.

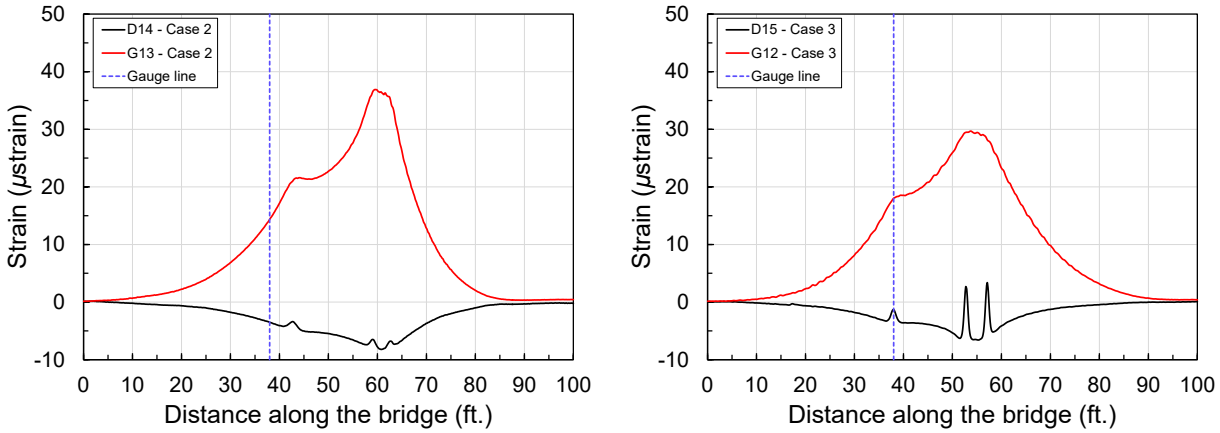

Figure 4.15 Bridge response for steel-reinforced bridge deck (27W36) during the first load test: (a) load case 2 and (b) load case 3

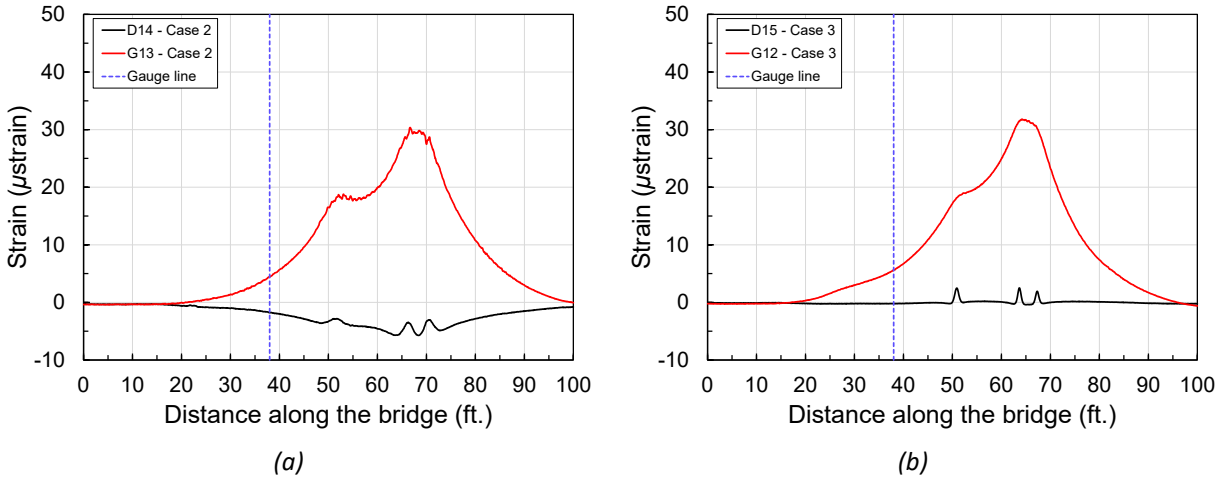

Figure 4.16 Bridge response for steel-reinforced bridge deck (27W36) during the third load test: (a) load case 2 and (b) load case 3

It should be noted that the gauges on the top of the bridge deck were in the transverse direction and the gauges attached underneath the deck were in the longitudinal direction. In the generated plots, the positions denoted along the horizontal axis refer to the position of the truck's front tire as it crossed the bridge. The distance between the peaks of the tandem axles and the peak of the front axle is equal to the center-to-center distance between the rear and front axles of the truck. The start and finish of the tests were indicated by a 0 ft and 100 ft distance along the X-axis. Comparing the response of the bridge deck to the results in the literature, the strain in the transverse direction of the bridge deck was not found to be significant.

Figures 4.17 and 4.18 illustrate the strain time history of girder 4 and the displacement response of the bridge deck at strain gauge location L4 for the first and third load tests, respectively. The relative displacement between the deck and girder at location L4 reveals the stiff nature of the bridge deck.

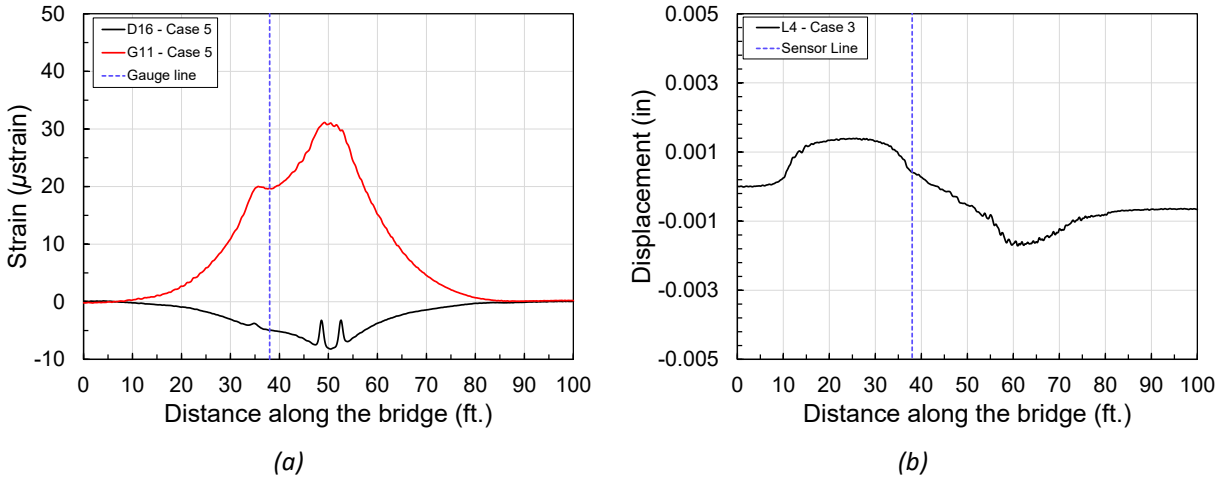

Figure 4.17 Bridge response for steel-reinforced bridge deck (27W36) measured during the first load test: (a) strain time history under load case 5 and (b) displacement time history under load case 3

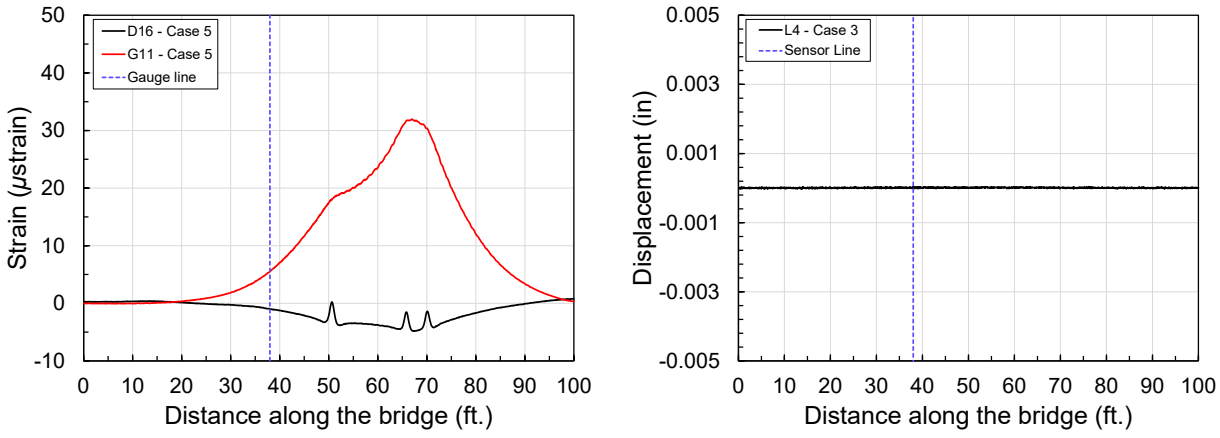

(a) *(b)*

Figure 4.18 Bridge response for steel-reinforced bridge deck (27W36) measured during the third load test: (a) strain time history under load case 5 and (b) displacement time history under load case 3

For the GFRP-reinforced bridge deck (27W37), the longitudinal strain time histories are shown in Figures 4.19 and 4.20 at strain gauge locations D14 and D15 for the first and third load tests, respectively. Comparing the response of the bridge deck to the results in the literature, the strain in the transverse direction of the bridge deck was not found to be significant.

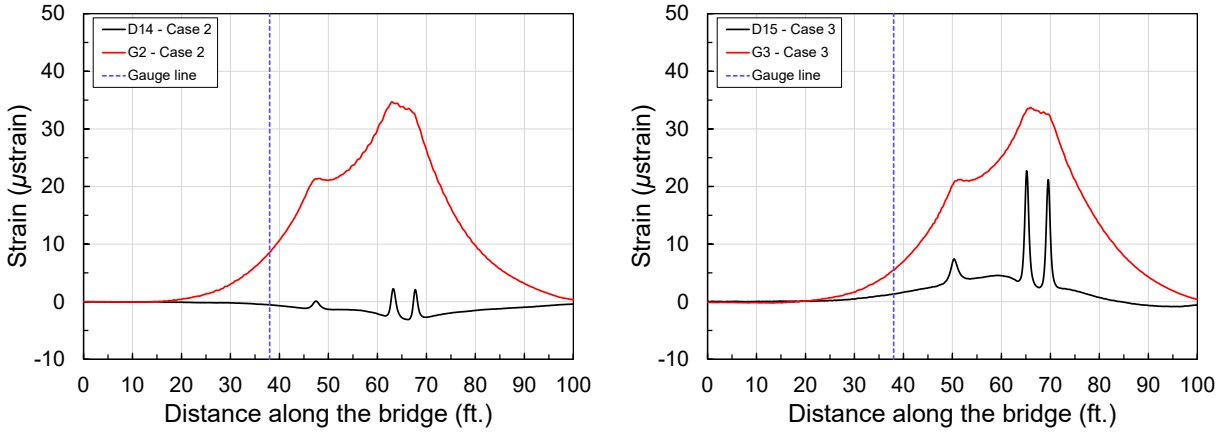

(a) *(b)*

Figure 4.19 Bridge response for GFRP-reinforced bridge deck (27W37) measured during the first load test: (a) load case 2 and (b) load case 3

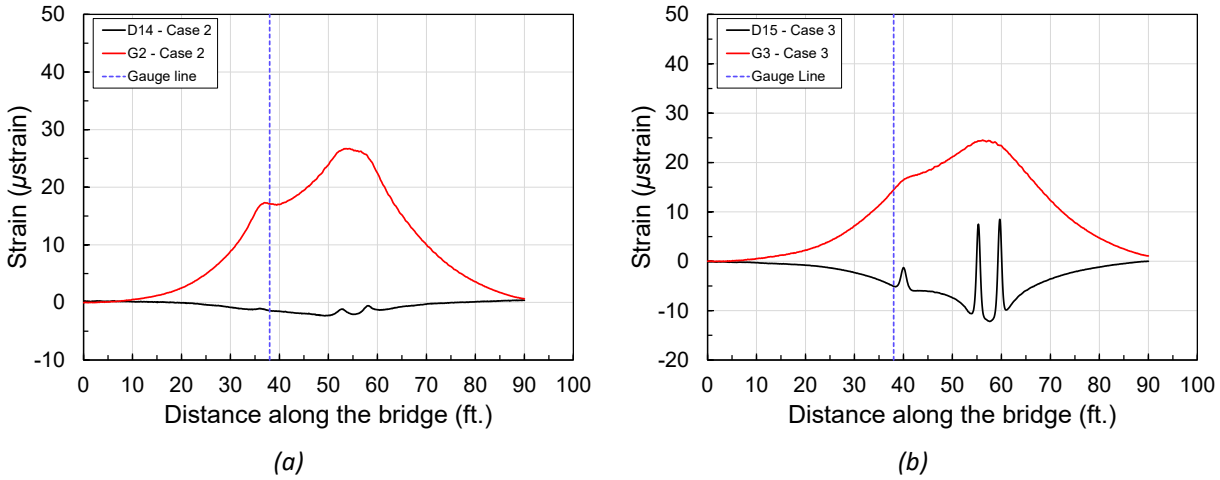

(a) *(b)*

Figure 4.20 Bridge response for GFRP-reinforced bridge deck (27W37) measured during the third load test: (a) load case 2 and (b) load case 3

Figures 4.21 and 4.22 illustrate the strain time history and displacement response of the bridge deck at the first and third load tests, respectively.

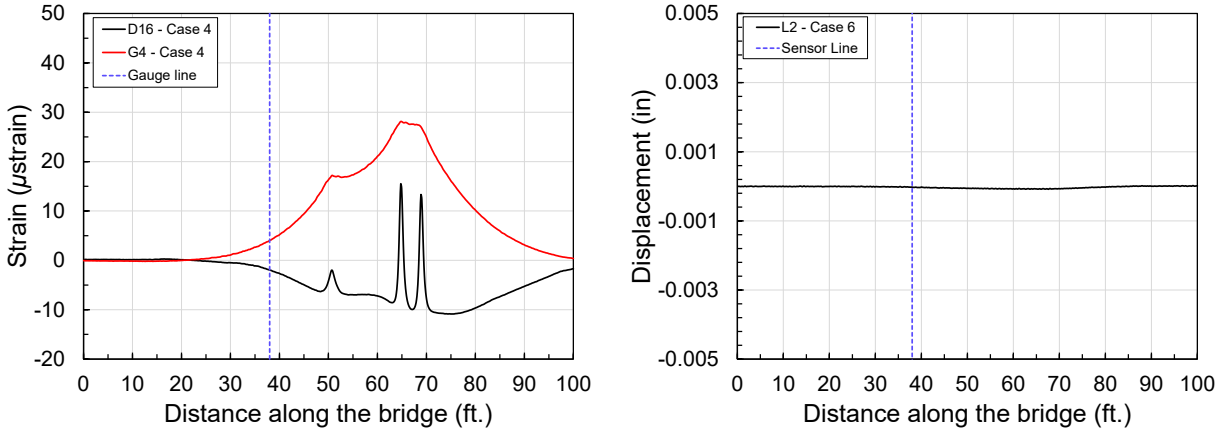

(a) *(b)*

Figure 4.21 Bridge response for GFRP-reinforced bridge deck (27W37) measured during the first load test: (a) strain time history under load 4 and (b) displacement time history load 6

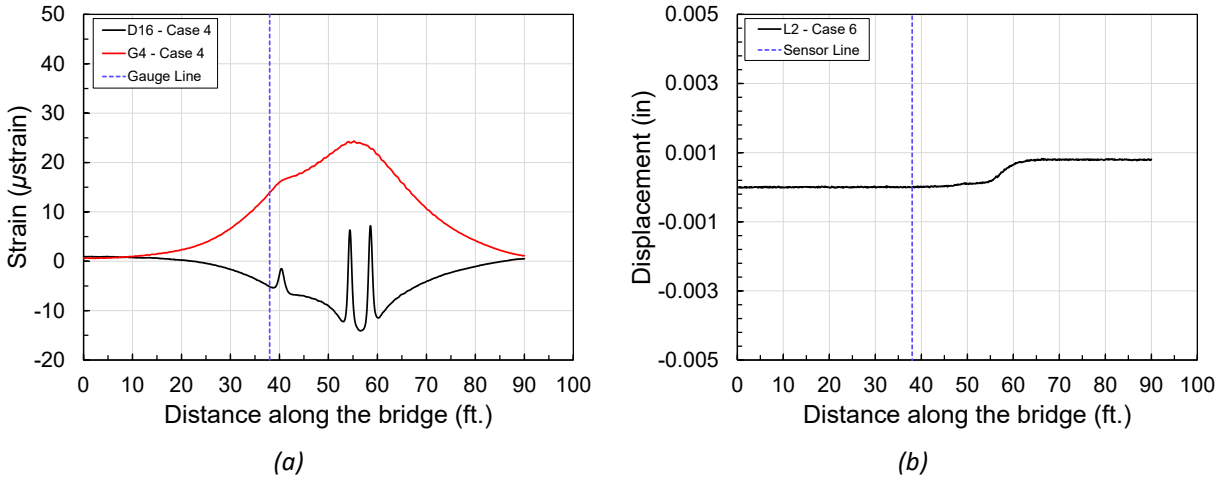

Figure 4.22 Bridge response for GFRP-reinforced bridge deck (27W37) measured during the third load test: (a) strain time history under load case 4 and (b) displacement time history under load case 6

Comparing the relative displacement between the deck and girder for the GFRP-reinforced bridge deck (27W37) and the steel-reinforced bridge deck (27W36), no excessive deflection was observed for either bridge.

The results of the third set of load tests were found to be aligned with the results of the first set of load tests. No unusual behavior/response was recorded for either bridge.

4.3.2 Neutral Axis Position

The live load test data were used to verify whether the deck and girders maintained a composite action. For this purpose, the neutral axis position was determined for various load cases. Prior to finding the neutral axis position, it was informative to review what the gauges indicated with respect to the general behavior of the deck. As expected, the truck position induced a positive moment on the deck at the mid-span (top compression, bottom tension). Thus, the neutral axis was calculated by using the strain values at the top and bottom of the girder as well as underneath the deck. The neutral axis was determined when the vehicle was at the mid-span of the bridge deck.

Figures 4.23 and 4.24 show the neutral axis location for load case 1 at strain gauge locations D14 and D15.

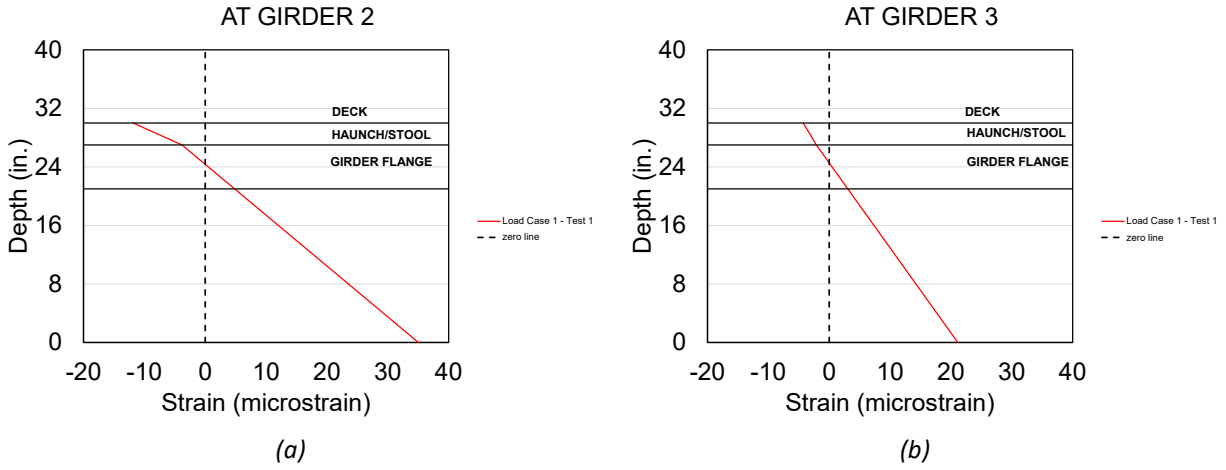

Figure 4.23 Neutral axis locations in steel-reinforced bridge deck (27W36) for the load case 1 of the first load test: (a) girder 2 and (b) girder 3

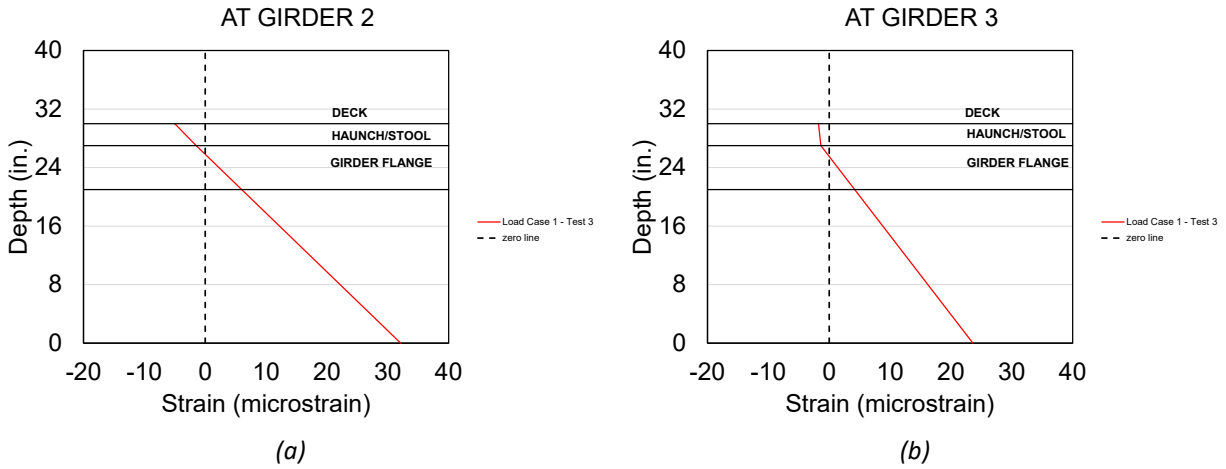

Figure 4.24 Neutral axis locations in steel-reinforced bridge deck (27W36) for the load case 1 of the third load test: (a) girder 2 and (b) girder 3

The linear variation of strain gauges D14, G6, and G13 and strain gauges D15, G5, and G12 at the D14 and D15 gauge locations confirmed the composite action of the bridge deck with the girders. The neutral axes for these cases were found to be in the girder flange, which was reasonable for a truck load. Similar results were obtained for the other load cases. Based on a comparison of results obtained under various load cases, the deck response was found to maintain its expected performance.

The process was repeated for the GFRP-reinforced bridge deck (27W37) to calculate the neutral axis. Figures 4.25 and 4.26 clearly illustrate that the neutral axis lies in the girder flange for load case 1 at strain gauge locations D14 and D15. The linear relation also reveals the composite action of the deck and girders.

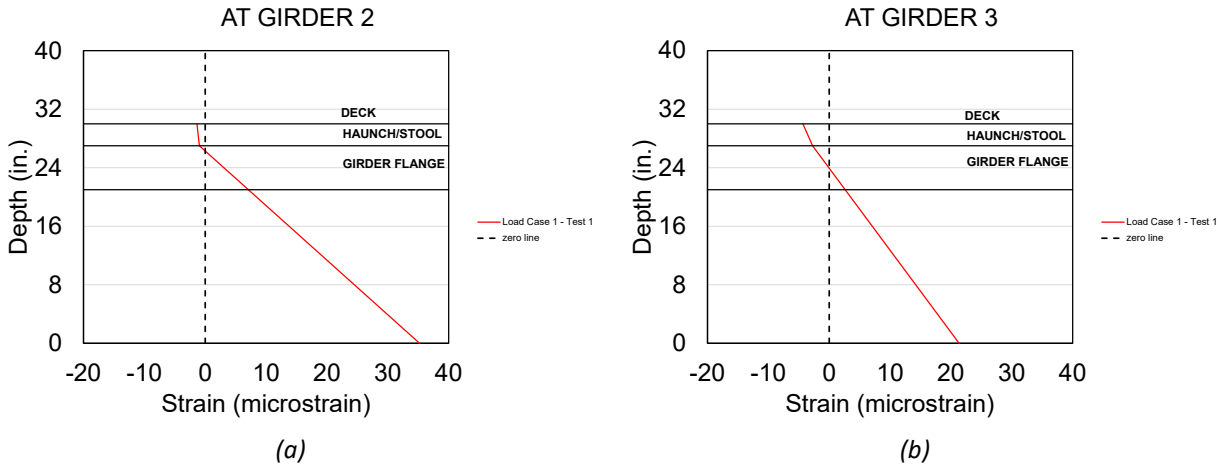

Figure 4.25 Neutral axis locations in GFRP-reinforced bridge deck (27W37) for the load case 1 of the first load test: (a) girder 2 and (b) girder 3

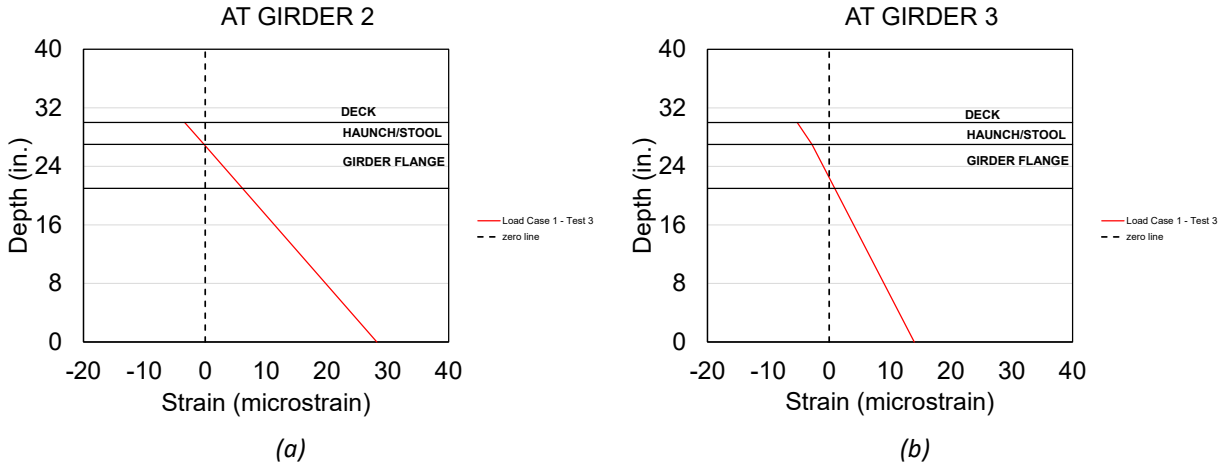

Figure 4.26 Neutral axis locations in GFRP-reinforced bridge deck (27W37) for the load case 1 of the third load test: (a) girder 2 and (b) girder 3

4.4 RESULTS OF SECOND LIVE LOAD TESTING

4.4.1 General Behavior

The second set of live load tests on the two bridges was conducted in June 2021. As with the first-year load tests, the longitudinal strain time histories are plotted in Figures 4.27 and 4.28 at strain gauge locations D14, D15, and D16 for load cases 2, 3, and 5, respectively.

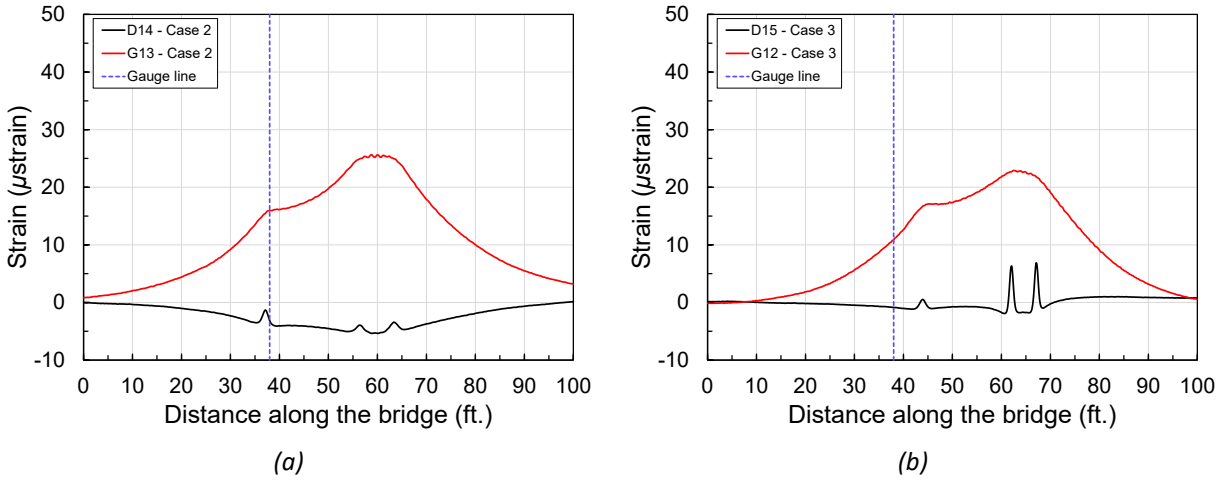

Figure 4.27 Bridge response for steel-reinforced bridge deck (27W36) measured during the second load test: (a) load case 2 and (b) load case 3

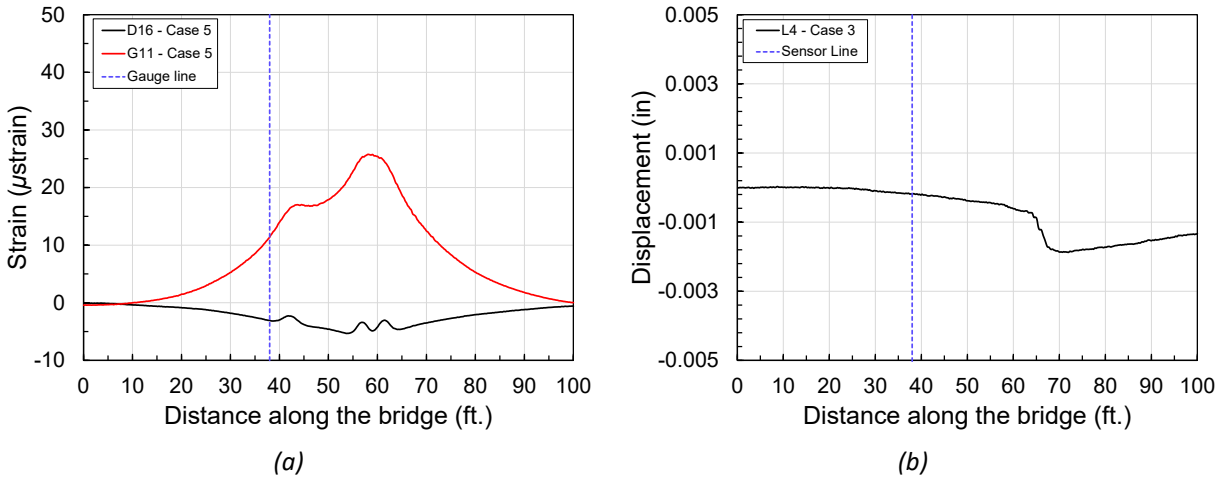

Figure 4.28 Bridge response for steel-reinforced bridge deck (27W36) measured during the second load test: (a) strain time history under load case 5 and (b) displacement time history under load case 3

In the generated plots, the positions denoted along the horizontal axis refer to the position of the truck's front tire as it crossed the bridge. Comparing the response of the bridge deck with the response recorded during the first-year load tests, the strains in the transverse direction of the bridge deck were observed to be similar. The live load test conducted on the GFRP-reinforced bridge deck (27W37) had some changes. Due to high water levels in the river, it was not possible to reach under the bridge. Consequently, the instrumentation plan was adjusted. The instrumentation at the mid-span was moved to a location 7 ft from the north abutment. As a result, the strains recorded were considerably lower than the strains recorded during the first-year load tests.

Figures 4.29 and 4.30 shows the strain and displacement response for various load cases.

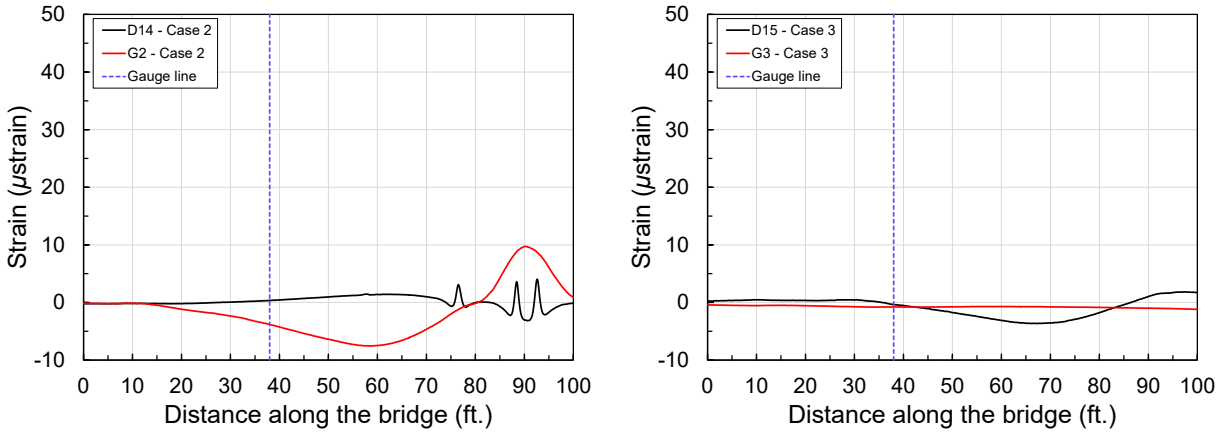

Figure 4.29 Bridge response for GFRP-reinforced bridge deck (27W37) measured during the second load test: (a) load case 2 and (b) load case 3

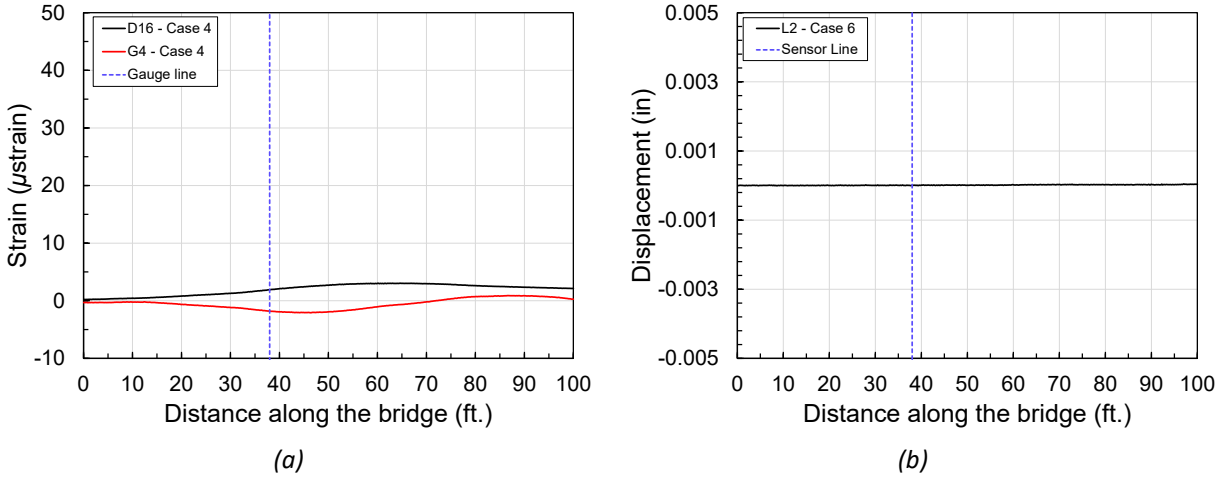

Figure 4.30 Bridge response for GFRP-reinforced bridge deck (27W37) measured during the second load test: (a) strain time history under load case 4 and (b) displacement time history under load case 6

As expected, the strain values were very low compared to the previous year. Also, the measured relative displacements were very small, showing the stiffness of the deck.

4.4.2 Neutral Axis Position

Similar to the first live load test, test data from the second load test were used to find the neutral axis position for various load cases. For this purpose, the neutral axis was calculated by using the strain values at the top and bottom of the girder as well as underneath the deck. Figure 4.31 shows the neutral axis location for load case 1 at strain gauge locations D14 and D15 at the time of peak strain response.

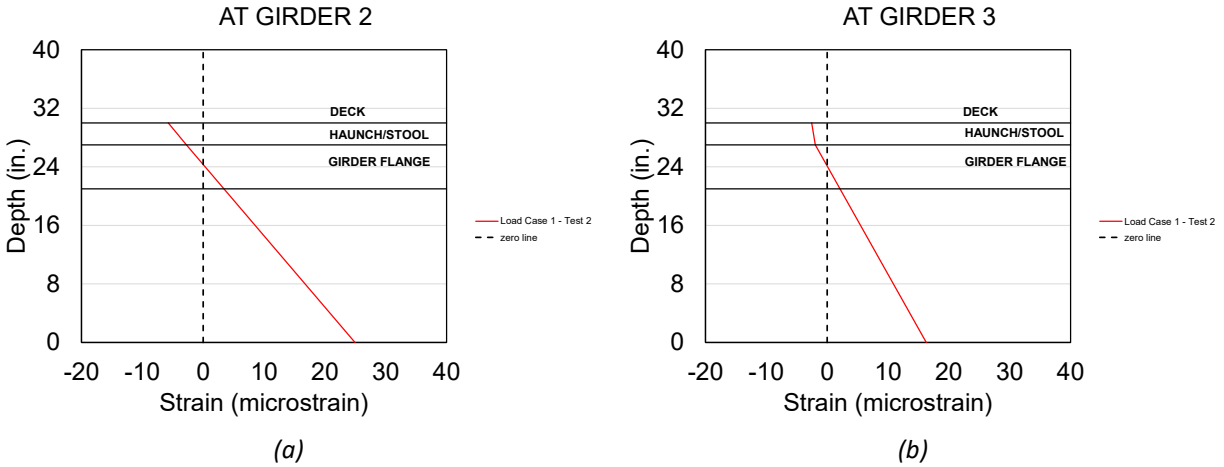

Figure 4.31 Neutral axis locations in steel-reinforced bridge deck (27W36) for load case 1: (a) girder 2 and (b) girder 3

The linear variation of strain gauges D14, G6, and G13 at the D14 gauge location confirmed the composite action of the bridge deck with the girders. The neutral axis in this case was found to be in the girder flange, which was reasonable for a truck load.

The process was repeated for the GFRP-reinforced bridge deck (27W37) to calculate the neutral axis. Figure 4.32 illustrates that the neutral axis lies in the girder web for load case 1 at strain gauge location D14.

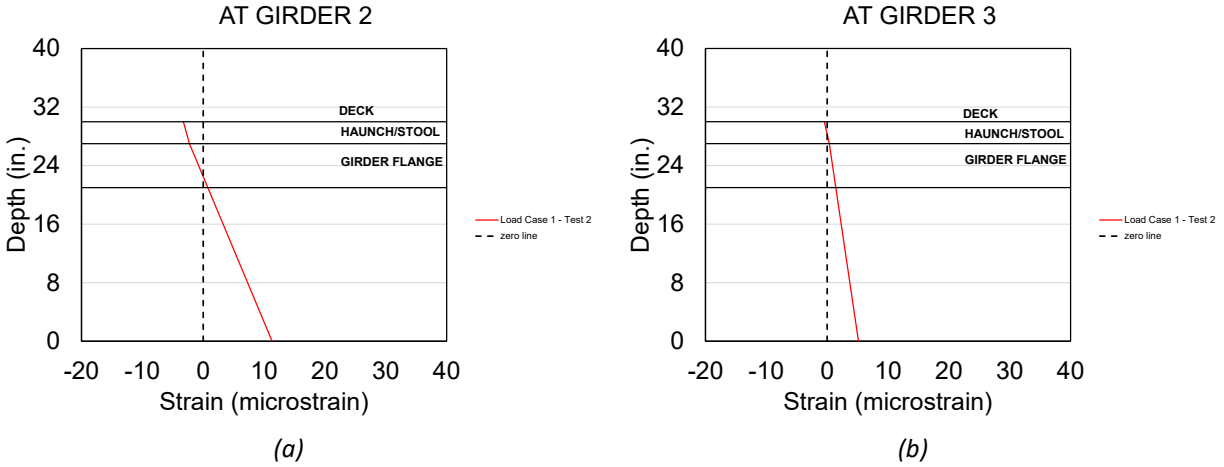

Figure 4.32 Neutral axis locations in GFRP-reinforced bridge deck (27W37) for load case 1: (a) girder 2 and (b) girder 3

At strain gauge location D15, the neutral axis lies in the deck. This behavior was different from what was obtained during the first load test. This was attributed to the location of the strain gauge during the second load test compared to its location during the first load test.

4.5 COMPARISONS OF THE THREE TESTS

Figures 4.33 and 4.34 show two girders under two similar load cases for the bridges with steel- and GFRP-reinforced decks.

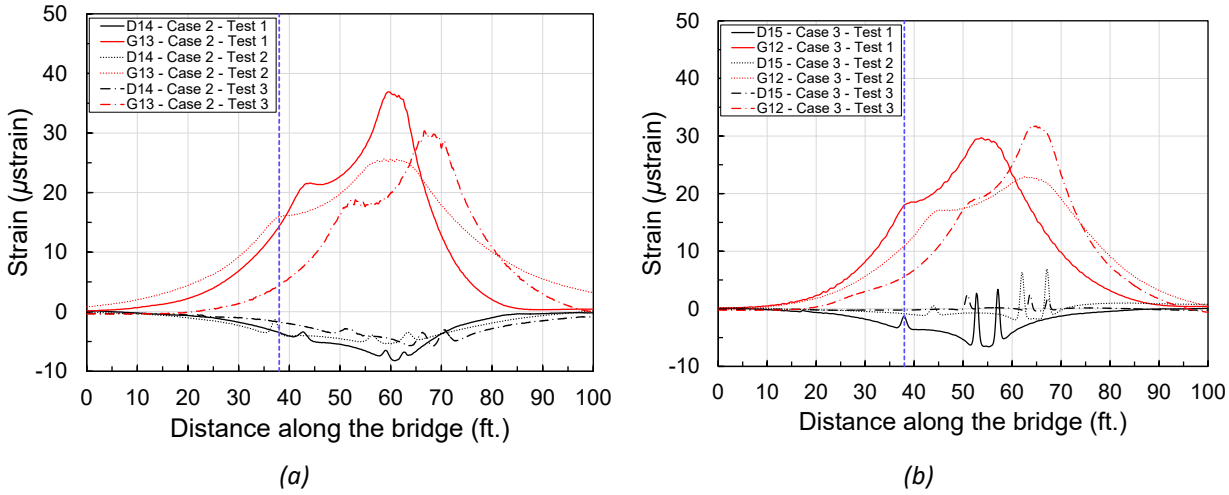

Figure 4.33 Bridge response for steel-reinforced bridge deck (27W36) over three tests: (a) load case 2 and (b) load case 3

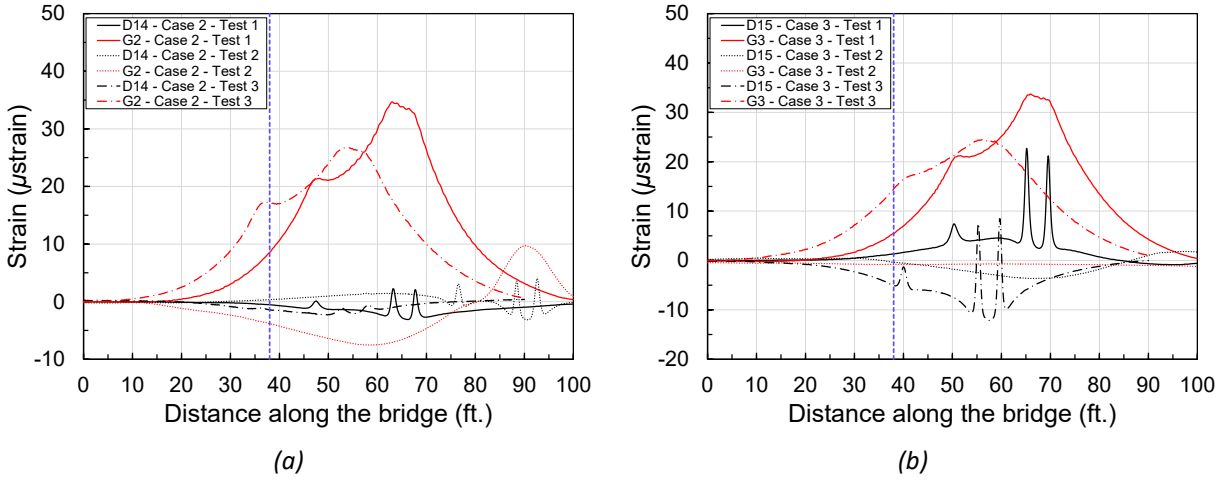

Figure 4.34 Bridge response for GFRP-reinforced bridge deck (27W37) over three tests: (a) load case 2 and (b) load case 3

Comparing all of the strain values versus the locations of the front wheels under the governing load cases over three tests shows consistently low values in both bridge decks. No unusual behavior was seen during the three tests in the GFRP-reinforced bridge deck, proving that using GFRP bars as an alternative to conventional bridge deck reinforcement does not cause the deck's behavior to differ significantly under live vehicle loads.

Moreover, Figure 4.35 shows the deck relative displacement over the three tests.

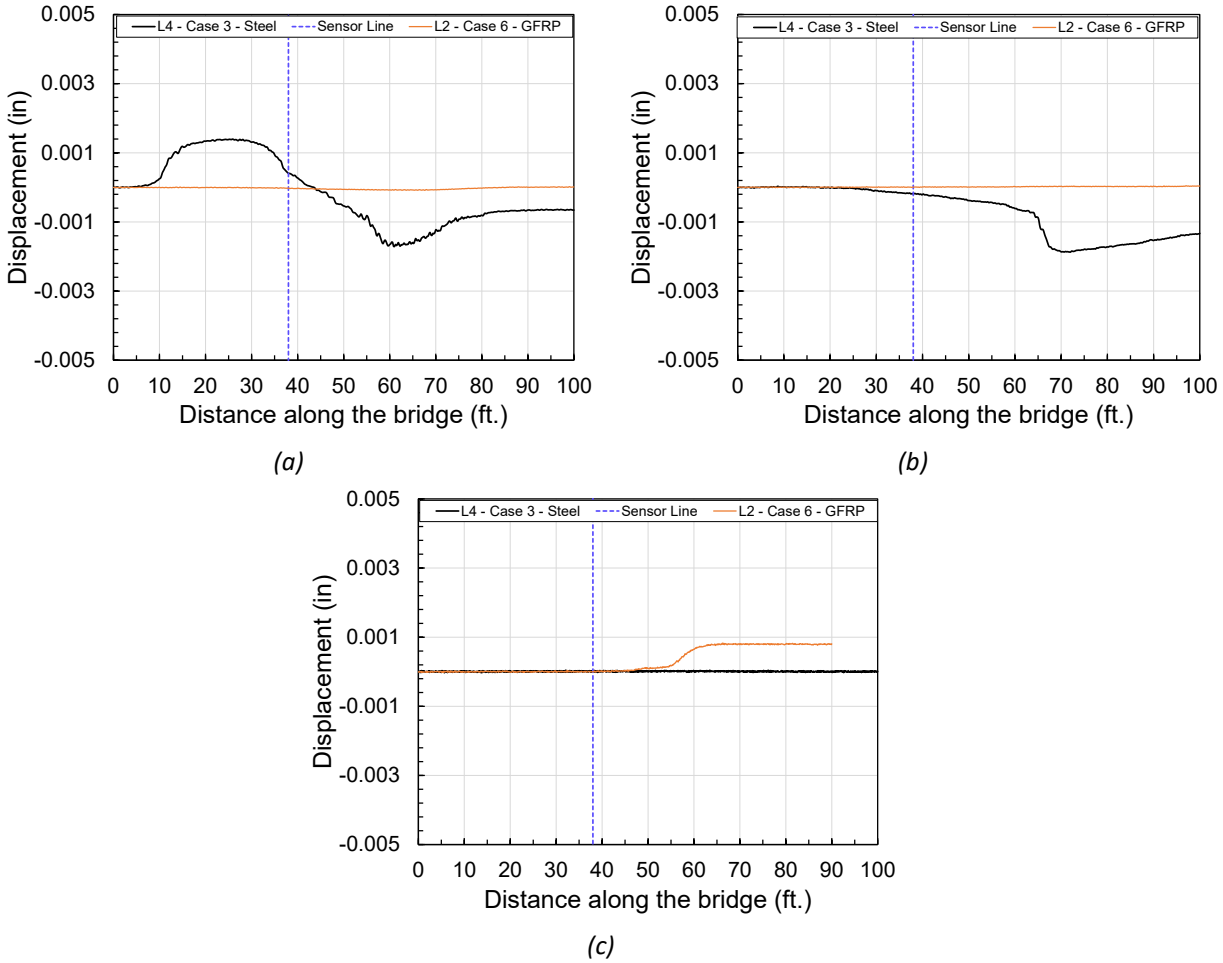

Figure 4.35 Deck relative displacement at sensors L4 of 27W36 and L2 of 27W37 bridge decks: (a) first live load test, (b) second live load test and (c) third live load test

The relative displacements of the deck with respect to the beams were found to be very small and even negligible in many cases. Table 4.1 provides the relative displacements recorded under the most demanding load cases.

Table 4.1 Relative displacement of the deck with respect to the girders

	Test 1		Test 2		Test 3	
Sensor	**Steel Deck**	**GFRP Deck**	**Steel Deck**	**GFRP Deck**	**Steel Deck**	**GFRP Deck**
L1	0.0011 in	0.0009 in	negligible	negligible	negligible	negligible
L2	0.0009 in	negligible	0.0003 in	negligible	negligible	0.0008 in
L3	0.0007 in	negligible	0.0032 in	negligible	negligible	negligible
L4	0.0017 in	0.0014 in	0.0019 in	negligible	negligible	0.0002 in
L5	0.0009 in	0.0013 in	negligible	0.0003 in	0.0002 in	negligible
L6	negligible	0.0006 in	0.0003 in	0.0013 in	0.0001 in	0.0007 in

Figures 4.36 and 4.37 show the neutral axis location at girders 2 and 3 for the steel- and GFRP-reinforced bridge decks under two different load cases, respectively.

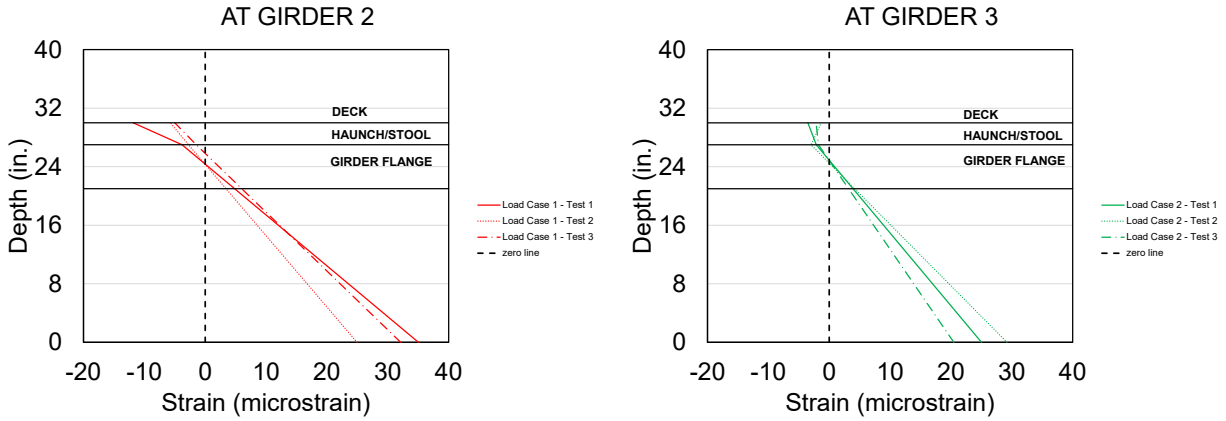

Figure 4.36 Neutral axis locations in steel-reinforced bridge deck (27W36) over three load tests for (a) girder 2 load case 1 and (b) girder 3 load case 2

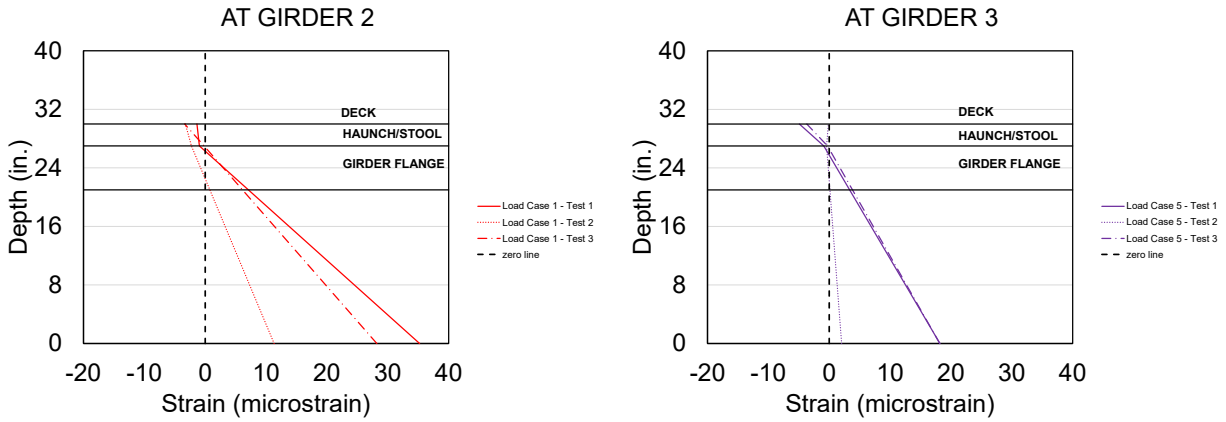

Figure 4.37 Neutral axis locations in GFRP-reinforced bridge deck (27W37) over three load tests for (a) girder 2 load case 1 and (b) girder 3 load case 5

Comparing all of the neutral axis locations at different girders under various load cases shows the composite action of the steel- and GFRP-reinforced bridge decks and indicates no significant change over three years.

4.6 GIRDER DISTRIBUTION FACTORS

Bridge girders are designed according to the AASHTO LRFD Bridge Design Specifications, which require calculation of the GDF. Given the relatively low stiffness of GFRP rebar, GDFs were determined for the two bridges under consideration in this research to understand what portion of the live load is

distributed to individual girders due to single- or multi-lane traffic. For this purpose, both the lever rule and special analyses were used.

4.6.1 Interior Girders

Per AASHTO Table 4.6.2.2.2b-1 (interior girders), the GDF for the moment when one design lane is loaded can be estimated as follows:

$$GDF = 0.06 + \left(\frac{s}{14}\right)^2 \left(\frac{s}{L}\right)^{0.3} \left(\frac{K_g}{12Lt_s^3}\right)^{0.1} \quad (4.1)$$

Per AASHTO Table 4.6.2.2.2b-1 (interior girders), the GDF for the moment when two or more design lanes are loaded can be found from the following:

$$GDF = 0.075 + \left(\frac{s}{9.5}\right)^{0.6} \left(\frac{s}{L}\right)^{0.2} \left(\frac{K_g}{12Lt_s^3}\right)^{0.1} \quad (4.2)$$

where *s* = spacing between girders, *L* = span length, and t_s= thickness of the slab. In Equations 1 and 2, K_g is calculated using the section properties as follows:

$$K_g = n\left(I_{beam} + Ae_g^2\right) \quad (4.3)$$

where I_{beam} = moment of inertia of the girder, *n* = number of girders, and *A* = area of the girder.

4.6.2 Exterior Girders

The GDF for exterior girders is calculated as follows using the lever rule, special analysis, and a simplified equation for single-lane and multi-lane effects:

Lever rule:

$$g_{ext} = \frac{\left[\frac{(6+X1)+(X1)}{s}\right]}{2}(MPF) \quad (4.4)$$

Special analysis:

$$g_{ext} = \left[\frac{N_L}{N_b} + \frac{X_{ext}\sum e}{\sum X^2}\right](MPF) \quad (4.5)$$

Simplified equation:

$$g_{ext} = e g_{int} \quad (4.6)$$

where *MPF* = multiple presence factor, N_L = number of loaded lanes, N_b = number of girders, X_{ext} = distance between the exterior girder and the center of the bridge, *e* = distance between the centroid of the vehicle and the center of the bridge, and *X* = distance between the girder and the center of the bridge.

4.6.3 Calculation of Girder Distribution Factors from Field Tests

An accurate determination of load transfer from the deck to the supporting girders is a critical issue in the design process. Thus, the live load test data were used to calculate the actual GDFs using the recorded strains. The strain data from the gauges placed on the bottom flange of the girder were used to calculate the GDFs using the following equation:

$$\text{GDF}_i = \frac{M_i}{\sum_{j\neq 1}^{k} M_j} = \frac{\varepsilon_i w_i}{\sum_{j\neq 1}^{k} \varepsilon_j w_j} \tag{4.7}$$

where M_i = bending moment at the i^{th} girder, ε_i = maximum bottom flange strain at the i^{th} girder, and w_i = ratio of the section modulus of the i^{th} girder to that of a typical interior girder. As all the girders are similar, the factor w_i is taken as 1.

The GDFs calculated were then compared with the GDFs given in AASHTO Table 4.6.2.2.2b-1 and Table 4.6.2.2.2d-1. The GDFs were calculated for every load case. Since two trials were performed for each load case, the average values were used to calculate the GDFs for the worst case.

Figure 4.38 shows the strain values measured at the bottom flange of the girders of the steel-reinforced bridge deck (27W36) under load cases 1 and 2.

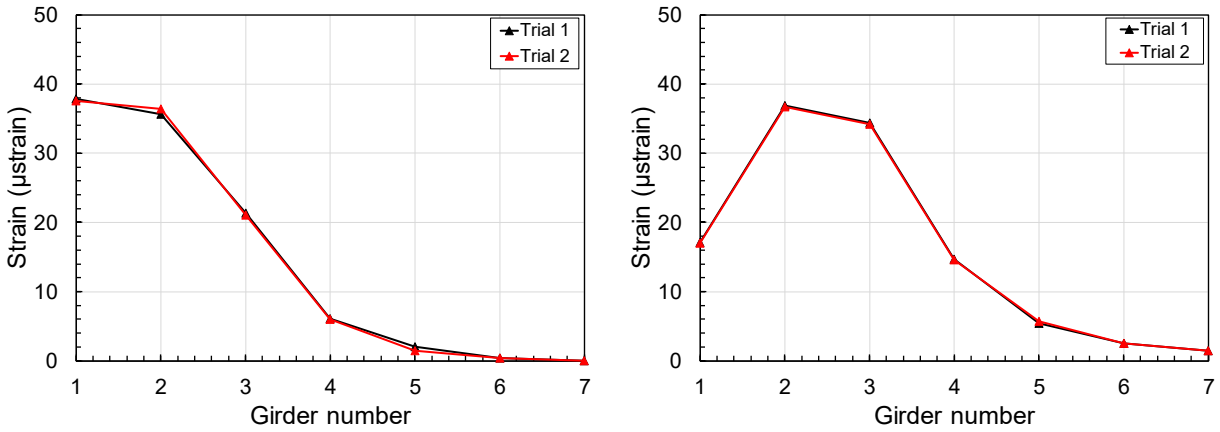

Figure 4.38 Strain measured at the bottom flange of the girders of steel-reinforced bridge deck (27W36) under (a) load case 1 and (b) load case 2

The data was obtained during the first load test. The girders were numbered from 1 to 7. The maximum strain was found to occur in the girders that were directly under the load path of the truck.

The strain data from every load case was then used to calculate the GDFs (Figure 4.39). It was observed that a significant portion of the total load was transferred to the girders underneath the truck path and adjacent girders.

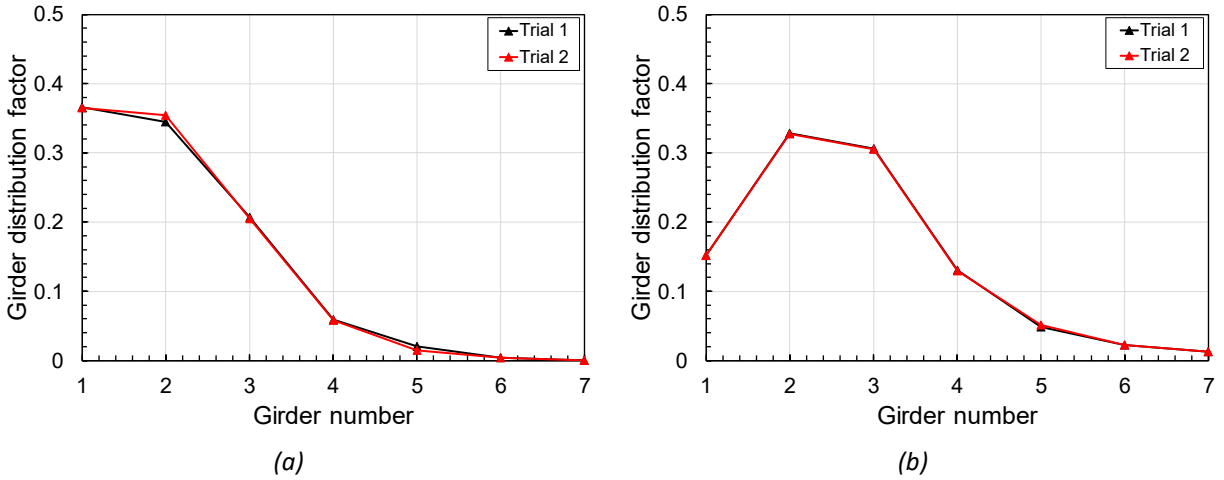

Figure 4.39 Girder distribution factors calculated for steel-reinforced bridge deck (27W36) under (a) load case 1 and (b) load case 2

Similarly, the maximum strains and GDFs were calculated for the GFRP-reinforced bridge deck (27W37) under load cases 1 and 2 (Figures 4.40 and 4.41). From the strain and GDF values, no significant difference was observed between the two bridges.

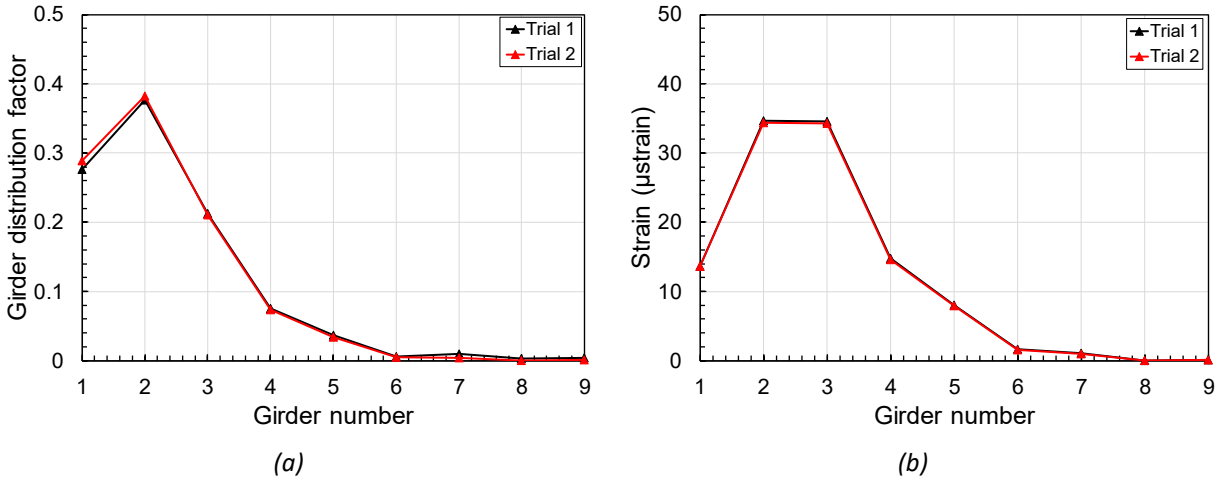

Figure 4.40 Strain measured at the bottom flange of the girders of GFRP-reinforced bridge deck (27W37) under (a) load case 1 and (b) load case 2

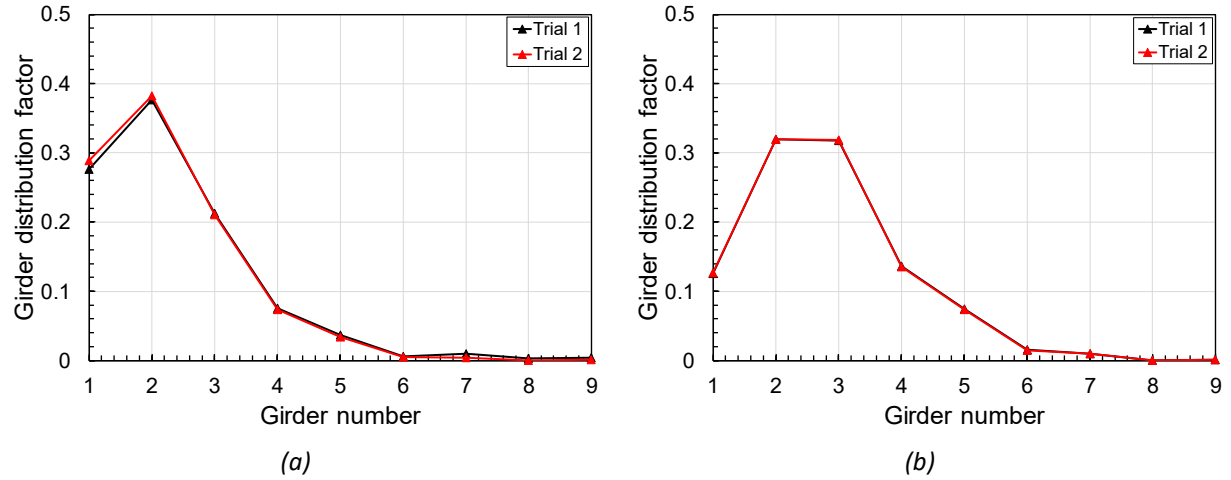

Figure 4.41 Girder distribution factors calculated for GFRP-reinforced bridge deck (27W37) under (a) load case 1 and (b) load case 2

For the steel-reinforced bridge deck (27W36), the maximum values from the seven load cases were used to create Figure 4.42(a).

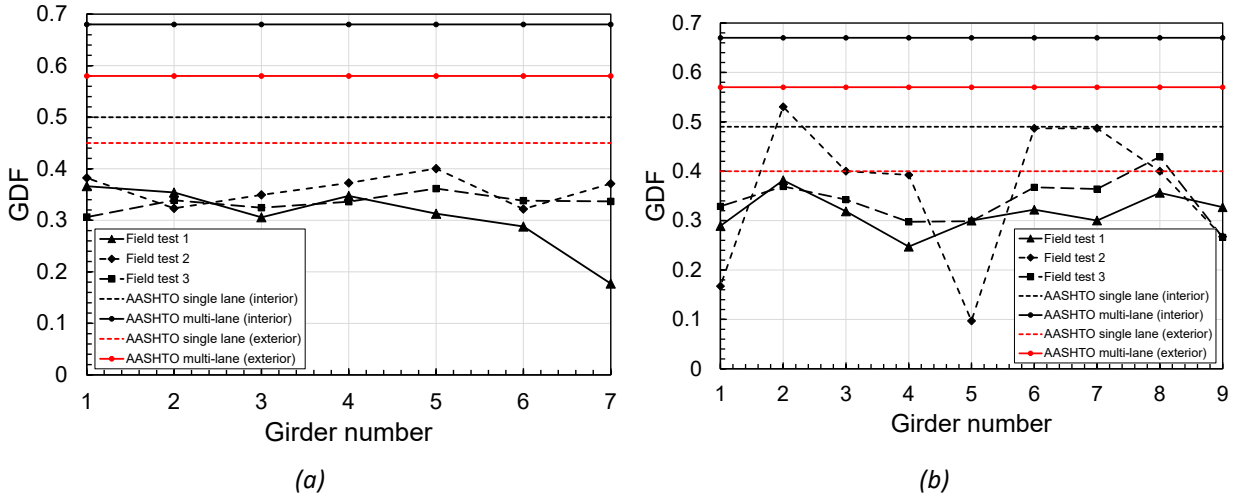

Figure 4.42 Comparison of calculated girder distribution factors with AASHTO specifications: (a) steel-reinforced bridge deck (27W36) and (b) GFRP-reinforced bridge deck (27W37)

This figure includes a comparison of the GDFs calculated from the three live load tests with those obtained from the AASHTO specifications. During the first load test for the steel-reinforced bridge deck (27W36), a lower GDF value was observed at girder 7 because the load path placed directly over girder 7 was not conducted. This load path was added during the second load test.

The strain gauge at girder 6 malfunctioned in the second load test. Therefore, the GDF for girder 6 could not be calculated. This also affected the GDF values for girders 4 through 6. Considering the fact that the total sum of strains should be approximately equal for all load cases, a correction was applied to the strain data at girder 6. The average sum of strains measured during load cases 5, 6, and 7 were subtracted from the average sum of strains measured during load cases 1 and 2. After applying the

correction, the GDF values in the second load test were found to be in good agreement with the values measured during the first load test.

In the third load test, the measured GDF values were also found to match closely with the values obtained from the first and second load tests. From the repeatability of the GDF values, it can be concluded that the bridge deck and girder system showed the expected load transfer mechanism.

In a similar way, the maximum values from the nine load cases were used to create Figure 4.42(b). Similar to the steel-reinforced bridge deck (27W36), some differences in the GDFs were observed between the first two load tests. In this case, it is not clear whether the differences were caused by changes in the bridge deck or changes in the strain gauge locations. In the third load test, the measured GDF values were found to match closely with the values obtained from the first load test. Therefore, the variation observed in the second load test was attributed to changes in the strain gauge locations.

Comparing Figures 4.42(a) and 4.42(b), the GDFs from two bridges were found to be comparable and in agreement with the AASHTO specifications.

CHAPTER 5: BRIDGE DECK INSPECTION

One of the main objectives of the inspection efforts was to document the number of cracks and types of cracks. Regular visits to the bridge site were planned for every six months throughout the entire duration of the project to inspect the condition state of the bridge decks and to retrieve the recorded long-term monitoring data for off-site processing. The periodic visual surveys of the top and underside of the bridges helped in identifying the development of cracks and irregularities.

5.1 FIRST SERIES OF INSPECTIONS

Extensive surveys during the site visit in May 2019 revealed top surface and full-depth cracks in both bridge decks. Top surface cracks were evident in the top surfaces of the decks (Figure 5.1).

(a) *(b)*

Figure 5.1 Top surface cracks in the bridge decks: (a) steel-reinforced bridge deck (27W36) and (b) GFRP-reinforced bridge deck (27W37)

Most of the surface cracks were found to propagate in the transverse direction. The distribution of cracks in the two bridges, however, was not identical. While the cracks in the steel-reinforced bridge deck (27W36) were more toward the bridge abutments at the beginning, the cracks in the GFRP-reinforced bridge deck (27W37) were generally away from the bridge abutments. This could be due to a variety of geometric and support conditions, as the crack patterns started to become similar over time.

In addition, full-depth cracks were also detected that extended from both the top and bottom surfaces. These cracks were marked with a white precipitate underneath the bridge decks (Figure 5.2).

(a) *(b)*

Figure 5.2 Full-depth cracks in the bridge decks: (a) steel-reinforced bridge deck (27W36) and (b) GFRP-reinforced bridge deck (27W37)

On comparing the crack formation in the two bridge decks, the steel-reinforced bridge deck (27W36) showed a significantly higher number of cracks compared to the GFRP-reinforced bridge deck (27W37).

5.2 SECOND SERIES OF INSPECTIONS

The second detailed inspection was conducted in November 2021 (after a delay due to Covid). Figure 5.3 shows close-up views of cracks in the two bridge decks along with a ruler to indicate the sizes of the cracks.

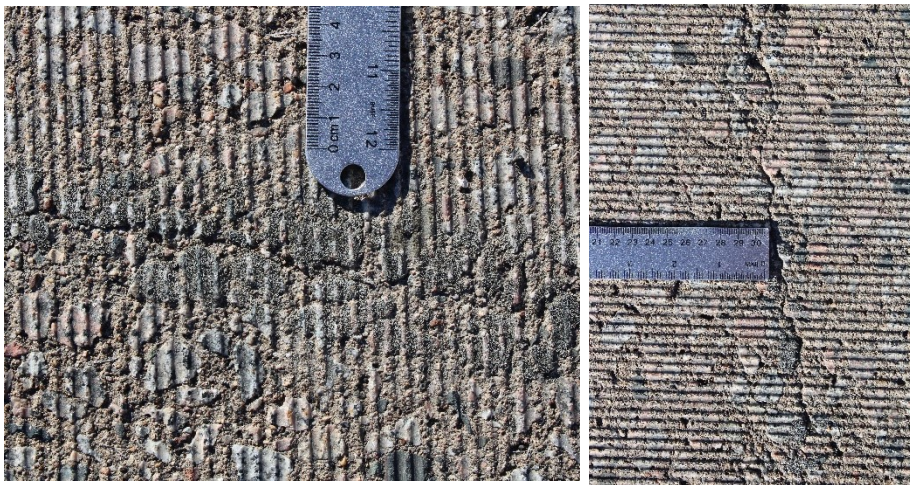

(a) *(b)*

Figure 5.3 Close-up view of cracks in the bridge decks: (a) steel-reinforced bridge deck (27W36) and (b) GFRP-reinforced bridge deck (27W37)

Figure 5.4 shows the cracks underneath the GFRP-reinforced bridge deck (27W37).

The cracks were observed to extend through the surface, as indicated by the amount of efflorescence. The cracks progressed across the width of the deck near the mid-span, whereas the cracks progressed diagonally near the abutment.

(a) *(b)*

Figure 5.4 Full-depth cracks in GFRP-reinforced bridge deck (27W37)

Similar crack patterns were observed in the steel-reinforced bridge deck (27W36). Figure 5.5 shows two cracks in this bridge deck, one near the abutment and one at the mid-span.

(a) *(b)*

Figure 5.5 Full-depth cracks in steel-reinforced bridge deck (27W36)

5.3 THIRD SERIES OF INSPECTIONS

The third series of inspections were conducted on August 24 and 31, 2022. The inspection team carefully noted the lengths of the cracks as well as the number of cracks for both bridges. The cracks on the top surface of the steel-reinforced bridge deck (27W36) were found to be mainly in the transverse direction. The cracks were concentrated near the bridge abutments, which might show a fixity effect over the ends of the bridge. The cracks on the top surface of the GFRP-reinforced bridge deck (27W37) also indicate a crack concentration close to the abutments, especially near the north support of the bridge. Some inclined cracks are also evident near the corners of the bridge.

Horizontal cracking on the bottom surface of the bridge decks was also investigated during the third series of inspection. Through cracks, running the width between girders, were detected near the abutments of the steel-reinforced bridge deck (27W36) (Figure 5.6).

Figure 5.6 Cracks on the bottom surface of steel-reinforced bridge deck (27W36)

Figure 5.7 shows the cracks on the bottom surface of the GFRP-reinforced bridge deck (27W37).

Figure 5.7 Cracks on the bottom surface of GFRP-reinforced bridge deck (27W37)

As the figure shows, diagonal through cracks close to the abutment, horizontal through cracks at the quarter of the bridge length, and hairline cracks were observed on the bottom surface of this bridge deck.

Overall, the limited movement of the bridge deck due to the fixity effect of the abutments might have affected the formation of the transverse cracks close to the abutments in both bridges. The completed rounds of inspection showed that the crack patterns generally follow a similar trend. In particular, the formation and propagation of cracks were found to have slowed down during the most recent inspections. Thus, assuming no abrupt changes in environmental and mechanical stressors, no significant structural deterioration is anticipated in the near future for the two bridges investigated through this project.

CHAPTER 6: LABORATORY TESTS ON GFRP REBAR

6.1 INTRODUCTION

To better understand the mechanical properties and strength of the GFRP rebar used in the GFRP-reinforced bridge deck (27W37), a limited set of laboratory material characterization tests was conducted. A total of four samples of the GFRP rebar used in the TH 169 bridge construction project were tested in this task. The specimens were loaded in tension until failure while force, displacement, and strain were measured. From the data recorded, stress-strain curves were developed, and the tensile properties of the specimens were compared with reference values obtained through a review of previous GFRP tensile tests.

The tensile properties determined for the tested GFRP rebar were consistent with the values found in literature. As expected, all specimens exhibited brittle behavior until failure, as indicated by the stress-strain curves. Testing procedures generally followed ASTM D7205 (2016), the standard test method for determining the tensile properties of FRP bars. Any significant deviations that were noted are described in the following sections.

6.2 SPECIMEN PREPARATION AND TESTING

Table 6.1 summarizes the deviations in the dimensions of the anchors used during ASTM D7205 testing.

Table 6.1 Anchor dimensions

Approach	Length (in.)	Outside Diameter (in.)	Inside Diameter (in.)	Wall Thickness (in.)
Experimental Method	6	1.063	0.813	0.125
ASTM D7205*	15	1.63	1.25	0.19

*Values are based on a specimen dimeter of 5/8 in.

The GFRP rebar tested had a nominal diameter of 0.625 in. and an effective diameter of 0.67 in. For tensile testing and specimen preparation, the procedure outlined in ASTM D7205, along with the deviations noted below, was followed. The rebar samples provided by MnDOT were cut into 28 in. pieces with the goal of verifying 28 in. as a sufficient testing length.

For tensile testing of GFRP rebar, anchorage and anchor alignment are important because they can significantly affect the failure modes of GFRP specimens. For this experiment, an anchorage system consisting of steel pipe with an AC100+Gold adhesive anchoring system was used to apply confinement pressure on the rebar. The steel pipe was 6 in. long with an outside diameter of 1.0625 in. and a wall thickness of 0.125 in. For each specimen, two steel pipes were used at each end of the GFRP rebar. The steel pipes were threaded on the inside for a length of 3 in. at each end of the anchor. Steel pipe-shaped anchors were bonded to each end of the 28 in. specimens using AC100+Gold adhesive anchoring epoxy. Specimens were placed in a jig to ensure vertical alignment during application of the anchors. The epoxy

was given approximately 1 hour to cure (the manufacturer-suggested curing time). For all specimens, a 16 in. free (gauge) length was used with an effective bar diameter of 0.67 in. For this bar diameter, ASTM D7205 calls for a 27 in. gauge length.

Figure 6.1 shows the anchorage system developed for the installation of grips on the rebar.

(a) *(b)*

Figure 6.1 Anchorage system developed for grip installation on GFRP rebar

The anchorage system consisted of a rectangular frame made of wood. The top and bottom frame members included drilled holes with diameters equal to the outside diameter of the steel pipe. This was done to ensure proper alignment of the grips with the rebar.

A GFRP rebar specimen with attached grips can be seen in Figure 6.2(a). Specimens were placed in the SATEC Systems, Inc. Universal Testing Machine with the displacement rate set to 0.15 in./min (Figure 6.2(b)).

(a) GFRP specimen before testing

(b) Testing machine

Figure 6.2 GFRP rebar test pictures

Each 28 in. specimen was instrumented with one longitudinal 350 Ohm strain gauge (Figure 6.3(a)).

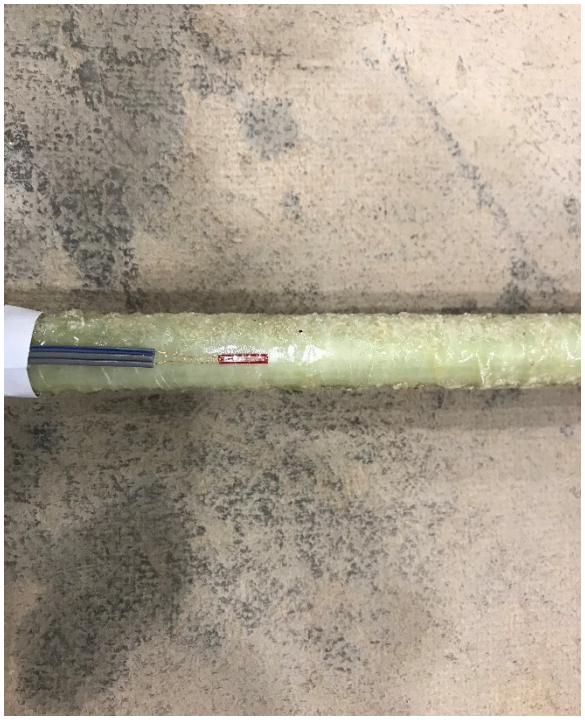

(a) Specimen instrumented with strain gauge

(b) Specimen mounted in testing machine

Figure 6.3 Tensile testing procedure for GFRP rebar

The displacement rate was calculated as per ASTM D7205, which calls for a strain rate of 0.01 min^{-1}, or a displacement rate of (0.01 min^{-1}) × (free length). Specimens were loaded in tension until failure, while force, strain, and displacement were measured.

6.3 RESULTS AND DISCUSSION

Figure 6.4 presents the stress-strain curves for the four GFRP test specimens. It can be clearly observed that the mechanical properties of the GFRP specimens were consistent across all tests.

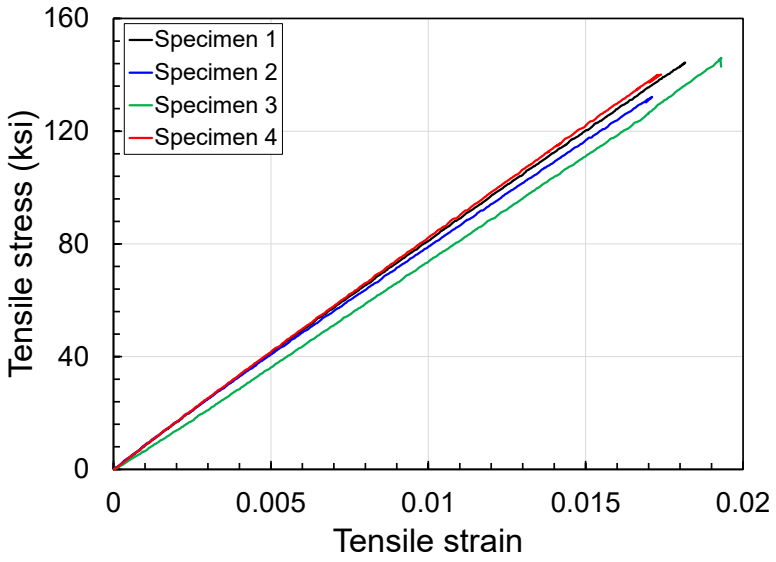

Figure 6.4 Experimental stress-strain curve for four GFRP specimens

The load measured using the Universal Testing Machine was converted to stress using the nominal cross-sectional area. To calculate nominal cross-sectional area, volume was measured directly by recording the volume of water displaced by a GFRP sample. ASTM D7205 calls for the indirect measurement of volume using mass divided by density. Nominal cross-sectional area was calculated as follows:

1. The GFRP specimens were cut into four samples of approximately 4 in. each.
2. The average length of each sample was calculated as the mean of three measured lengths, in accordance with ASTM D7205.
3. The volume of each sample was measured directly by water displacement.
4. The nominal cross-sectional area was calculated by (volume) / (length). A mean nominal area was calculated using all nine samples.

The consistency among the tests, along with the similarities between the experimental and reference tensile properties (Table 6.2), suggests that the testing procedure and resulting data are valid.

Table 6.2 Experimental test results

Specimen	Ultimate Load (k)	Ultimate Stress (ksi)	Ultimate Strain (μ)	Tensile Modulus (ksi)
1	44.8	144.4	18,156.5	8,045.0
2	40.9	132.2	17,111.9	7,833.9
3	45.3	145.9	19,314.6	7,428.7
4	43.4	140.1	17,393.5	8,171.1
Mean	**43.6**	**140.6**	**17,994.1**	**7,869.7**

In Figure 6.4, stress increases linearly until the point of maximum load and then undergoes a sudden failure. The failure is marked by several glass fibers snapping at once, causing the testing machine to suddenly decrease load to maintain a constant displacement rate. Figure 6.5 shows the average stress-strain curve obtained from the experiments. Note that the average stress-strain curve in Figure 6.5 was calculated using the mean ultimate stress and mean ultimate strain of the four test specimens.

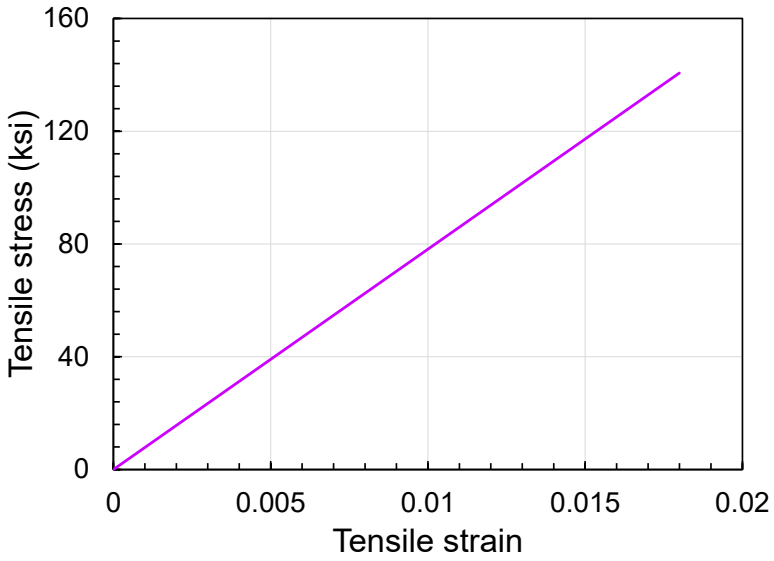

Figure 6.5 Average stress-strain curve for tested GFRP rebar

The tensile modulus values obtained experimentally were found to be higher than the values from the literature. The failure patterns observed in the experiments are shown in Figure 6.6.

(a) *(b)*

Figure 6.6 Failure modes of GFRP rebar

Despite the deviations from the ASTM D7205 standard noted above, the specimens failed in a manner consistent with a successful test. Specifically, the specimens did not fail at the anchors, exhibited brittle behavior until failure, and demonstrated tensile properties consistent with those obtained from the literature.

6.4 SUMMARY

The tensile strength properties exhibited by the tested GFRP rebar were found to be consistent with the values obtained from the literature. However, the tensile modulus was observed to be higher than the values found in the literature. The validity of the tensile properties calculated for the MnDOT GFRP rebar is further supported by the behavior of the specimens during testing. Specifically, the specimens exhibited brittle behavior until failure, and failure did not occur at the anchors.

Failure occurred suddenly in the sense that the GFRP specimens did not show any yielding prior to failure. However, failure did not occur completely without warning, as it may in a glass rod, for example. Instead, there was a 30 to 40 second period during which the glass fibers in the GFRP bars snapped and separated from the polymer matrix. During this period, the strain gauge came unattached from the specimen as the fibers split from the polymer in a sort of fraying manner.

Table 6.3 Comparison between Steel and GFRP bars mechanical properties

	Steel*	GFRP**
Yield Stress (ksi)	40-75 ksi	Not applicable
Elastic Modulus (ksi)	29000 ksi	5920-7990 ksi
Minimum Tensile Strength (ksi)		80-174 ksi
Yield Strain (%)	0.14-0.25%	Not applicable
Ultimate Strain (%)	10-12%	1.2-2.4%

*Standard properties of steel rebars
**GFRP properties from different references included in the main text.

Table 6.3 shows GFRP bars have higher tensile strength but less stiffness than steel. Due to the less stiffness, GFRP rebars provides less confinement to concrete. Due to inherent brittleness and less confinement, GFRP rebars cannot be used in seismic regions. Thus, while GFRP rebar offers a very high ultimate tensile stress relative to the yield stress of steel, its inherent brittleness is less desirable than the ductility of steel in the context of a tension-controlled reinforced concrete member. A brittle material would not offer the same gradual failure as the yielding of steel. However, assuming that the capacity of a member is not greatly exceeded, the drawn-out snapping of fibers that occurs as GFRP fails may provide some degree of warning if a concrete member were to fail in tension.

CHAPTER 7: DETAILING AND COST CONSIDERATIONS

This chapter covers a range of reinforcement details and life-cycle cost considerations related to GFRP-reinforced bridge decks.

7.1 DESIGN AND DETAILING CONSIDERATIONS

This section covers design and detailing recommendations related to the use of GFRP-reinforced concrete in bridge deck applications. For this purpose, the relevant AASHTO and CSA S6 guidelines are discussed hereunder.

7.1.1 AASHTO Specifications

This section summarizes the provisions of AASHTO LRFD Bridge Design Guide Specifications for GFRP-reinforced bridge decks (2018). The referenced guide specifications only provides the minimum requirements for public safety and does not substitute for the judgment of a design professional. Material properties should be in compliance with ASTM D7957/D7957M-22. AASHTO (2018) includes the geometric, material, mechanical, and physical properties of the solid round GFRP bars for concrete reinforcement. Section 2.4.2 of AASHTO (2018) summarizes some material properties of GFRP reinforcing bars like tensile strength and strain and modulus of elasticity. AASHTO (2018) does not cover prestressed applications, lightweight concrete, seismic load, and other items stated in section 1.3. Rather, it covers the analysis and design of concrete structures consisting of normal weight concrete with a design compressive strength not exceeding 10 ksi. AASHTO (2018) provides specifications similar to the section 9 of AASHTO LRFD Bridge Design Specifications (2017) to a large extent. In addition, it offers some additional guidelines regarding the reinforcement details in sections 3.7.2.5 and 3.7.3.1. A creep rupture limit state is also included in AASHTO (2018).

Limit state design principles, including service, fatigue and creep rupture, strength, and extreme limit states, govern the specifications. The limit states and design methodologies are discussed in section 2.5. For the limit states of service and fatigue and creep rupture, Bernoulli's beam theory is applied. For the other two limit states, the areas of a concrete element characterized by their behavior as B-regions (beam or Bernoulli) or D-regions (distributed or discontinuity) should be determined. A sectional design model governs the design of B-regions, with the flexure based on the conventional beam theory and the shear based on the conventional beam theory and the truss analogy. D-regions should be designed according to the strut-and-tie method, while some familiar types might be designed by empirical approaches or legacy detailing practices. All of the limit states should comply with the provisions of sections 2.5.2, 2.5.3, 2.5.4, 2.5.5, and 2.5.6.

The design of B-regions includes the flexural and axial force effects as discussed in section 2.6 and shear and torsion as discussed in section 2.7. The rectangular stress distribution in section 2.6.2.2 could be used for the practical design of flexural concrete members. Therefore, the flexural resistance of the component is calculated for compression- or tension-controlled sections based on the tensile strains of the GFRP bars. If a more precise calculation is required, the strain compatibility approach might be

utilized. Section 2.6.3.3 explains the reinforcement limits in a flexural member. The referenced section provides no maximum reinforcement limit. The amount of tensile reinforcement is expected to be enough to develop flexural resistance exceeding the minimum of 1.33 times the factored moment and that from equation 2.6.3.3-1. The instantaneous and long-term deflections of bending components are covered in section 2.6.3.4.

As for the shear and torsional design of concrete structures reinforced with GFRP bars, section 2.7.1.4 categorizes the slab as a series of B-regions and suggests a sectional design model. Thus, the general requirements of shear and torsion are discussed in section 2.7.2.1, followed by the transverse reinforcement properties—with the exception of slabs and footings—and shear stress calculation in section 2.7.2.8. Section 2.7.3 covers the details and requirements of the sectional design model and reviews the nominal shear resistance of concrete, transverse reinforcement, and longitudinal reinforcement if torsion consideration is required. Section 2.9 specifies the reinforcement details, including concrete cover, hooks and bends, bar spacing, transverse reinforcement, shrinkage and temperature reinforcement, and development and splices. Additionally, section 2.10.1 limits the reinforcing bar size to No. 10 in concrete bridge decks. The provisions for the slab superstructure types, including cast-in-place solid slabs and precast decks as well as beams and girders and diaphragms, are discussed in sections 2.10.2, 2.10.3, and 2.10.4. Additionally, one-way and two-way shear in slabs should be determined in accordance with section 2.10.5.1.

Section 3 of the design code goes over the analysis and design of bridge decks reinforced with GFRP bars. Section 3.5 defines the requirements for the service, creep rupture, fatigue, strength, and extreme limit states of slabs. The analysis methods are stated to be approximate elastic and refined analysis methods from articles 4.6.2.1 and 4.6.2.3 of the AASHTO LRFD Bridge Design Specifications or the empirical design method. The latter might be used if the conditions of section 3.7.2.4 are met. The other parts of section 3.7.2 explain the requirements and definitions related to the empirical design method. Thus, according to section 3.7.2.5, four orthogonal layers of bars not smaller than No.5 with the outermost layers placed in the direction of the effective length should be provided in slabs that are designed based on the empirical design method. The effective length criteria are explained in section 3.7.2.3. Section 3.7.2.5 also reviews the minimum amount of GFRP reinforcement, the maximum spacing of the GFRP reinforcing bars in each direction, and the increase in the reinforcement due to excessive skew angles. Accordingly, the minimum GFRP reinforcement is $870d/E_f$ in in^2/ft for the bottom layer along the effective length, where d represents the effective depth (in) and E_f is the tensile modulus of elasticity of GFRP bars (ksi). The other three layers should have a minimum reinforcement ratio of 0.0035. The maximum spacing between the bars is 12 in. The steps and requirements of the traditional design method can be found in section 3.7.3.

7.1.2 CSA Specifications

The CSA S6 (2019) specification applies to prestressed and non-prestressed beams and slabs, externally and internally restrained slabs, stressed wood decks, and barrier walls.

Section 16.4 explains the durability requirements of FRP bars, specifying the reinforcement cover for bars and tendons in section 16.4.5. Accepted material properties of FRP bars, including tensile strength and modulus of elasticity, are discussed in section 16.5. Accordingly, the resistance factor for GFRP reinforcement in concrete shall be 0.65. The resistance factors provided for other FRP materials are presented in Table 7.1.

Table 7.1 Resistance factors for pultruded FRP and aramid fiber rope

Application	ϕFRP
AFRP reinforcement in concrete and NSMR	0.65
AFRP in externally bonded applications	0.55
AFRP and aramid fiber rope tendons for concrete and timber components	0.60
CFRP reinforcement in concrete	0.80
CFRP in externally bonded applications and NSMR	0.80
CFRP tendons	0.80
GFRP reinforcement in concrete	0.65
GFRP in externally bonded applications and NSMR	0.70
GFRP tendons for concrete components	0.55
GFRP tendons for timber decks	0.70

Externally restrained deck slab guidelines are mainly reported in section 16.7. Sections 16.7.2 and 16.7.3 cover the details required to design full-depth cast-in-place deck slabs and cast-in-place deck slabs on stay-in-place formwork, respectively. Orthogonal GFRP bars not less than $0.0015t$ mm^2/mm ($0.018t$ in^2/ft, where t is the deck thickness) in each direction should be used in the bottom and middle of these types of slabs, respectively, to control cracks.

The design details for concrete beams and slabs are given in section 16.8. Several aspects of the mentioned slabs, including minimum flexural resistance (at least 1.5 times the cracking or factored moment), crack-control reinforcement requirements, maximum stress in GFRP bars under service loads with a resistance factor of 0.25, development length, and tendon properties, are discussed in this section. Section 16.8.7 specifies the shear design of slabs with FRP bars in accordance with the related strains. The minimum amount of shear reinforcement is also mentioned in this section. Requirements and details for internally restrained cast-in-place deck slabs are covered in section 16.8.8. Accordingly, the empirical design method can be applied to decks with FRP bars that meet specific requirements, including (a) two orthogonal FRP bars (not less than 15 mm in diameter) with the clear distance between the top and bottom transverse bars being at least 55 mm, (b) a minimum area of $500d_s/E_{FRP}$ for the transverse FRP bars in the bottom mat, and (c) a minimum GFRP bar ratio of 0.0035 for the other three directions. Finally, section 16.8.8.2 discusses the flexural design of the cast-in-place deck slabs and specifies a maximum reinforcement spacing of 300 mm and a minimum bar diameter of 15 mm.

An informative non-mandatory annex describing the design of pultruded GFRP composite bridges for pedestrians or bicycles is provided as Annex A16.3. The annex accepts grade E17 and grade E23 GFRPs. The design details, including tension and compression slenderness ratios, deflection limits under live and lateral loads, vibration properties like damping value and fundamental frequencies, maximum stress at

service limit state, minimum member thickness values, and connection details, are also provided in section A16.3.3.

7.2 LIFE-CYCLE COST ANALYSIS

In conventional concrete bridge decks, corrosion of steel reinforcement is the primary source of deterioration. This deterioration results in the loss of billions of dollars every year due to the maintenance and replacement of bridge decks in the United States. In Minnesota, the average annual snowfall ranges from 36 in. in the southwest to more than 70 in. in the regions along Lake Superior. The average snowfall in the metro Minneapolis has been recorded to be 51.2 in. As a result, reinforced concrete bridge decks are often exposed to a significant amount of deicing salts and can consequently experience extensive material deterioration.

7.2.1 Overview

Deterioration over time can significantly reduce the service lives of bridge decks and increase their vulnerability to other environmental and mechanical stressors. As a potential solution, the use of GFRP rebars can be considered, mainly because they are not susceptible to corrosion. However, the cost of GFRP rebars can be different than that of conventionally used epoxy-coated steel rebars. Therefore, a life-cycle cost analysis (LCCA) is needed to evaluate whether the use of GFRP-reinforced bridge decks is a viable economic choice. In this study, the LCCA performed used estimated initial costs, repair costs, and re-decking costs to compute the various costs over the service life of the bridges under consideration.

7.2.2 Life-Cycle Cost Analysis (LCCA)

LCCA was performed to compare the life-cycle cost of the GFRP-reinforced bridge deck (27W37) to that of the steel-reinforced bridge deck (27W36). The calculations compared the deck rebar design options with integral abutments and no expansion joints. Therefore, the analysis does not represent the life-cycle cost of the full bridge structure.

The steel-reinforced bridge deck (27W36) is reinforced with epoxy-coated steel rebars, while the GFRP-reinforced bridge deck (27W37) is reinforced with GFRP rebars. The initial construction costs, repair costs, and other costs used in the analysis are shown in Table 7.2. The repair techniques include mill and overlay (i.e., removing the top layer of existing pavement and replacing it with a new layer) and mill and patch (i.e., a more localized repair technique, involving milling out small areas of damaged pavement and filling them again). The costs used in the LCCA are approximated MnDOT construction costs, and engineering judgement was used to predict the time of work activities and the service lives of the two bridges. The cost of the GFRP rebars used for construction was \$6/ft^2 higher than the cost of the steel rebars. Table 7.2 shows three types of milling and patching costs. Here, Type D, E, and F represent costs related to 1.0%, 0.5%, and 0.25% of the wearing course area.

Table 7.2 Life-cycle costs for the two bridge decks

Costs (per ft^2)	Bridge 27W36	Bridge 27W37
Rebar costs	$9.00	$15.00
Total construction costs	$36.00	$42.00
Mill and overlay	$8.50	$0.00
Mill and patch deck Type D	$38.00	$0.00
Mill and patch deck Type E	$48.00	$0.00
Mill and patch deck Type F	$68.00	$0.00
Mill and patch	$15.66	$0.00
Re-decking	$65.00	$71.00

Unlike the service life of the GFRP-reinforced bridge deck (27W37), the service life of the steel-reinforced bridge deck (27W36) is well understood. In the Midwest, bridge decks are typically assumed to have a service life of 65 years. In the absence of knowledge and data about GFRP-reinforced bridge decks, three service lives of 50 years, 65 years, and 80 years were assumed. At the end of their service lives, bridge decks are re-decked. From experience, the first repair on the bridge was assumed to be related to milling and overlay, and deck patching was assumed to occur after 30 years of service. Another deck patching on the steel-reinforced bridge deck (27W36) was assumed to be performed after 45 years of service. At the end of a service life of 65 years, the steel-reinforced bridge deck (27W36) was assumed to be replaced. Since GFRP rebars are not expected to corrode, which should prevent spalling of the concrete, bridge repair costs were not included in the analysis. It should be noted that this assumption can result in optimistic results and may need to be reassessed. The LCCA was conducted for a period of 100 years. The present value was calculated using the following equation:

$$\text{Present value} = \text{Cost}\left(\frac{Ia}{1+r}\right)^n \tag{7.1}$$

where *Ia* is the inflation adjustment taken as 1.0023, *r* is the discount rate taken as 1.22%, and *n* is the number of years. The remaining capital value of the decks was calculated using a straight-line depreciation method. The life-cycle costs calculated for the two bridges are presented in Tables 7.3 and 7.4.

Table 7.3 Life-cycle costs for steel-reinforced bridge deck (27W36)

Year	Service life: 65 years		
	Costs (per ft^2)		Present value (per ft^2)
0	Initial cost	$36.00	$36.00
30	Mill and overlay	$24.16	$17.99
45	Mill and patching	$15.66	$10.06
65	Re-deck	$65.00	$34.31
100	Remaining capital value of deck	$30.00	-$11.23
Life-cycle costs			$87.14

Table 7.4 Life-cycle costs for GFRP-reinforced bridge deck (27W37)

Year	Service life: 50 years			Service life: 65 years			Service life: 80 years		
	Cost (per ft^2)		Present value (per ft^2)	Costs (per ft^2)		Present value (per ft^2)	Costs (per ft^2)		Present value (per ft^2)
0	Initial cost	$42.00	$42.00	Initial cost	$42.00	$42.00	Initial cost	$42.00	$42.00
50	Re-deck	$71.00	$43.43	—	—	—	—	—	—
65	—	—	—	Re-deck	$71.00	37.48	—	—	—
85	—	—	—	—	—	—	Re-deck	$71.00	$30.79
100	Remaining capital value of deck	$0.00	$0.00	Remaining capital value of deck	-$32.77	-$12.28	Remaining capital value of deck	-$53.25	-$19.33
	Life-cycle costs		$85.43	Life-cycle costs		$67.22	Life-cycle costs		$54.41

As shown in Table 7.3, the life-cycle cost per square foot for the steel-reinforced bridge deck (27W36) with a 65-year service life is observed to be $87.14/ft^2. The life-cycle costs calculated for the GFRP-reinforced bridge deck (27W37) are presented for three scenarios in Table 7.4. The life-cycle cost of the GFRP-reinforced bridge deck (27W37) is approximately equal to that of the steel-reinforced bridge deck (27W36) when the GFRP-reinforced bridge deck (27W37) is assumed to have a service life of 50 years. For service lives of 65 years and 80 years, the life-cycle costs are observed to be $67.22/ft^2 and $54.41/ft^2, respectively. The results show that use of GFRP rebars can be a viable economic option.

During the inspections, it was observed that even the bridge deck with GFRP rebars developed surface and full-depth cracking. In the first set of analyses, no repair costs were considered for the GFRP-reinforced bridge deck (27W37). The second set of analyses was performed to consider the repairs assumed to occur after 30 years of service life. A 30-year period was chosen based on the common practice. These repair costs were assumed to be similar to those of the steel-reinforced counterpart. From the results of the updated analysis (Table 7.5), it can be observed that GFRP rebars are still an economically viable option when the initial service life is taken as 65 or 80 years. Figures 7.1 and 7.2 illustrate the life-cycle costs of the two bridges for three life spans without and with additional repairs, respectively.

Table 7.5 Life-cycle costs for GFRP-reinforced bridge deck (27W37) with additional repairs

Year	Service life: 50 years			Service life: 65 years			Service life: 80 years		
	Costs (per ft^2)		Present value (per ft^2)	Costs (per ft^2)		Present value (per ft^2)	Costs (per ft^2)		Present value (per ft^2)
0	Initial cost	$42.00	$42.00	Initial cost	$42.00	$42.00	Initial cost	$42.00	$42.00
30	Mill and overlay	$24.16	$17.99	Mill and overlay	$24.16	$17.99	Mill and overlay	$24.16	$17.99
50	Re-deck	$71.00	$43.43	—	—	—	—	—	—
65	—	—	—	Re-deck	$71.00	37.48	—	—	—
85	—	—	—	—	—	—	Re-deck	$71.00	$30.79
100	Remaining capital value of deck	$0.00	$0.00	Remaining capital value of deck	-$32.77	-$12.28	Remaining capital value of deck	-$53.25	-$19.33
	Life-cycle costs		$103.42	Life-cycle costs		$85.21	Life-cycle costs		$72.40

Figures 7.1 and 7.2 illustrate a direct comparison of the life-cycle costs of the steel- and GFRP-reinforced bridge decks over three life spans (i.e., 50, 65, and 80 years) without and with additional repairs, respectively. The referenced figures show that the GFRP-reinforced bridge deck can be a superior choice, especially for extended service lives.

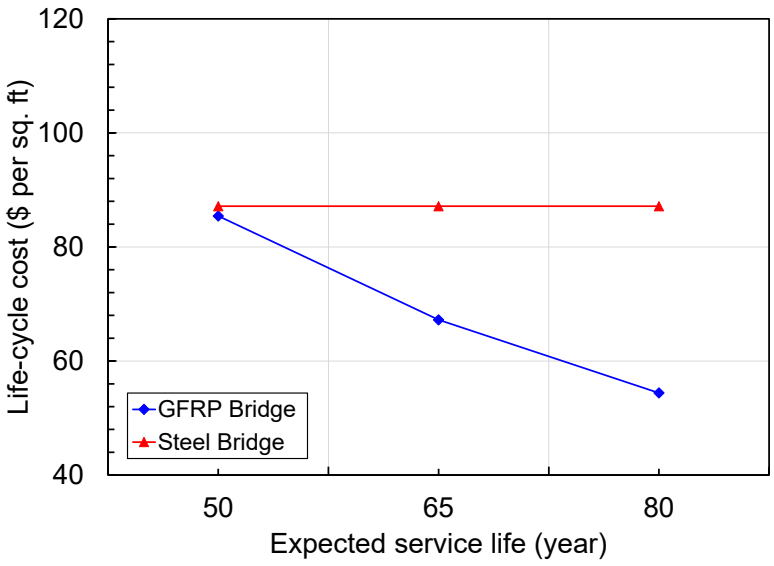

Figure 7.1 Life-cycle cost for the bridge deck with the assumption of requiring no additional repairs

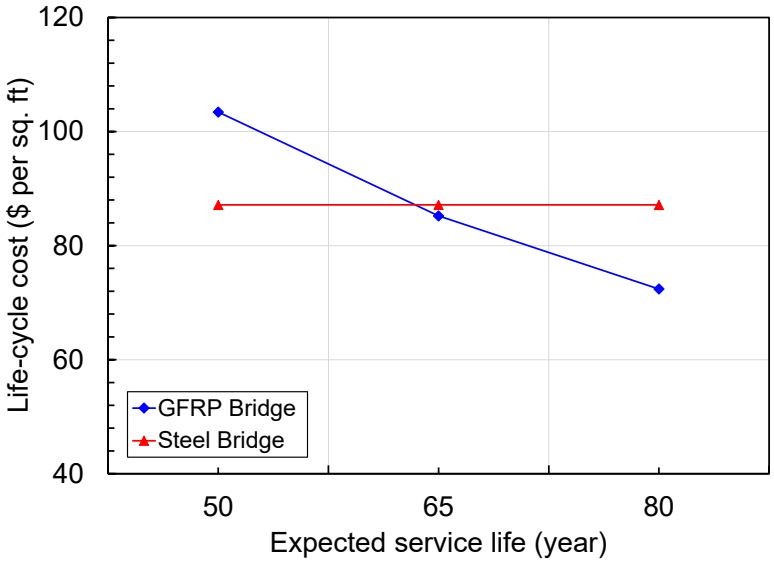

Figure 7.2 Life-cycle cost for the bridge deck with the assumption of requiring additional repairs

CHAPTER 8: SUMMARY AND CONCLUSIONS

8.1 SUMMARY

In 2018, MnDOT constructed two side-by-side bridges on TH 169 over Elm Creek, with the northbound bridge deck reinforced with conventional steel bars and the southbound slab reinforced with GFRP bars. The goal of the research project described in this report was to evaluate the fundamental structural behavior of the GFRP-reinforced bridge deck compared to that of the steel-reinforced slab to evaluate the performance of GFRP reinforcement under both environmental stressors and service loads. To achieve this goal, comprehensive field testing was carried out to investigate the performance of the two bridges, and laboratory testing was conducted on the GFRP rebar used in the southbound bridge deck.

Prior to placing the concrete bridge decks, VW gauges were installed to measure the strain values inside the decks. To best measure performance, gauge locations were selected to capture the extreme response, characterize the general response, and determine the relevant response measures (e.g., live load GDFs). The temperature at each strain gauge was also captured from the thermistors built into the VW gauges. The VW gauges were connected to a data-acquisition system placed under the bridge deck. The data from the gauges were recorded continuously over a period of three years using the data-acquisition system.

In addition to these long-term performance monitoring efforts, three live load field tests were performed on each of the bridges. The first test was conducted prior to opening the bridges to regular traffic. The second and third load tests were conducted June 2021 and August 2022, respectively. Strains recorded during the live load testing were analyzed to evaluate deck behavior. The primary focus of the live load tests was to understand the manner in which the decks participate globally along with the girders to transfer vehicle loads longitudinally to the abutments.

The research project also included a condition assessment of the bridge decks at regular intervals throughout the duration of the project. The condition assessment included documentation of the deck surface and of any full-depth cracks on top of and underneath the bridge decks, including the types and locations of the cracks and other relevant information.

The research project also evaluated the mechanical properties of the GFRP rebar used in the southbound bridge deck. For that purpose, the researchers conducted a set of laboratory tests on the GFRP rebar used by the contractor. The specimens were loaded in tension until failure, while force, displacement, and strain were measured during loading.

8.2 CONCLUSIONS

The primary conclusion from the live load data analysis was that the two bridge decks behaved consistently and as expected over the first three years. Accordingly, the GFRP-reinforced bridge deck showed no unusual behavior compared to the steel-reinforced deck.

The analysis of the live load data indicated that the shape and magnitude of the strain response under truck loads matched the expected behavior and were similar for the three on-site field tests. A difference identified between the results of the second year and the results of the other two years for the GFRP-reinforced bridge deck (27W37) was due to a change in the location of the sensors. No evidence of a response to the cracking observed and documented in the decks was obtained from the analysis of the live load test data, indicating that the structural integrity of the bridges was consistent with the design specifications.

From the test data, the depth of the neutral axis was determined from the strain data. The neutral axis data for different years showed that the bridge deck behavior was consistent for both bridges and that using GFRP bars as an alternate for bridge deck reinforcement did not change the behavior of the bridge deck significantly. The correlation between the strain data on the deck and the girders showed the composite action being maintained by the reinforced concrete slabs of the bridge decks.

From the live load tests, girder distribution factors (GDFs) were computed using the strain data from the strain gauges on the girders. The GDFs were found to be lower than the values obtained from the AASHTO GDF equations. The reason could be the higher transverse stiffness or lower longitudinal stiffness of the bridge decks, which causes more uniform distribution of the load among the girders. Moreover, the GDFs calculated for both bridges showed approximately similar behaviors with no significant difference.

The data collected from the VW gauges were used to understand the performance of the bridge decks under environmental loads such as temperature and humidity, time-dependent effects such as shrinkage, and vehicle loads. The collected strain data were analyzed to determine the condition of the bridge decks for close to four years. From the data, a variation was observed in the strain data in the early life of the bridge with respect to variations in temperature. On exploring the temperature strain and shrinkage strain, the researchers found that shrinkage strain primarily governed bridge behavior in the early days. Overall, the researchers found that the bridges' behavior was consistent over the first four years. The investigations showed that the GFRP bars behaved similarly to the steel bars during these years. The GFRP-reinforced deck showed slightly higher strain values overall. The excess amount, however, was too small to make a notable difference over the bridge's lifetime.

The researchers assessed the condition of the bridge decks by making visits to the bridge site on a regular basis. Several lateral and inclined cracks were observed mostly near the abutments in both bridge decks. In addition to surface cracks, full-depth cracks were also observed near the abutments. Shrinkage, temperature gradients, and the fixity effects of the integral abutments could have caused the cracks that developed on the bridge decks. Generally, mostly similar crack patterns were observed on the two bridge decks.

Finally, the comparison between the short- and long-term performance of the bridge decks reinforced with steel and GFRP rebar revealed no significant difference over three years, indicating that GFRP bars could be used as an alternative in bridge deck reinforcement.

8.3 RESEARCH BENEFITS AND IMPLEMENTATION STEPS

Bridges in Minnesota, like elsewhere, are expected to be designed for a service life of (at least) 75 years. While the design loads are specified for a 75-year recurrence interval, the current specifications do not necessarily help the transportation agencies ensure that the bridge will remain in service for 75 years. Therefore, it is not surprising that existing bridge elements, such as decks, are found in need of a major repair or complete replacement after only 30 to 40 years. The degradation of bridge decks is mainly due to the corrosion of steel reinforcing bars embedded in concrete. Considering the time and labor required to address this critical issue, the completed research project investigated an alternative solution of using corrosion resistant GFRP rebars (instead of their metallic counterparts). With successful implementation, the outcome of this project reduced the direct costs originating from maintenance efforts required for the bridge decks made with steel rebars. Furthermore, increased service life of bridge decks minimizes the need to replace them during a bridge's design life. This also eliminates the indirect costs from possible bridge closure, disruption in traffic, and impact on surrounding environment.

Although there has been wide use of GFRP reinforcement in bridge decks in some parts of Canada, there have been relatively few GFRP reinforced bridge decks built in the United States. GFRP rebars have shown a great potential for structural applications in bridges owing to their high resistance to corrosion, low weight-to-volume ratio, and high tensile strength. To properly use the capabilities of such rebars, a number of studies have been performed and the results are available in the literature review section of this report. However, very few field investigations have been conducted to examine the durability and strength of the bridge decks constructed with GFRP rebars. The current research project addressed this knowledge gap and provided firsthand information from the field that can be used in the future to build similar bridges. To achieve this goal, the research team developed a comprehensive plan to investigate both short and long-term behavior of the two bridges constructed side by side north of Minneapolis. To make direct comparisons possible, one bridge deck was reinforced with steel rebars and the other with GFRP rebars.

Long-term monitoring of the two bridges was aimed at understanding the changes in strain in bridge decks over an extended period of time, which included seasonal variations. The two bridges being compared were adjacent to each other, which provided a great opportunity to directly compare the behavior of the two decks as they experience very similar environmental conditions. The two bridges were monitored for the first four years of their service life. Considering the importance of the long-term monitoring of the steel and GFRP rebars embedded in concrete, it was critical to install strain gauges and thermocouples during the construction of the bridge deck. This was achieved using a set of VW strain gauges. VW strain gauges were proven to deliver high accuracy for long-term monitoring, while providing a long service life. Each VW strain gauge was also equipped with a thermistor that measured the temperature at the location of the gauge.

Live load tests on GFRP and steel reinforced bridge decks were aimed at understanding the distribution of loads from the point of application to the deck and supporting girders. It was imperative to capture stresses and strains developed in the deck while transferring the loads. Stresses, strains, and deflections

were used to evaluate whether the GFRP-reinforced deck reasonably met the expected structural behavior with respect to load-carrying mechanisms and the stress levels generated in the superstructure. The data obtained from the live load tests was also beneficial in assessing the likelihood of immediate and long-term crack development in the bridge deck from vehicle loads. The primary focus of live load tests was to understand the manner in which the deck participated along with the girders to transfer the vehicle loads to the abutments. To address the required performance issues, gauge locations were selected to: (1) capture the extreme response, (2) characterize the response in general, and (3) determine the relevant response measures (e.g., live load girder distribution factors).

The research project also included condition assessment of bridge decks at regular intervals throughout a four-year duration. The condition assessment included the documentation of crack formation and propagation. This effort helped ensure that there were no concerning serviceability issues in bridge decks. On the other hand, the potential effects of severe environmental stressors, such as deicing salts, freeze-thaw cycles, and high temperatures, on the structural integrity of the deck elements were assessed. To maximize research benefits, the project was completed with a detailed service-life analysis of both bridges, taking into consideration initial construction costs as well as any costs incurred for repair and maintenance. Due to the inherent corrosion resistance of GFRP rebars, the cost related to the repair and maintenance of the GFRP-reinforced bridge deck was low compared to that estimated for the steel-reinforced bridge deck. This was achieved without compromising any of the required structural performance measures.

The reported results shed light on the practical advantages of using GFRP rebars for deck reinforcement, facilitating the future implementation of GFRP rebars in various bridge projects in Minnesota and beyond. It should be noted that, despite the wealth of data collected from the two bridges during their first four years of service, a four-year duration is essentially a snapshot when compared to the 75-plus years of service anticipated for these bridges. Hence, additional monitoring is recommended after 10, 25, and 35 years to obtain holistic insights, as the decks continue to degrade and live their lives.

REFERENCES

AASHTO. 1996. *Standard Specifications for Highway Bridges*. American Association of State Highway and Transportation Officials, Washington, DC.

AASHTO. 1998. *AASHTO LRFD Bridge Design Specifications*. 1st edition. American Association of State Highway and Transportation Officials, Washington, DC.

AASHTO. 2017. *AASHTO LRFD Bridge Design Specifications*. 8th edition. American Association of State Highway and Transportation Officials, Washington, DC.

AASHTO. 2018. *AASHTO LRFD Bridge Design Guide Specifications for GFRP–Reinforced Concrete*. 2nd edition. American Association of State Highway and Transportation Officials, Washington, DC.

ACI 440.1. 2015. *Guide for the Design and Construction of Concrete Reinforced with FRP Bars*. American Concrete Institute, Farmington Hills, MI.

Ahmed, E. A., F. Settecasi, & B. Benmokrane. 2014. Construction and Testing of GFRP Steel Hybrid-Reinforced Concrete Bridge-Deck Slabs of Sainte-Catherine Overpass Bridges. *Journal of Bridge Engineering*, *19*(6), 04014011.

Alagusundaramoorthy, P., I. E. Harik, & C. C. Choo. 2006. Structural Behavior of FRP Composite Bridge Deck Panels. *Journal of Bridge Engineering*, *11(*4), 384–393.

ASTM D7205. 2016. *Standard Test Method for Tensile Properties of Fiber Reinforced Polymer Matrix Composite Bars*. ASTM International, West Conshohocken, PA.

Benmokrane, B., E. El-Salakawy, A. El-Ragaby, & T. Lackey. 2006. Designing and Testing of Concrete Bridge Decks Reinforced with Glass FRP Bars. *Journal of Bridge Engineering*, *11*(2), 217–229.

Cao, L. 1996. *Analysis and Design of Slab-on-Girder Highway Bridge Decks*. PhD dissertation. University of Colorado, Boulder, CO.

Cheng, L. 2005. *Development of a Steel-Free FRP-Concrete Slab-on-Girder Modular Bridge System*. PhD dissertation. University of California, San Diego, CA.

Cheng, L. 2011. Flexural Fatigue Analysis of a CFRP Form Reinforced Concrete Bridge Deck. *Composite Structures*, *93*(11), 2895–2902.

Cheng, L. & V. M. Karbhari. 2006. New Bridge Systems Using FRP Composites and Concrete: A State-of-the-Art Review. *Progress in Structural Engineering and Materials*, *8*(4), 143–154.

CSA. 2000. *Canadian Highway Bridge Design Code*. Canadian Standards Association, Toronto, ON.

CSA. 2019. *Canadian Highway Bridge Design Code*. S6:19. Canadian Standards Association, Toronto, ON.

Cuelho, E., J. Stephens, P. Smolenski, & J. Johnson. 2006. *Evaluating Concrete Bridge Deck Performance*. Western Transportation Institute, Montana State University, Bozeman, MT.

Deitz, D. H. 1998. *GFRP-reinforced Concrete Bridge Decks*. PhD dissertation. University of Kentucky, Lexington, KY.

Deitz, D., I. E. Harik, & H. Gesund. 2000. *GFRP-reinforced Concrete Bridge Decks*. Kentucky Transportation Center, University of Kentucky, Lexington, KY.

Eitel, A. K. 2005. *Performance of a GFRP-reinforced Concrete Bridge Deck*. PhD dissertation. Case Western Reserve University, Cleveland, OH.

El-Ragaby, A., E. F. El-Salakawy, & B. Benmokrane. 2005. Finite Element Modeling of Concrete Bridge Deck Slabs Reinforced with FRP Bars. Special Publication 230-52. *SP-230: 7th International Symposium on Fiber-Reinforced (FRP) Polymer Reinforcement for Concrete Structures*, pp. 915–934.

El-Ragaby, A., E. El-Salakawy, & B. Benmokrane. 2007. Fatigue Analysis of Concrete Bridge Deck Slabs Reinforced with E-Glass/Vinyl Ester FRP Reinforcing Bars. *Engineering Composites: Part B*, *38*(5–6), 703–711.

El-Salakawy, E. F. & B. Benmokrane. 2004. Serviceability of Concrete Bridge Deck Slabs Reinforced with FRP Composite Bars. *Structural Journal*, 101(5), 727–736.

El-Salakawy, E., B. Benmokrane, A. El-Ragaby, & D. Nadeau. 2005. Field Investigation on the First Bridge Deck Slab Reinforced with Glass FRP Bars Constructed in Canada. *Journal of Composites for Construction*, *9*(6), 470–479.

Hall, T., & A. Ghali. 2000. Long-Term Deflection Prediction of Concrete Members Reinforced with Glass Fibre Reinforced Polymer Bars. *Canadian Journal of Civil Engineering*, *27*(5), 890–898.

Harik, I., P. Alagusundaramoorthy, R. Siddiqui, R. Lopez-Anido, S. Morton, P. Dutta, & B. Shahrooz. 1999. Testing of Concrete/FRP Composite Deck Panels. *Proceedings of the 5th Construction Materials Congress, Materials Engineering Division*, Cincinnati, OH, pp. 351–358.

Hassan, T., A. Abdelrahman, G. Tadros, & S. Rizkalla. 2000. Fiber Reinforced Polymer Reinforcing Bars for Bridge Decks. *Canadian Journal of Civil Engineering*, *27*(5), 839–849.

Holden, K. M., C. P. Pantelides, & L. D. Reaveley. 2014. Bridge Constructed with GFRP-Reinforced Precast Concrete Deck Panels: Case Study. *Journal of Bridge Engineering*, *19*(5), 1–7.

Imbsen, R. A., D. E. Vandershaf, R. A. Schamber, & R. V. Nutt. 1995. *NCHRP Report 276: Thermal Effects in Concrete Bridge Superstructures*. National Cooperative Highway Research Program, Washington, DC.

Kitane, Y., A. J. Aref, & G. C. Lee. 2004. Static and Fatigue Testing of Hybrid Fiber-Reinforced Polymer-Concrete Bridge Superstructure. *Journal of Composites for Construction*, *8*(2), 182–190.

Kumar, S. V., & H. V. S. GangaRao. 1998. Fatigue Response of Concrete Decks Reinforced with FRP Rebars. *Journal of Structural Engineering*, *124*(1),11–16.

Kwon, S.-C., P. K. Dutta, Y.-H. Kim, & R. Lopez-Anido. 2003. Comparison of the Fatigue Behaviors of FRP Bridge Decks and Reinforced Concrete Conventional Decks under Extreme Environmental Conditions. *Journal of Mechanical Science and Technology*, *17*, 1–10.

Nassif, H., N. Suksawang, M. Gindy, T. Abu-Amra, & J. Davis. 2003. Instrumentation and Field Testing of the Doremus Avenue Bridge. Paper presented at the 82nd Annual Meeting of the Transportation Research Board, January 12–16, Washington, DC.

Pantelides, C. P., K. M. Holden, & J. Ries. 2012. *Health Monitoring of Precast Bridge Deck Panels Reinforced with Glass Fiber Reinforced Polymer (GFRP) Bars*. Utah Department of Transportation, Salt Lake City, UT.

Park, Y., Y. Kim, & S.-H. Lee. 2014. Long-Term Flexural Behaviors of GFRP-reinforced Concrete Beams Exposed to Accelerated Aging Exposure Conditions. *Polymers*, *6*(6), 1773–1793.

Semendary, A. A., E. P. Steinberg, K. K. Walsh, & E. Barnard. 2017. Live-Load Moment-Distribution Factors for an Adjacent Precast Prestressed Concrete Box Beam Bridge with Reinforced UHPC Shear Key Connections. *Journal of Bridge Engineering*, 22(11), 1–18.

Shafei, B., B. Phares, & D. Saini. 2020. *Field Investigation of Bridge Deck Reinforced with Glass Fiber Reinforced Polymer (GFRP) Rebar*. Minnesota Department of Transportation, St. Paul, MN.

Stallings, J. M., & P. Porter. 2002. *Live Load Tests of Alabama's HPC Bridge*. Auburn University Highway Research Center, Auburn, AL.

Tabsh, S. W., & M. Tabatabai. 2001. Live Load Distribution in Girder Bridges Subject to Oversized Trucks. *Journal of Bridge Engineering*, *6*(1), 9–16.

Torres, V., N. Zolghadri, M. Maguire, P. Barr, & M. Halling. 2019. Experimental and Analytical Investigation of Live-Load Distribution Factors for Double Tee Bridges. *Journal of Performance of Constructed Facilities*, *33*(1), 1–11.

Trejo, D., F. Aguiniga, R. L. Yuan, R. W. James, & P. B. Keating. 2005. *Characterization of Design Parameters for Fiber Reinforced Polymer Composite Reinforced Concrete Systems*. Texas Transportation Institute, Texas A&M University System, College Station, TX.

Yang, Y., &J. J. Myers. 2003. Live-Load Test Results of Missouri's First High-Performance Concrete Superstructure Bridge. *Transportation Research Record: Journal of the Transportation Research Board*, *1845*, 96–103.

Yost, J. R., & E. R. Schmeckpeper. 2001. Strength and Serviceability of FRP Grid Reinforced Bridge Decks. *Journal of Bridge Engineering*, *6*(6), 605–612.